Faculty of Mechanical Engineering

High Frequency Oscillations in a Combustion Chamber

A Novel Mitigation Strategy

R.E. de Jongh

15 February 2019

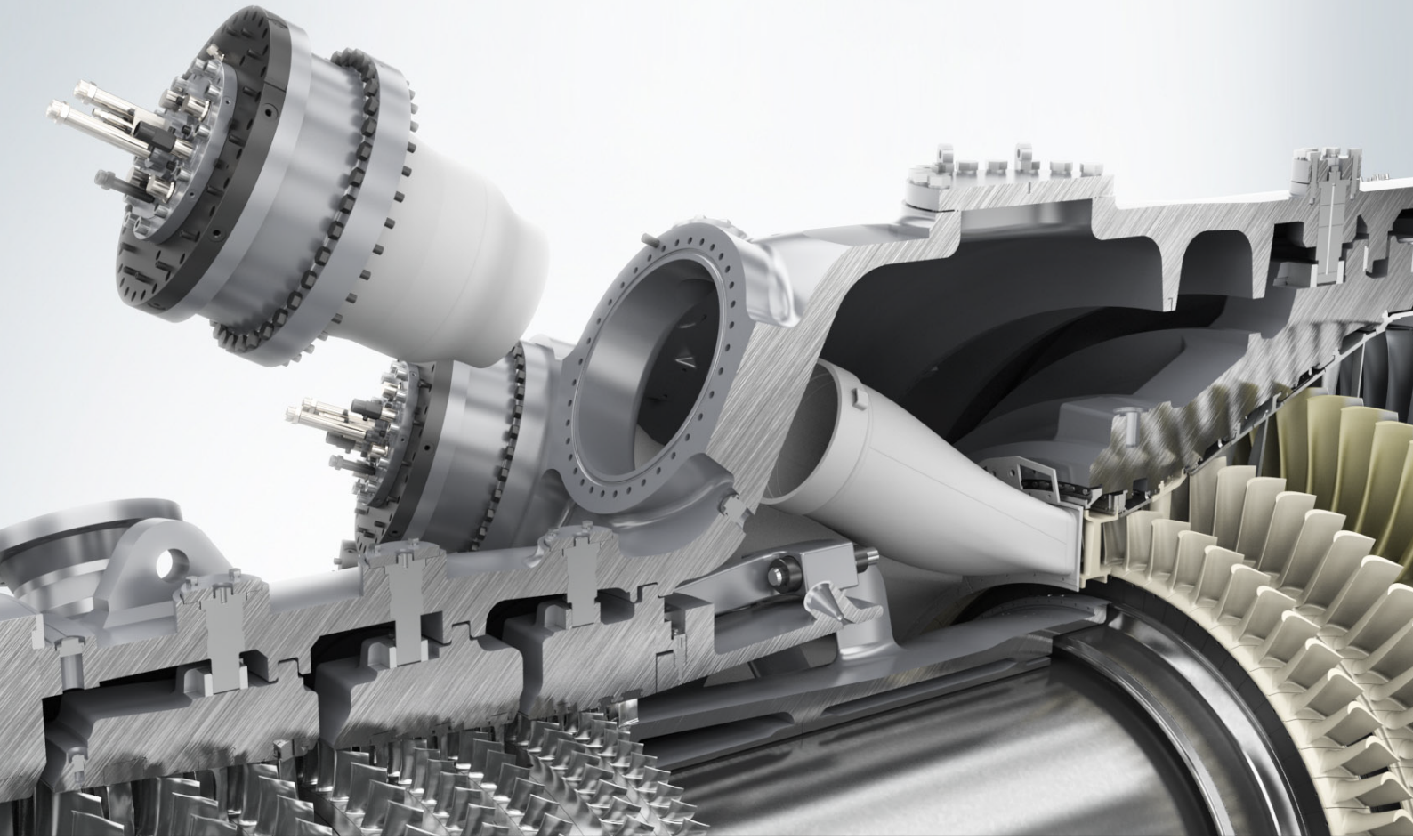

TU Delft Delft University of Technology

SIEMENS

Challenge the future

High Frequency Oscillations in a Combustion Chamber

A Novel Mitigation Strategy

Master of Science Thesis

For obtaining the degree of Master of Science in Mechanical Engineering
at Delft University of Technology

R.E. de Jongh

15 February 2019

Faculty of Mechanical Engineering · Delft University of Technology

Delft University of Technology

Delft University Of Technology
Department Of
Energy and Process Technologies

The undersigned hereby certify that they have read and recommend to the Faculty of Mechanical Engineering for acceptance a thesis entitled **"High Frequency Oscillations in a Combustion Chamber"** by **R.E. de Jongh** in partial fulfillment of the requirements for the degree of **Master of Science**.

Dated: 15 February 2019

Readers:

Prof. dr. ir. S.A. Klein

Prof. dr. ir. B. J. Boersma

Prof. dr. D.J.E.M. Roekaerts

dr. L. Panek

Summary

Restrictions on NO_x emissions are increasingly stricter. In order to reduce the emissions of a gas turbine, manufacturers moved from diffusion-flames to lean premixed flames in their combustion process. However lean premixed flames are prone to (transverse) combustion instabilities. These instabilities consists of thermoacoustically driven pressure oscillations. In order to mitigate acoustic oscillations, dampers are implemented in a gas turbine combustion chamber. These dampers have proven to be effective, but they also consume cooling air, which has a negative impact on the efficiency of the gas turbine. Therefore in this thesis, a solution that potentially provide damping without consuming cooling air is investigated.
Implementing baffles in a combustor is such a mitigation strategy. Experimental results of a baffled combustor exist and the aim of this thesis is to validate the experimental results and to gain more insight in the mechanisms inducing the damping effect of the baffles on transverse thermoacoustic instabilities. Moreover, in literature possible mechanisms with regard to transverse instabilities are found. Part of this thesis is dedicated to reproducing these mechanisms. A Large Eddy Simulation (LES) solver is used to perform the simulations. In addition, a Helmholtz solver is used to further verify the results from the LES.

Before the LES is conducted on the full domain of a test combustor, a smaller domain (1/20 of the test domain) is simulated first to determine the correct settings for simulating transverse combustion instabilities. The chemistry part of the combustion process is performed by tabled chemistry, namely Flamelet Generated Manifolds (FGM). Two different models that account for flame propagation are reviewed for their performance of predicting thermoacoustic behaviour. In order to force a response of the system, a new excitation method (the pressure bomb) is used. The pressure bomb is able to trigger acoustic modes that are not always visible in a self-excited simulation.

The smaller domain is further used to derive more knowledge on the limit cycle behaviour of the flames in a combustion chamber. It is shown that the premix passages acoustically couple with the combustion chamber during transverse combustion instabilities. Moreover, it is derived that a coupling between heat release centre displacement and the transverse acoustic pressure distribution occurs. The flames in a pressure anti-node of the first transverse mode displace in longitudinal direction and the flames in the velocity anti-node displace in

transverse direction. To verify the acoustic results of the smaller domain, the eigenmodes derived by COMSOL are compared to the acoustic modes derived by the LES. As it turns out, the modes derived by LES all align with the eigenfrequencies of the domain. Next, the so called Poor Man's Rayleigh (PMR) criterion is proposed to derive with the eigenfrequency solver which modes are most likely to become unstable. It determines a value based on the overlap between the predicted heat release from Computational Fluid Dynamics (CFD) and the eigenmode pressure distribution derived from an eigenfrequency solver. The results of the PMR are promising and PMR may be used to optimize combustion chambers in the frequency domain.

The simulation results of the baffle configuration implemented in the test combustor indicate that the first transverse mode can sustain. Higher order modes except for the sixth transverse seem to be damped by the baffles. Furthermore it is observed that the first transverse mode in the combustor is a rotating mode. The simulations are able to capture the fact that baffles lower the frequency for the first transverse mode. The simulations did produce much higher oscillation amplitudes than usually in experiments, thus making it difficult to compare the results of the combustors with and without baffles.

Table of Content

List of Figures

List of Tables

List of Acronyms

ATF	Artificially Thickened Flame
BCD	Bounded Central-Differencing
BDF	Backward Differencing Formula
CCGT	Combined Cycle Gas Turbine
CD	Central-Differencing
CFD	Computational Fluid Dynamics
CFL	Courant-Friedrichs-Lewy
DFT	Discrete Fourier Transform
DNS	Direct Numerical Simulation
FD	Finite Differences
FE	Finite Elements
FEM	Finite Element Method
FFT	Fast Fourier Transform
FGM	Flamelet Generated Manifold
FOU	First-Order Upwind
FSD	Flame Surface Density
FV	Finite Volumes
HFD	High Frequency Dynamics
IFD	Intermediate Frequency Dynamics
LES	Large Eddy Simulation
LFD	Low Frequency Dynamics
LGT	Large Gas Turbine
PISO	Pressure Implicit Splitting of Operators
PMR	Poor Man's Rayleigh
RANS	Reynolds Averaged Navier-Stokes
SGS	Smagorinsky Subgrid Scale
SIMPLE	Semi-Implicit method for Pressure-Linked Equation

SOU	Second-Order Upwind
STL	Sensitive Time Lag
TFC	Turbulent Flame Speed Closure
WALE	Wall Adapting Local Eddy-Viscosity

List of Symbols

Greek Symbols

β	Temperature coefficient
Δ	Grid size
Δ_f	LES filter
ϵ	Dissipation
η	Kolmogorov length scale
λ	Wave length
μ	Viscosity
ν	Kinematic viscosity
ν_{sgs}	Subgrid eddy viscosity
ϕ	Scalar quantity
π	Ratio of circumference of circle to its diameter
ρ	Density
ρ_e	Excess density
τ	Stress Tensor
τ_{sgs}	Subgrid stress
T_{sgs}	Subgrid stress tensor

Roman Symbols

A_f	Pre-exponential factor

c	Progress variable
c_0	Speed of sound
Co	Courant number
Da	DamkÃűhler number
E_k	Activation energy
Ka	Karlovitz number
f	Frequency
h	Enthalpy
J_i	Mass diffusion species i
k	Rate coefficient
k_{sgs}	Subgrid kinetic energy
$\bar{M}$	Average molar weight
$\dot{m}$	Mass flow rate
p	Pressure
p_0	Ambient pressure
p'	Pressure fluctuation
Pr	Prandtl number
q	Heat release
$\mathbf{q}$	Heat Flux
R_0	Specific gas constant
Re	Reynolds number
S_{Y_i}	Net rate production of species i by chemical reaction
V	Volume
g	Acceleration due to gravity
v	Velocity
v_l	Laminar flame speed
v'_{rms}	Root mean square velocity fluctuation
v_t	Turbulent flame speed
X	Molar fraction
Y_i	Mass fraction species i
Z	Mixture fraction

Chapter 1

Introduction

Due to the ever increasing demand for electricity worldwide and the fact that the growth of renewable energy is not going fast enough, burning fossil fuels is still required to supply the world with electricity [1]. Combined cycles consisting of a gas turbine (Figure 1.1) and a heat recovery steam generator are an efficient and practical way to generate electricity, while keeping emissions low. In fact, burning natural gas in a Combined Cycle Gas Turbine (CCGT) produces 50 to 60 percent less carbon dioxide than a new coal plant for the same amount of power [2]. Furthermore, CCGT power plants have the flexibility which is necessary in the future with the increasing power generation share of renewables [3]. In the gas turbine section usually natural gas is burned. During the combustion process, NO_x is emitted. Over the years, the restrictions for NO_x emissions have become increasingly stricter [4, 5].

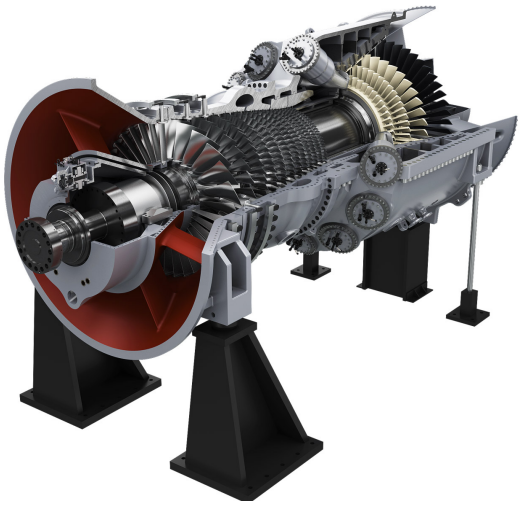

Figure 1.1: The SGT5-9000HL, with a simple cycle output of 593 MWe and a combined cycle efficiency of $> 63\%$ [6]

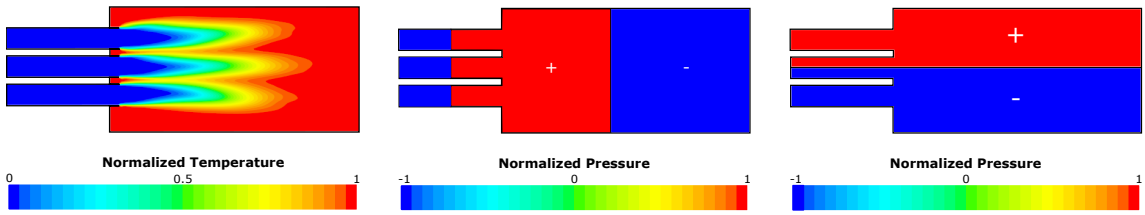

(a) Flames **(b)** Longitudinal mode **(c)** Transverse mode

Figure 1.2: An example of three flames burning in a combustor and how a longitudinal and transverse wave could look like

To reduce the amount of emitted NO_x, gas turbine manufacturers have moved from diffusion flames in the combustion chamber to lean premixed flames. Lean premixed flames reduce the amount of produced NO_x, because there are less local hot spots and the excess air cools the flame [5]. Unfortunately, lean premixed combustion systems are vulnerable to thermoacoustic instabilities [7]. Thermoacoustic instabilities are caused by the coupling between the flames and acoustic waves in the burner. These acoustic oscillations can be so significant, that they could potentially destroy a combustion chamber. For example, the famous F-1 Engine, which powered the Saturn V rocket, suffered from thermoacoustic instabilities with amplitudes as high as 100% of the mean combustor pressure during the test phase [8], resulting in many destroyed engines.

The newest model of the SIEMENS can gas turbine is shown in Figure 1.1. The flames anchor in the cans, which are approximately cylindrical shaped. The thermoacoustic instabilities occur mostly, but not limited to, in the cans. In this thesis only the thermoacoustic instabilities in a can are investigated.

Acoustic waves can propagate in multiple directions, namely the longitudinal (Figure 1.2b, the pressure distribution is in axial direction), the transverse (Figure 1.2c, the pressure distribution is perpendicular to the flames) and radial direction. The causes and symptoms of the longitudinal acoustic instabilities in a can combustion system are mostly known [9–12]. In contrast, the transverse and radial acoustic instabilities in a can gas turbine combustion system have only recently received attention [13, 14] and the root cause of these instabilities is not yet understood. Generally, the transverse and radial acoustic modes in an industrial combustion chamber occur at high frequencies ($> 1000\ Hz$) [15].
In order to prevent the gas turbine from being damaged by acousic waves, damping is added to the system. For example, the developers of the F-1 engine implemented baffles [8, 16, 17] to damp the transverse oscillations. After many tests, they got the engine to operate stable enough.
The goal of this thesis is to gain more insight in the damping ability of the baffles. Subsequently, a study into the mechanisms responsible for the transverse modes is conducted.

The research in this thesis is mostly performed by means of Computational Fluid Dynamics CFD, which is a powerful tool to predict thermoacoustic behaviour of a system. Especially LES have proven to be able to accurately simulate thermoacoustic instabilities [18–21]. LES solves in the time domain, which requires heavy computational power. An interesting new approach is to make use of solvers which solve in the frequency domain. Solving in the frequency domain

enables developers to optimize their burners with significantly less computational power. In this work, the acoustic module from COMSOL Multiphysics is used to compare LES with the results from a Helmholtz solver.

1.1 Problem Definition

Most gas turbine combustion chambers are designed in such a way that the longitudinal instabilities are of lesser influence. However, transverse acoustic waves are still a major concern. The current knowledge about the origin and behaviour of these transverse acoustic waves is limited. Furthermore, state of the art damping measures in the gas turbine combustion chambers are not optimal. The damping devices consume a significant amount of cooling air, resulting in a direct loss of power output. Adding baffles to a system has the potential to eliminate transverse oscillations, while keeping cooling air consumption low. A schematic overview of how baffles and resonators in a combustor look like is shown in Figure 1.3. Further research is required into the damping ability of introducing baffles in a combustion chamber.

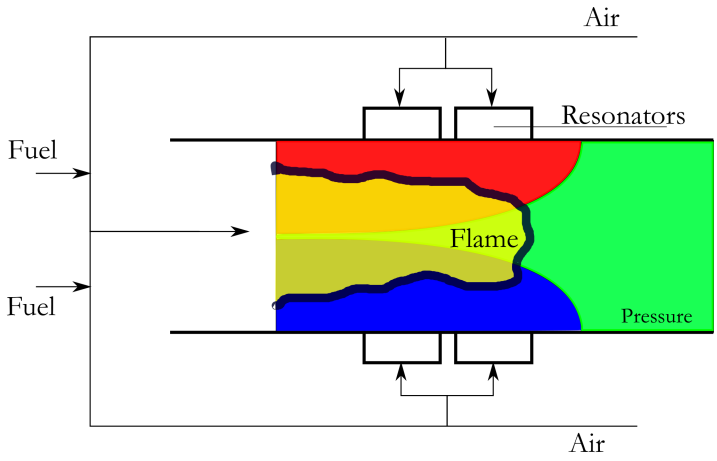

(a) A combustion system with resonators

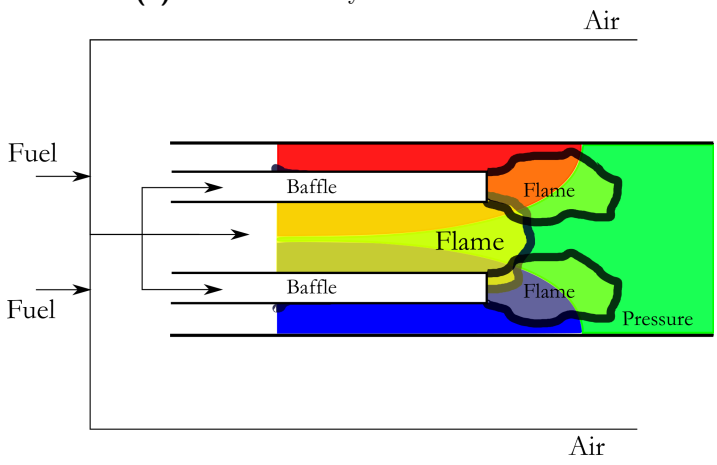

(b) A combustion system with baffles

Figure 1.3: Schematic overview of two different thermoacoustic damping strategies

1.2 Research Objective

The objective of this research is to gain more insight in High Frequency Dynamics (HFD) in an industrial combustion chamber and what the damping ability of implementing baffles in a combustion chamber is. New research has provided more knowledge about transverse combustion instabilities. In this thesis, it is tried to reproduce what was observed in literature. In addition, with some new post processing techniques developed in this thesis, the current knowledge about HFD is hopefully extended.

1.3 Research Question

The primary research question in this thesis is

- What is the damping ability by baffles in a gas turbine combustion chamber with regard to transverse acoustic oscillations?

In order to fully answer the primary research question, more knowledge about the mechanisms behind the transverse acoustic oscillations is required. Therefore, three secondary questions are formulated to aid in this process

- What are the optimum settings for simulating transverse combustion instabilities?
- How do the flames couple to transverse oscillations and what does their spatial movement looks like?
- Can a method be derived to predict a priory which (transverse) eigenfrequencies of a domain are most likely to become unstable?

Chapter 2

State of the art / Literature review

Simulating combustion instabilities requires the accurate treatment of three important physical phenomena, namely turbulence, combustion and acoustics. In this chapter section 2.1 describes the equations behind a turbulent reactive flow and thereafter section 2.2 treats the modelling procedures.
Moreover, in this thesis the aim is to get insight in the thermoacoustic behaviour of a gas turbine combustion chamber. Therefor, knowledge about the fundamentals of acoustics is required, which is provided in section 2.3. In section 2.4 a brief description of the current knowledge about the driving mechanisms behind thermoacoustics can be found. The last section, namely section 2.5 discusses the current options for controlling thermoacoustics in a combustion chamber.

2.1 Governing Equations

The combustion process and the flow in the combustor handled in this report are fully turbulent. To model this, knowledge of fundamental equations for fluid dynamics as well as for combustion is required. Furthermore, acoustics are also governed by the same equations that govern a reactive flow. The following subsection provides a brief description of the governing equations for a turbulent reactive flow. In addition, the wave equation is derived from the governing equations.

2.1.1 Fluid Mechanics

This section covers the governing equations describing a reacting flow. The evolution of a reacting flow is governed by a set of transport equations. Namely the conservation of mass, momentum, energy and species. First the conservation of mass, which is expressed by the continuity equation

$$\frac{\partial \rho}{\partial t} + \nabla \cdot (\rho \vec{v}) = 0, \tag{2.1}$$

where ρ is the density and $\vec{v}$ the velocity of the flow. The conservation of momentum is given by

$$\rho \frac{D\vec{v}}{Dt} = -\nabla p + \nabla \cdot \tau + \rho \vec{g}. \tag{2.2}$$

The variable τ represents the stress tensor and $\vec{g}$ equals the acceleration due to gravity. The pressure is denoted by p. The conservation of energy is written in terms of specific enthalpy h for matters of convenience [22]

$$\frac{\partial (\rho h)}{\partial t} + \nabla \cdot (\rho \vec{v} h) = -\nabla \cdot \mathbf{q} - \tau : (\nabla \vec{v}) + \frac{Dp}{Dt}. \tag{2.3}$$

In this equation $\mathbf{q}$ denotes the heat flux and the second and third term on the right denote the enthalpy production due to viscous effects and pressure variations. Finally, the conservation equation for the species of mass fractions $Y_i = \rho_i / \rho$ with ρ_i the mass density for species i is [23]

$$\frac{\partial \rho Y_i}{\partial t} + \nabla \cdot (\rho \vec{v} Y_i) = -\nabla \cdot \vec{J_i} + S_{Y_i}. \tag{2.4}$$

Here, $\vec{J_i}$ denotes the mass diffusion, S_{Y_i} is the net rate of production of specie i by chemical reaction. Pressure, density and temperature are related to each other through the equation of state for ideal gasses. With R_0 being the specific gas constant and $\bar{M}$ the average molar weight of the mixture, the ideal gas law is defined as

$$p = \rho T \frac{R_0}{\bar{M}}. \tag{2.5}$$

The stress tensor τ from Equation 2.2 and Equation 2.3, using Stokes' assumption, can be described as

$$\tau = -\mu (\nabla \vec{v} + (\nabla \vec{v})^T - \frac{2}{3} (\nabla \vec{v}) \mathbf{I}), \tag{2.6}$$

where μ is the dynamic viscosity and $\mathbf{I}$ the unit tensor. This set of equations describes the physical governing equations of a reactive flow. The term S_{Y_i} in Equation 2.4 can be resolved, which requires tremendous CPU power [24], or modelled, which is described in section 2.2.

2.1.2 Wave Equation

The acoustic wave equation with source term can be derived from the conservation of mass and the momentum equation. Klein [25] describes a summary of how to derive the wave equation and his work is used as a guideline here. The first step is to take the time derivative of the mass conservation equation (Equation 2.1) and the divergence of the Navier Stokes equations (Equation 2.2) and subtract the results from each other

$$\frac{\partial^2 \rho}{\partial t^2} - \nabla^2 p = \nabla \cdot (\nabla \cdot (\rho \vec{v}\vec{v}) - \nabla \cdot \tau). \tag{2.7}$$

Then, the term $\frac{\partial^2 \rho}{\partial t^2}$ is moved to the right hand side. The term $\frac{1}{c_0^2}\frac{\partial^2 (p-p_0)}{\partial t^2} - \frac{\partial^2 \rho_0}{\partial t^2} + \nabla^2 p_0$ is added to both sides of Equation 2.7 and the result is

$$\frac{1}{c_0^2}\frac{\partial^2 p'}{\partial t^2} - \nabla^2 p' = \nabla \cdot (\nabla \cdot T) - \frac{\partial^2 \rho_e}{\partial t^2}, \tag{2.8}$$

where the subscript $_0$ stands for a constant in the far field, $p' = p - p_0$ is the acoustic pressure fluctuation, T is the Lighthill stress tensor [26] and ρ_e is the excess density, which reads as

$$\rho_e = \rho - \rho_0 - (p - p_0)/c_0^2. \tag{2.9}$$

The left hand side of Equation 2.10 describes the propagation of a pressure fluctuation with the speed of sound (c_0) through time and space. The right hand side shows two source terms. The first term is a flow noise source term and the second term the thermoacoustic source term. Klein [25] showed by an order of magnitude analysis that the noise source term can be neglected compared to the thermoacoustic source term. The thermoacoustic source term depends on the heat release q and the wave equation in the absence of a mean flow can then be written as

$$\frac{1}{c_0^2}\frac{\partial^2 p'}{\partial t^2} - \nabla^2 p' = \frac{\partial}{\partial t}\left[\frac{\rho_0}{\rho}\frac{\gamma - 1}{c^2} q\right]. \tag{2.10}$$

2.2 Computational Methods for Turbulent Reacting Flows

Two approaches to gain insight in the effects of thermoacoustic instabilities in a combustion system are experiments or simulations. Over the years, computational power has increased with such an amount, that numerical solvers are now a serious option to model complex combustion processes, including corresponding combustion instabilities [11]. Full scale experimental studies are costly compared to simulations [27]. During the design process of a combustor, the usual approach is to simulate as much as possible with numerical solvers and perform a full scale test when it has been fully designed. This research focuses on the simulating aspect of the design process. Therefore, this chapter is an outlay of several numerical approaches to aid the prediction of combustion instabilities and performance of the passive control options.

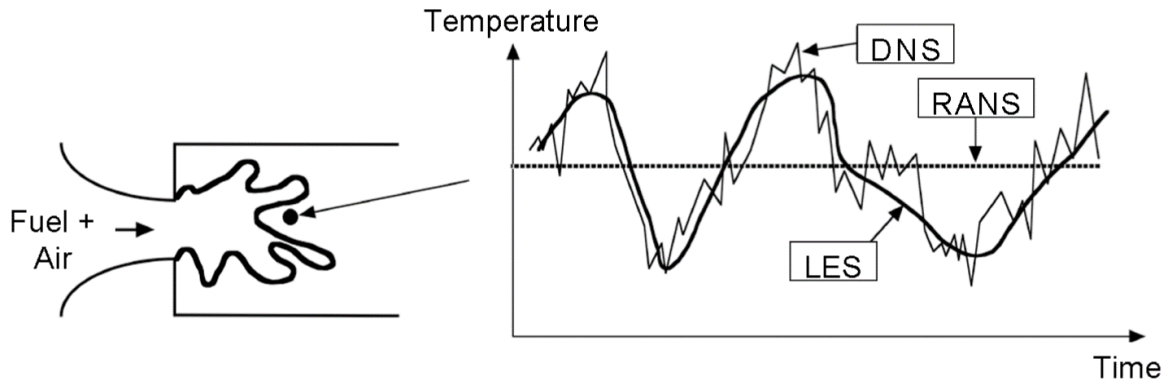

Figure 2.1: The output of a probe monitoring the temperature in front of a flame in a simulation. The output depicts the difference between RANS, DNS and LES.

2.2.1 Computing Turbulent Flows

Modelling turbulent flows has been studied for years and multiple methods for different ends have been developed. The difference lies in the fact that it is not always necessary to resolve all the scales. Often resolving the micro scale of turbulence, which is also computationally the most intensive, is not necessary. The user can decide which scales to resolve by choosing between methods. For example, to resolve all scales one can use Direct Numerical Simulation (DNS). LES can be used if only the macro scale needs to be resolved and the micro scale can be modelled. Reynolds Averaged Navier-Stokes (RANS) uses the time averaged values to predict the flow and thus does not return solutions per time step. Figure 2.1 is an overview of how the previous solvers provide output of a virtual temperature sensor over time.

All three methods are briefly described in this section. The main attention goes towards LES, because that is the method that will be used in this research for reasons listed above and below.

Direct Numerical Simulation (DNS)

DNS resolves both the micro and macro scale of turbulence, meaning that the equations from subsection 2.1.1 are applied to a discretized volume or surface without any modifications [28]. In order to do so, the spatial resolution has to be small enough to resolve the Kolmogorov scale η. The Kolmogorov length scale is given by [29]

$$\eta = \left(\frac{\nu^3}{\epsilon}\right)^{\frac{1}{4}}, \tag{2.11}$$

with ϵ, the dissipation rate, being

$$\epsilon \propto \frac{v'^3}{l} \propto v'^2 \frac{v'}{l} \simeq \frac{Kinetic\ energy}{Eddy\ life\ time} \tag{2.12}$$

and the factor $\frac{l}{u'}$ is the eddy life-time. Eventually the computational effort scales with $Re^{11/4}$, meaning that high Reynolds number flows are expensive to perform with DNS. Therefore, even though DNS can accurately predict the flow perturbations, it is not considered as a viable option for this research.

Reynolds Averaged Navier-Stokes (RANS)

RANS is the most widely used numerical turbulence approach in the industry. The computational effort of a RANS is low, because it uses ensembled averages to deduce the mean fields of the flow quantities. RANS decomposes velocity, pressure and temperature into an average and a fluctuation. The decomposition for a quantity ϕ looks like:

$$\phi = \bar{\phi} + \phi' \tag{2.13}$$

Where $\bar{\phi}$ equals the average of the quantity and ϕ' the fluctuating part. The idea is to use the decomposition on the Navier-Stokes Equations provided by Equation 2.2. The equations are then averaged and only represent the average turbulent flow [29]. Averaging the Navier-Stokes equations lead to a new unknown term $\overline{v_i' v_j'}$, also called the Reynolds stress term. The Reynolds stress term requires closure, due to newly introduced unknown quantities.

The output of a RANS simulation are the mean fields of the flow, whereas thermoacoustic instabilities in CFD require time dependent results. Therefore this method in the current form is not of interest for this research.

Large Eddy Simulation (LES)

First, a brief description of the basic principles of LES is given, later in this section the ability of LES to predict combustion instabilities is described in more detail. For the basic principles, the books from Nieuwstadt *et al.* [29] and Stephen B. Pope [28] have been used as main source of information. As stated before, LES resolves the large scales in a flow, while modelling the small scales, reducing computational costs considerably compared to DNS. To achieve this, LES filters the turbulent field with the formal description

$$\widetilde{\phi}(x_1, x_2, x_3) = \int\int\int G(\vec{x'} - \vec{x})\phi(\vec{x}) dx_1' dx_2' dx_3' \tag{2.14}$$

where $G(\vec{x'} - \vec{x})$ represents the filter function. In most cases, the filter has a value of $\frac{1}{V_f}$ inside volume $V_f = \Delta_f^3$ and zero outside V_f, which is centered around (x_1, x_2, x_3) from Equation 2.14. All fluctuations smaller than Δ_f are considered too small and modelled by the subgrid. The resulting velocity field is a product of the macro structure. Applying the filter to the equations in subsection 2.1.1, but now taking the integral form with the Einstein notation so it is applicable in CFD, with ˜ denoting the filter operations and introducing the subgrid stress τ_{sgs} as

$$\tau_{sgs} = -\rho_0 \left(\widetilde{v_i v_j} - \tilde{v}_i \tilde{v}_j \right). \tag{2.15}$$

The filtered Navier-Stokes can be written as

$$\frac{\partial \tilde{v}_i}{\partial t} + \frac{\partial \tilde{v}_i \tilde{v}_j}{\partial x_j} = -\frac{1}{\rho_0}\frac{\partial \tilde{p}}{\partial x_i} + \frac{\partial}{\partial x_j}\nu\left(\frac{\partial \tilde{v}_i}{\partial x_j} + \frac{\partial \tilde{v}_j}{\partial x_i}\right) + \frac{1}{\rho_0}\frac{\partial \tau_{sgs}}{\partial x_j}. \tag{2.16}$$

Similar to RANS, a closure problem is encountered here. The subgrid stress τ_{sgs} is an unknown quantity and has to be modelled. Popular methods are the Smagorinsky [30], the One Equation Eddy [31] and WALE models. Smagorinsky is the basic model used for subgrid modelling. The One Eddy Equation model predicts more accurate the pressure drops in a system [31] and the WALE model has higher accuracy in the vicinity of walls [32].

Subgrid Models

The Smagorinsky subgrid model is the oldest and best known model. Subgrid models such as the One Eddy Equation and Wall Adapting Local Eddy-Viscosity (WALE) origin from Smagorinsky. All three models provide closure for Equation 2.15. They share the first two steps, namely that the subgrid tensor can be modeled by

$$T_{sgs} = \frac{\tau_{sgs}}{\rho_0} = 2\nu_t \bar{S}_{ij} + \frac{1}{3}T_{kk}\delta_{ij}, \tag{2.17}$$

with

$$\bar{S}_{ij} = \frac{1}{2}\left(\frac{\partial \tilde{v}_i}{\partial \tilde{x}_j} + \frac{\partial \tilde{v}_j}{\partial \tilde{x}_i}\right), \tag{2.18}$$

where $\frac{1}{2}T_{kk} = \frac{1}{2}(\widetilde{v_k v_k} - \tilde{v_k}\tilde{v_k}) = k_{sgs}$ and k_{sgs} is the subsgrid scale kinetic energy. The common denominator of the three subgrid models, is how to handle the subgrid eddy viscosity ν_{sgs} and the subgrid scale kinetic energy.

- The first step in the Smagorinsky Subgrid Scale (SGS) model is to approximate the eddy viscosity by

  $$\nu_{sgs} = C_s \Delta \sqrt{k_{sgs}} \tag{2.19}$$

  and Δ is the grid size and C_s is a constant which can be calculated by

  $$C_s^2 = C_k \sqrt{\frac{C_k}{C_\epsilon}}. \tag{2.20}$$

  Both C_k and C_ϵ are also constants and have a value of 0.094 and 1.048 respectively. The SGS model assumes that the production and dissipation at the micro scale is in equilibrium. Therefore the subgrid scale kinetic energy can be written as $k_{sgs} = \frac{C_k \Delta^2 |\bar{S}|^2}{C_\epsilon}$ and Equation 2.19 is then

  $$\nu_{sgs} = (C_s \Delta)^2 |S_{ij}|. \tag{2.21}$$

- Instead of assuming equilibrium at the smallest scales, The One Equation Eddy subgrid scale model uses a transport equation to derive the subgrid scale kinetic energy of the flow [33]. The use of a transport equation over the assumption of local balance between production and dissipation results in higher accuracy for high Reynolds number flows and in coarse meshes.
- The WALE subgrid scale model was derived to have better subgrid scale performance in the vicinity of walls [32, 34]. This is achieved by taking into consideration both the strain and rotation rate of the smallest resolved turbulent fluctuations [35]. The two advantages of WALE over Smagorinsky are that the vicsocisty tends to zero in the vicinity of a wall and that the viscosity does not rely on information of the position and direction of the wall.

LES for predicting Thermoacoustic instabilities

Numerous studies have been conducted on the topic of prediciting thermoacoustic instabilities by means of LES. One of the first is the study by Veynante and Poinsot [36], which became a fundamental one. They used LES in combination with the artificial flame thickening model for combustion modelling, which is the same combustion model used for this study. The conclusion from Veynante and Poinsot [36] is that LES is able to predict combustion instabilities and that the Artificially Thickened Flame (ATF) flame model is a viable method to simulate combustion. In Angelberger *et al.* [37] it is proven that the method used by Veynante and Poinsot [36] also works with a more advanced chemistry model. However, forcing of the system was necessary in order to observe instabilities. Forcing or not forcing the system in simulations is an important aspect of the this study.

The most pressing question on LES is whether it is possible to simulate transverse combustion instabilities. Luckily it has already been done by Ghani *et al.* [38] and in Refs Wolf *et al.* [27, 39] for annular combustion chambers.
LES is a promising tool, being able to model perturbations in a turbulent flow, while keeping computational time low compared to DNS. Based on this, it has been decided to use LES for this research.

2.2.2 Computing Reacting Flows

Previous sections focused on the aspects of non-reacting flow and acoustics from a modelling perspective. It was stated, that thermoacoustic instabilities in a combustor couple with flames and therefore the flames have to be included in the CFD. The flames in this thesis are all perfectly premixed flames. Figure 2.2 depicts the spatial structure of a premixed flame entering the combustion chamber. Modelling combustion introduces new difficulties compared to modelling non-reacting flows, such as [23]

1. Chemical reactions with multiple species, where each specie must be tracked individually.

2. Reaction rates of each species have to be taken into account.

3. The system is more prone to modelling errors, due to the complexity of the combustion models.

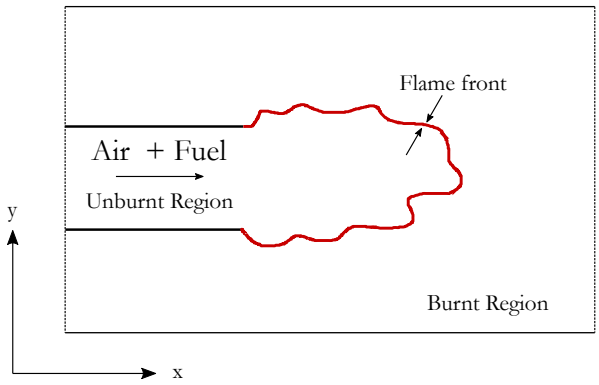

Figure 2.2: Structure of a premixed flame entering a combustion chamber

It is important to find an accurate combustion model in order to get realistic results of the coupling between flames and instabilities. The combustion models discussed in this section are especially applicable to premixed flames.

Reacting Rates

The cornerstones of a combustion process are the reaction rates. In Equation 2.4 the factor S_{Y_i} denotes the net rate production per species i. Then S_Y is the reaction rate of species i in a set of N reactions is given by

$$S_Y = \sum_{i=1}^{N} S_{Y_i}. \tag{2.22}$$

The individual reaction rates are defined as

$$S_{Y_i} = \nu_{Y_i} M_Y \left(k_{fi} \prod_k [X_i]^{\upsilon'_{Y_i}} - k_{bi} \prod_k [X_i]^{\upsilon''_{ki}} \right), \tag{2.23}$$

with M_{Y_i} representing the molar weights of species i, k_f and k_b the forward and backward rate coefficients of the reaction, X_i the molar fraction, whose definition is $X_Y = \rho \frac{Y_i}{M_{Y_i}}$. The remaining terms are the stoichiometric coefficients, $\upsilon_{ki} = \upsilon''_{ki} - \upsilon'_{ki}$. The rate coefficients constitute a central problem in combustion modelling according to Poinsot and Veynante [23]. The empirical Arrhenius law is a model method to determine the forward rate coefficient,

$$k_{f_i} = A_{fi} T^{\beta_i} exp\left(-\frac{E_k}{RT} \right). \tag{2.24}$$

and the backward rate depends on the forward rate through equilibrium constants

$$k_{bi} = \frac{k_{fi}}{\left(\frac{p_a}{RT}\right)^{\sum_{k=1}^{N} \upsilon_{ki}} exp\left(\frac{\Delta S_k^0}{R} - \frac{\Delta H_k^0}{RT} \right)} \tag{2.25}$$

Here p_a is the atmospheric pressure and ΔH_k^0 and ΔS_0^k are respectively the enthalpy and entropy changes for reaction i and these quantities are obtained from tabulations. In order to calculate the forward and backward rate coefficients for each reaction, data is required for A_{fk}, β_k and the activation energy E_k. Finally, the source term in Equation 2.3 can now be written as

$$S_E = -\sum_{i=1}^{N} S_{Y_i} \Delta H_k^0. \tag{2.26}$$

Normally this data can be obtained through experiments and compiled into tables. Numerical simulations require a chemical scheme containing all species and reactions, however already a simple $H_2 - O_2$ kinetic scheme consists of 9 species and 19 reactions [23]. Calculating the transport equation for all species containing multiple reactions is too time consuming and it will be shown that simplified models for this process are accurate while reducing computational time significantly.

Consecutively, the space and time scales corresponding to S_{Y_i} are typically small and therefore require fine meshes in order to resolve them. The central problem in numerical combustion revolves around finding adequate models to deal with the issues above. Combustion modelling is separated into two parts, namely the chemistry part and the flame propagation part. The chemistry part is done by Flamelet Generated Manifold (FGM) in this thesis and is discussed in the next subsection. Afterwards the flame propagation models are explained in more detail.

2.2.3 Tabulated Chemistry

An important observation in turbulent premixed combustion modelling is that the time scales of the chemical processes are much smaller than the mean flow time scales. As a result, it is possible to assume that the chemical processes are in steady state. However, the problem of deciding which species and reaction to take into account remains to be solved. With the focus on premixed methane-air flames, Peters and Williams [40] derived a method to simplify the kinetics for combustion of methane. It is shown that multiple reactions, at higher pressures, can be combined into a three-step mechanism simplifying the complete combustion of premixed methane. Unfortunately, even solving only these three reactions during run time is still computationally intensive.

Laminar Flamelets

The concept of laminar flamelets has been proposed by several authors, including Peters [41]. The main concept of flamelets in premixed combustion circles around the fact that the chemical reactions are fast compared to the time scales of turbulence, which is expressed by the Damköler number [41]

$$Da = \frac{\tau_t}{\tau_F} = \frac{v_l l_t}{v'_{rms} l_F}, \tag{2.27}$$

where τ_t the timescale for the turbulent motions is, τ_F the timescale for the flame time or also called the chemical time scale, l_t the length scale of the turbulent motions and l_F the length scale of the chemical processes. Respectively v_l and v'_{rms} are the notations for the laminar flame speed and the root mean square of the velocity fluctuations. Based on this, it has been observed that the burning region behaves asymptotically within a thin burning layer if the chemical time scale is much smaller than the convection and diffusion time scales. These layers are the definition of a flamelet. Together with the proposed simplification of the reaction schemes in Ref [40], the flamelet is an important and accurate simplification of combustion modelling.

Further requirements for the flamelet theory to hold is that the turbulent Reynolds number,

$$Re = \frac{v'_{rms} l_t}{\nu} > 1 \tag{2.28}$$

is greater than unity, to avoid laminar flames. In addition, the Karlovitz number,

$$Ka = \frac{\gamma l_F}{v_l} = \frac{t_F}{t_k} \tag{2.29}$$

should be small, so that the flame stretch remains weak. In the equations above, γ is the inverse of the Kolmogorov time $t_K = \frac{l_K}{v_k}$ and ν_k is the effective kinematic viscosity. The limitations mentioned above are depicted in the Borghi diagram (Figure 2.3) as the flamelet regime. There are indications though that the flamelet theory also holds for other regimes, such as the distributed reaction zones [43].

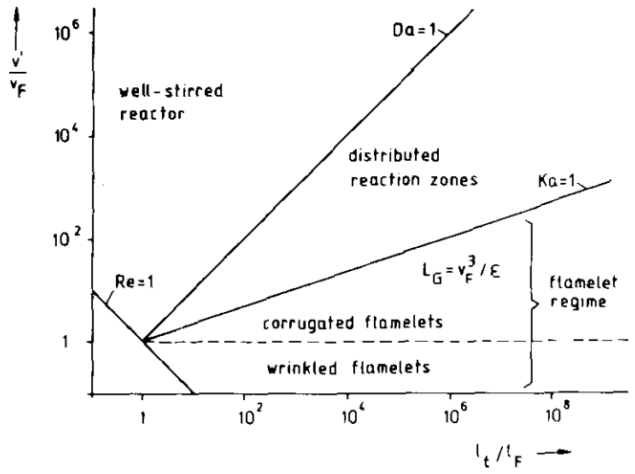

Figure 2.3: The Borghi diagram, taken from [41], first introduced by [42].

Flamelet Tables

FGM is based on the assumption that multidimensional flames may be described as an ensemble of freely propagating one dimensional laminar flames. As long as the chemical time scales remain small, compared to the time scales of turbulence, the reaction zone will remain laminar [22]. This is the case for large Damköler numbers, which relates the turbulent and chemical timescales. The one dimensional flames are tabulated with data from one dimensional laminar premixed flame using complex chemical models. Table generation is done by performing an one dimensional simulation of flamelets at constant equivalence ratio for the specified species [23]. Thereafter, the simulation is repeated for different equivalence ratios to form a n-dimension manifold. In this thesis the manifold is 2-D. The parameters defining the manifold are the mixture fraction

$$Z = \frac{m_{fuel}}{m_{fuel} + m_{Oxidizer}} \tag{2.30}$$

and the progress variable, also used in this work

$$c = \frac{Y_{CO_2}(Z)}{Y_{CO_2}^{max}(Z)} \tag{2.31}$$

The progress variable is the variable used in the tables to look-up how far the flame has progressed in space and what the corresponding states of the other species are. This is visualized in Figure 2.4 where the mass fraction of important species as a function of the mass fraction of CO_2 and velocity gradient a is given.

To account for non-adiabatic effects and heat loss or gain, enthalpy is added as another control variable. Generally the progress variable is not a fixed specie. A different specie can be used as progress variable depending on the personal preference of the user.

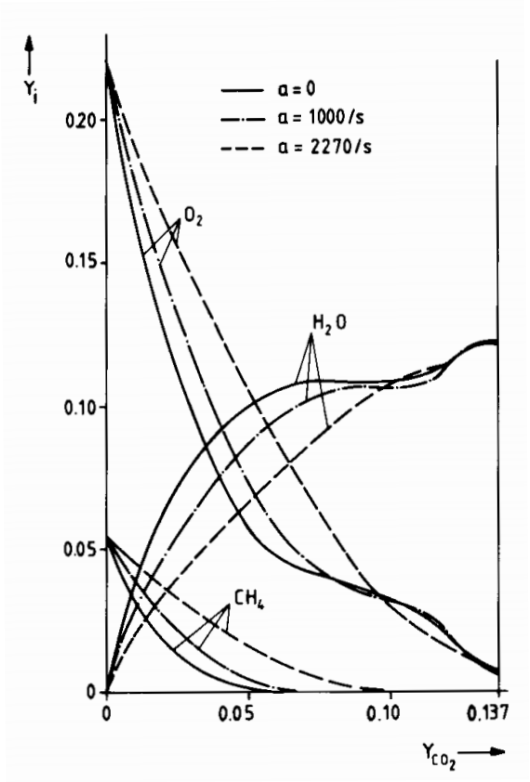

Figure 2.4: The mass fraction of important species as a function of the mass fraction of CO_2

2.2.4 Flame Front Propagation Models

In the previous section, it has been shown that it is computationally not feasible to solve Equation 2.4. Modelling the combustion mechanisms instead of solving all the reactions provides a solution. Several combustion models for (partially) premixed flame combustion have been developed. Knudsen and Pitsch [44] provide an overview of the most widely used combustion model. Three of them are described here.

- **FGM** Kinetic Rate [45], this model uses precomputed look-up tables containing the details of a set of asymptotic 1-D flames, which are mapped onto the 3-D field. Based on control variables such as the progress variable and the mixture fraction derived in CFD, the reactive source term is interpolated from the tables.
- **ATF** model. Due to the fact that the flame front is usually much thinner than the grid size, the ATF model thickens the flame, keeping the laminar flame speed constant over the flame front [46]. Then a reduced set of transport equations for a reduced number of chemical species are computed with the Arrhenius coefficients from the previous subsection. The ATF model can also be used in combination with FGM for quicker chemistry solutions [47, 48]. The ATF model requires a subgrid wrinkling model, or efficiency function to compensate for the thickened flame and the resulting loss of flame wrinkling.
- **Flame Surface Density (FSD)** model, or Turbulent Flame Speed Closure (TFC) [49, 50]. FSD also derives data from precomputed flamelets, but the combustion progress

is based on a precomputed laminar flame speed. It does not thicken the flame, rather directly determines the turbulent flame speed based on the changing laminar flame speed over the flame front and the local turbulence.

All three models can or must derive data from precomputed look-up tables. A brief explanation of how the tables are generated is provided in the next subsection. First the three flame models are discussed further, with extra detail given to ATF and FGM, because these models are used in this work.

Turbulent Flame Speed Closure (TFC)

Originally a model only compatible with RANS, Flohr and Pitsch [51] modified the model to be compatible with LES too. They derived a transport equation for the filtered progress variable. In the transport equation, closure is required for the chemical source term. This closure is based on the turbulent flame speed. In a LES this closure reads as

$$\frac{v_t^{\Delta}}{v_l} = 1 + A(Re_{\Delta} Pr)^{1/2} Da_{\Delta}^{-1/4}, \tag{2.32}$$

where v_l is the laminar flame speed, v_t^{Δ} the turbulent flame speed, Δ denotes the filter operator and A is a constant set to 0.52 [49]. TFC is computationally fast and robust due to the fact that only one extra transport equation has to be solved. Furthermore the model constant A can be changed to get accurate flame lengths [51]. Thermoacoustic instabilities have been simulated with TFC as flame model in for example Flohr and Pitsch [51] and Zhang *et al.* [52]

Artificial Thickened Flame (ATF)

The idea of the ATF, proposed by Butler and O'Rourke [53], is to thicken the flame, while maintaining the propagation velocity (the laminar flame speed). First, the scaling of the laminar flame speed and the laminar flame thickness is given by

$$v_l^0 \propto \sqrt{D_{th} B} \tag{2.33}$$

and

$$\delta_L^0 \propto \frac{D_{th}}{v_F^0} = \sqrt{\frac{D_{th}}{B}}, \tag{2.34}$$

where D_{th} is the thermal diffusivity and B is the reaction rate. Introducing factor F as the thickening factor, the laminar flame speed and flame thickness can be written as

$$v_l^1 = v_l^0, \tag{2.35}$$

$$\delta_l^0 = F \delta_l^0, \tag{2.36}$$

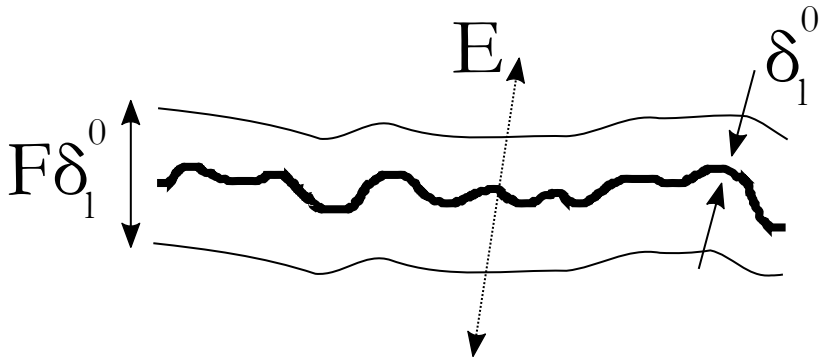

Figure 2.5: Overview of the ATF procedure

here, the subscript 1 stands for the thickened flame and 0 for a non-thickened flame. The visualization of the ATF procedure is provided by Figure 2.5. In this figure $F\delta_1^0$ depicts the thickened flame front, E indicates the regime where the error function works and δ_1^0 is the actual flame front.
If F is large enough, the flame front can be resolved on the mesh. However artificially thickening the flame eliminates the effect of flame wrinkling at the smallest scales. Furthermore larger eddies can now enter the thickened reaction zone, changing the flame-turbulence interaction. To account for these disadvantages of the ATF model, a closure model for the flame wrinkling is introduced. Such that the source term from Equation 2.4 becomes

$$S_Y^1 = \Xi^2 \frac{\alpha_l}{\alpha_{eff}} \frac{S_{Y^0}}{F} = \frac{E}{F} S_{Y^0}, \tag{2.37}$$

with α_l and α_{eff} being the thermal diffusivity in a laminar flame and the effective thermal diffusivity. Then $\alpha_{SGS} = \alpha_{eff} - \alpha_l$ and remaining unknown quantity is the wrinkling factor Ξ, to which the next subsection is devoted. Combustion instabilities have mainly been modelled with the thickened flame approach, see for example Wolf *et al.* [27], Veynante and Poinsot [36], Angelberger *et al.* [37].

Subgrid flame front wrinkling

Charlette *et al.* [54] proposed a subgrid wrinkling model based on a power law. Their derivation yields

$$\frac{v_t}{v_l^0} = \Xi = \left(1 + min\left[max\left(\frac{\Delta}{\delta_l} - 1, 0\right), \Gamma \frac{v'}{s_l^0}\right]\right)^{\beta}. \tag{2.38}$$

$\Gamma \frac{v'}{s_l^0}$ is an efficiency function describing the net strain effect of subgrid turbulent scales. The efficiency function relates the flame surface area to a cutoff length and limits the wrinkling at the smallest length-scales of the flame. β is the model constant, of which it is advised to set it to 0.5 according to Charlette *et al.* [54]. Lower Reynolds numbers most likely justify a higher model constant [55]. One of the advantages of the ATF approach with a subgrid wrinkling

model over the FGM model is that the model constant can be altered such that the flame lenghts can be changed to their correct lengths. The full derivation of the model can be found in Charlette *et al.* [54].

FGM Kinetic Rate

The FGM model solves a transport equation for the progress variable (Equation 2.31) to determine the location of the flame front. Consider a scalar variable Υ which assumes the value $\Upsilon_u = 0$ in the unburnt gases and $\Upsilon_b = 1$ for the burnt gases. The variable Υ can be any combination of mass fractions. Usually CO_2 is chosen, which aligns with the previously discussed progress variable. A flame surface is then defined as an iso-surface of Υ, resulting in $\Upsilon(x,t) = const.$ The transport equation is as follows

$$\frac{\partial(\rho\Upsilon)}{\partial t} + \nabla\cdot(\rho\vec{v}\Upsilon) - \nabla\cdot\left(\frac{\lambda}{Le_\Upsilon c_p}\nabla\Upsilon\right) - S_\Upsilon = 0, \tag{2.39}$$

where Le_Υ and S_Υ are respectively the Lewis number and the chemical source term. This approach is similar to the well known G-Equation model [56]. The chemical source term is calculated from the chemical kinetic reaction rate based on the progress variable, which is interpolated from the FGM table. The influence of turbulent fluctuations is modelled with statistically independent assumed shape Beta Probability Density Functions for the progress variable and a Delta Function Probability Density Function for the enthalpy. The equation for the chemical source term then reads as

$$S_\Upsilon = \rho\int\int S_{KR}(c,f)P(c,f)dcdf = S_{KR}. \tag{2.40}$$

Here, S_{KR} is the Kinetic-Rate flamelet source term from the flamelet tables and P the joint Probability Density Function of the progress variable c and the mixture fraction f. No literature is found up to now that has used FGM Kinetic Rate for simulating thermoacoustic instabilities in a gas turbine combustion chamber.

Table 2.1: Flame models comparison. The column Refs means which References have used the corresponding model for simulating thermoacoustic instabilities.

Flame Model	Model Constant	Complexity	Accuracy Slow Species	Refs
TFC	Yes	Single formula closure	Low	[51, 52]
ATF	Yes	Flame resolved on grid	High	[27, 36, 37, 39, 57, 58]
FGM Kinetic Rate	No	Turbulence quantities interpolated from table	Low	

2.3 Acoustics in a Closed System

In this section, a more in depth explanation of acoustics in a closed cylinder is given. The wave equation, Equation 2.10, with source term in the absence of a mean flow and assuming that all oscillations are harmonic was derived in section 2.1. The homogeneous part of the wave equation in cylindrical coordinates reads as

$$\frac{1}{\rho}\frac{\partial}{\partial\rho}\left(\rho\frac{\partial p'}{\partial\rho}\right)+\frac{1}{\rho^2}\frac{\partial^2 p'}{\partial\phi^2}+\frac{\partial^2 p'}{\partial z^2}+k^2p'=0, \tag{2.41}$$

which can be solved to derive a formula for a forward travelling acoustic wave in 1-D that reads as

$$p(x,t)=pe^{i(\omega t-kx)}. \tag{2.42}$$

It has been assumed that the pressure disturbance is infinitesimally small, it is isotropic, e.g uniform in all directions, and that the acoustic velocity is small compared to the sound of speed [59]. Due to these assumptions, this formula excludes viscous effects near walls and large-amplitude pressure oscillations. With $\omega=2\pi f$ and $k=\frac{2\pi}{\lambda}$ is the wave number. A time varying pressure fluctuation $p'(x,y,z,t)$ in 3-D can be expressed in the frequency domain as:

$$p'(x,y,z,t)=Re[\hat{p'}(x,y,z,t)]=Re[\hat{P}(x,y,z)e^{-i\omega t}] \tag{2.43}$$

Hat represents a complex variable and Re the real part of a complex variable. Combining Equation 2.43 into the left hand side of the wave equation (Equation 2.10) returns the Helmholtz equation for acoustics in cylindrical coordinates by

$$\nabla^2\hat{P}+\left(\frac{\omega}{c_0}\right)^2\hat{P}=0, \tag{2.44}$$

Based on the Helmholtz equation, the eigenfrequencies and eigenmodes can be found. In this thesis, the Acoustic Pressure (ACPR) module from COMSOL Multiphysics has been used to derive the eigenfrequencies of the numerical domain. The eigenfrequencies found by COMSOL are subsequently used as a sanity check for the LES calculations. Furthermore, an approach to predict in the frequency domain which eigenmodes are most likely to become unstable in the CFD of a combustion chamber is discussed in this work.

Gas turbine manufacturers prefer to know the eigenfrequencies of a combustor beforehand, so that they can predict where instabilities may arise. A cheap computational way to find the acoustic eigenfrequencies of a system is with an acoustic solver, such as the Helmholtz solver. It shares its fundamentals with Finite Element Method (FEM). The solution is then sought in the frequency domain. Compared to LES, this solver does not predict which modes are stable or unstable when no forcing is applied, it merely gives all the eigenmodes of the domain. Later on it will be showed that combustion instabilities almost always occur at an eigenfrequency of the domain. Searching only for the eigenmodes is computationally significantly faster than

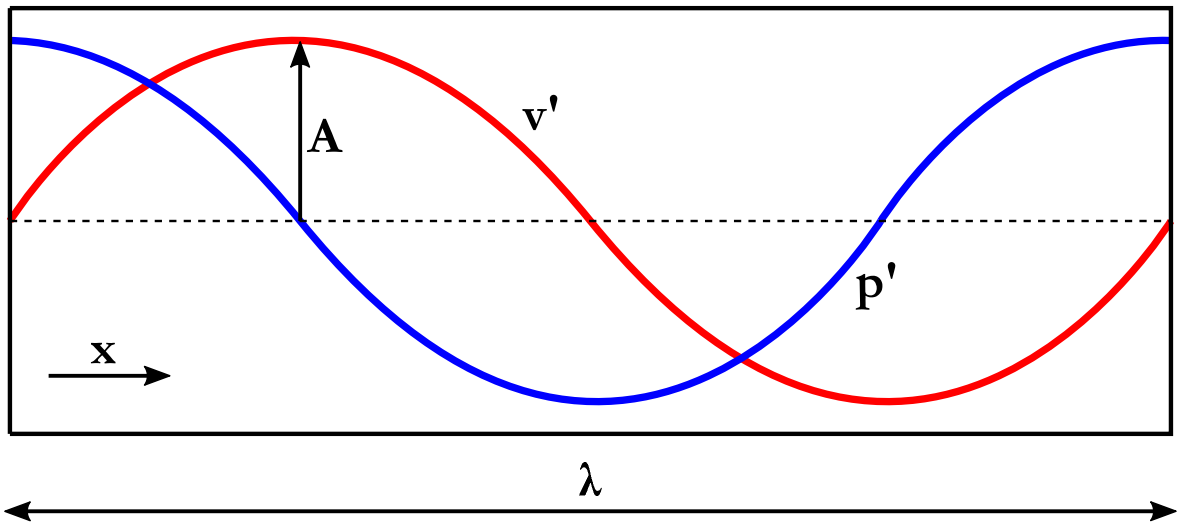

Figure 2.6: Closed system with an wave length equal to the domain length

performing an LES. Quite some research has lately been conducted predicting the stability of a system in the frequency domain, which requires extensive modelling procedures [39, 60–64].

A solution found for Equation 2.42 can be written as

$$f = \frac{c_0}{\lambda}. \tag{2.45}$$

Here, c_0 is the speed of sound and has different values depending on the medium and temperature. The formula couples the wave length and its corresponding frequency based on the properties of the medium.

In this study, acoustics will be explained on the basis of the geometry of a closed cylinder, because the SIEMENS combustion chamber is also approximately cylindrically shaped. Eigenfrequencies of a system are the frequencies at which a system tends to oscillate without any driving force. In 1-D, eigenfreqencies are the frequencies of which the corresponding half wave length or multiples of half wave lengths equal the length of the system. See for example Figure 2.6, a fully closed 1-D system, where the full wave length is equal to the length of the system. The blue line represents the deviation in pressure and the red line the deviation in velocity, also called acoustic pressure and acoustic velocity and A denotes the amplitude of the wave. The acoustic velocity flows between high and low acoustic pressure and therefor has a phase shift of 90 deg with the acoustic pressure. The pressure distribution of an eigenfrequency is also referred to as the eigenmode.

Figure 2.6 also depicts that near the walls the pressure has either a maximum or a minimum, while the velocity fluctuation is zero. The medium can not flow through the wall and the velocity goes to zero. In a closed (1-D) system, the velocity fluctuations are always zero at the walls and the pressure fluctuations are at a maximum.

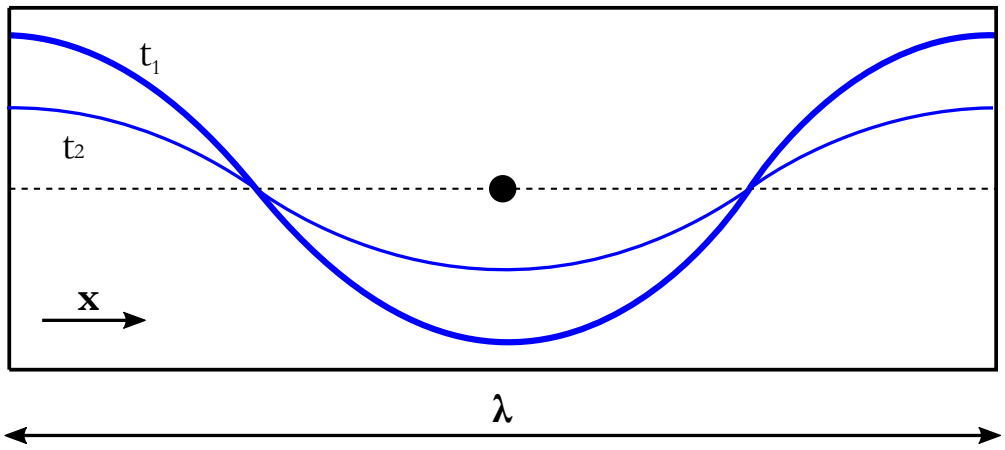

Figure 2.7: A standing wave at two points in time

2.3.1 Spatial structure eigenfrequencies

In the previous subsection, it was derived that a wave in a closed system has a pressure maximum at the wall and the wall-normal velocity fluctuations must be zero. Therefore, the wall-normal gradient of the pressure must always be zero at the wall. The result is that the points of low and high pressure are fixed in space. This is the definition of a standing wave, depicted in Figure 2.7. The black dot denotes the spatial position of the fixed pressure maximum, which is also called the pressure anti node. Both walls are also pressure nodes. It can also be derived from Figure 2.7 that there are two positions where the pressure is always zero. This is where the lines intersect. The zero pressure positions fixed in space are also referred to as pressure nodes.

When a standing wave occurs, it is always at an eigenfrequency of the system [65]. Predicting which frequencies are an eigenfrequency in a closed system can be done by

$$f = \frac{nc_0}{2L}, \tag{2.46}$$

with c_0 the speed of sound in the medium, L the length of the domain and n the factor indicating what the mode order is. This formula holds for longitudinal waves in a (1-D) domain. However, in a 3-D domain, next to longitudinal waves also transverse and radial waves occur. Figure 2.8 provides an overview of the pressure distributions in 3-D for a longitudinal, transverse, radial and a combination of the first two for a cylinder.

In a cylinder, the eigenfrequencies are not necessarily all standing waves anymore. Usually the longitudinal eigenfrequencies in a domain are standing waves, but a transverse wave could also for example also travel in circumferential direction in a cylinder. In Figure 2.9 the pressure distribution and wave propagation direction in a slice of a cylinder is shown for both a standing and a rotating wave. In fact, there are multiple ways how an acoustic mode can present itself in a cylinder [65]

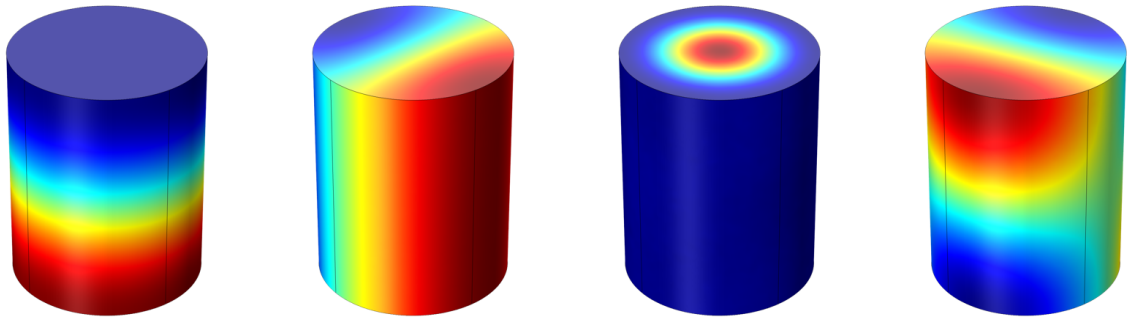

Figure 2.8: Acoustic Eigenmodes in a closed system. From left to right, a longitudinal mode, a transverse mode, a radial mode and a combined mode with a longitudinal and a transverse component. Red means it has positive amplitude, blue is a negative amplitude.

Standing Pressure nodes and anti-nodes are fixed in space.

Turning or **Spinning** Pressure nodes and anti-nodes are turning at the speed of sound.

Rotating The pressure distribution is rotating at the transverse convective speed [39].

The above acoustic behaviour also exists in combustion chambers. For example Wolf *et al.* [39], Prieur *et al.* [66] discuss this for annular combustion chambers. While the geometry is therefore different, what they have observed is also of importance in this work.

The eigenfrequencies corresponding to the transverse and radial waves in a system depend on the circumferential length of the cylinder when they rotate. The corresponding frequency for the transverse and radial modes is then given by

$$f = \frac{c_0 \theta_{mn}}{2\pi r}. \tag{2.47}$$

Here θ_{mn} is the root constant of the Bessel Functions [67], which is a constant from a look-up table. Ultimately, Equation 2.46 and Equation 2.47 can be combined into a formula which

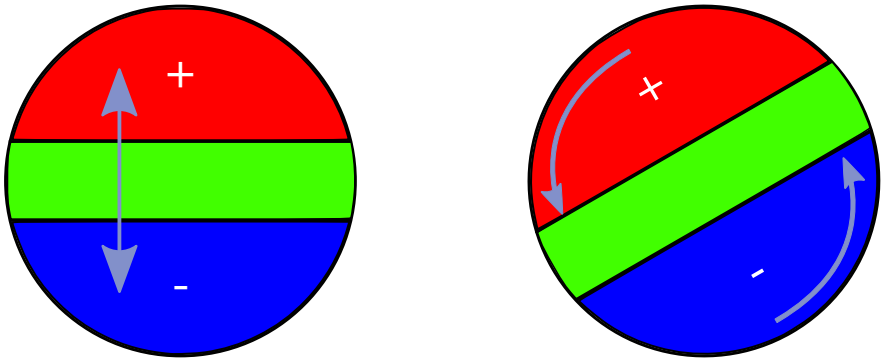

(a) standing wave **(b)** Rotating/Spinning Wave

Figure 2.9: The directions an eigenmode can move in

can predict any eigenfrequency of a cylinder, in any direction or combination. Namely by

$$f_{smn} = \frac{c_0}{2\pi}\sqrt{\left(\frac{s\pi}{l}\right)^2 + \left(\frac{\theta_{mn}}{r}\right)^2}. \tag{2.48}$$

In Equation 2.48, l is the length, r is the radius of the cylinder and s, m and n represent the integers corresponding to the longitudinal, radial and transverse direction. Prediction of eigenfrequencies and their corresponding mode shape for a cylinder can be done analytically, but for complex geometries the analytic derivation of eigenfrequencies is difficult and is usually done with a FEM solver such as COMSOL.

Transverse and radial acoustic eigenmodes start usually at a higher frequency than the longitudinal modes, due to the fact that the diameter of the combustion chambers are smaller than the length. Therefore the transverse and radial modes receive more attention than the longitudinal modes in this thesis.
Knowledge about how the instabilities behave is critical in order to control them. Prieur *et al.* [66] provides a good study on the behaviour of these acoustic instabilities. Further good articles on how acoustic modes look like are for example Refs. [20, 21, 68, 69].

2.4 Thermoacoustics

Thermoacoustic instabilities in a combustion chamber are the result of coupling between the heat release fluctuations of the flames and pressure fluctuations. The propagation and reflection of these pressure fluctuations, can cause severe damage to a combustion chamber [23, 68]. Usually, the instabilities align with the eigenfrequencies of the combustion chamber. The coupling of the heat release oscillations and the pressure oscillations is visualized in Figure 2.10 [8, 18, 70].

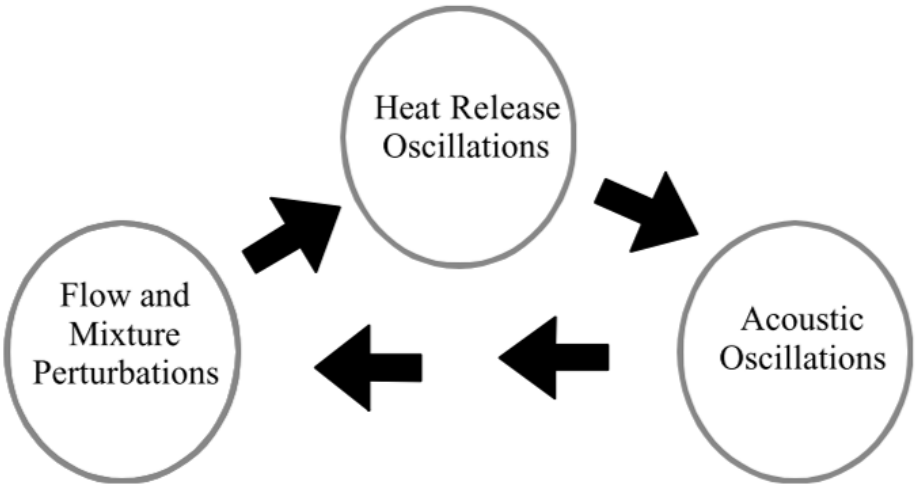

Figure 2.10: The thermoacoustic feedback loop in a combustion chamber, provided by Lieuwen and Yang [8]

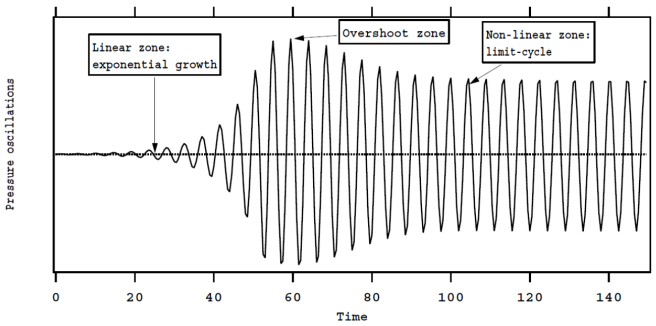

Figure 2.11: Limit cycle behaviour of combustion instability over time and its specifics. Found in Poinsot and Veynante [23]

2.4.1 Rayleigh Criterion

The fundamentals of combustion instabilities lead back to the so called Rayleigh criterion, derived by Lord Rayleigh [71] and is specified as

$$\int_0^\tau \int_V p'(\vec{x},t)q'(\vec{x},t)dVdt > 0. \tag{2.49}$$

When the pressure oscillations $p'(\vec{x},t)$ and the heat release oscillations $q'(\vec{x},t)$ are in phase at the flames, the system is unstable. This occurs when the result of Equation 2.49 is greater than zero [8, 70].
The Rayleigh criterion in this form is only eligible for ideal systems without any form of damping. For realistic cases, the acoustic losses have to be taken into account. To account for these energy losses an extended version has been derived [23] and can be written as

$$\frac{(\gamma-1)}{\rho_0\gamma}\int_V \int_0^\tau p'(\vec{x},t)q'(\vec{x},t)dtdV > \int_A \int_0^\tau p'(\vec{x},t)\vec{v}\cdot\mathbf{n}dtdA, \tag{2.50}$$

with V the combustor volume and T the period of the oscillations. It can be shown that in order for the system to become stable, the source term on the left, or the amount of energy fed to the system $\int_V p'qdV$ would have to be smaller than the acoustic losses, represented by the term on the right. At a certain point in time, the driving terms equal the damping terms and a limit cycle has been reached. How this looks like in the time domain is shown in Figure 2.11. The limit cycle behaviour is an integral part of thermoacoustics.

The next section describes multiple driving mechanisms for thermoacoustics. These driving mechanisms are more in-depth physical explanations of what is happening as coupling between acoustic instabilities and heat release fluctuations. As long as they full fill the Rayleigh criterion, they are considered as acoustic instability cause or effect.

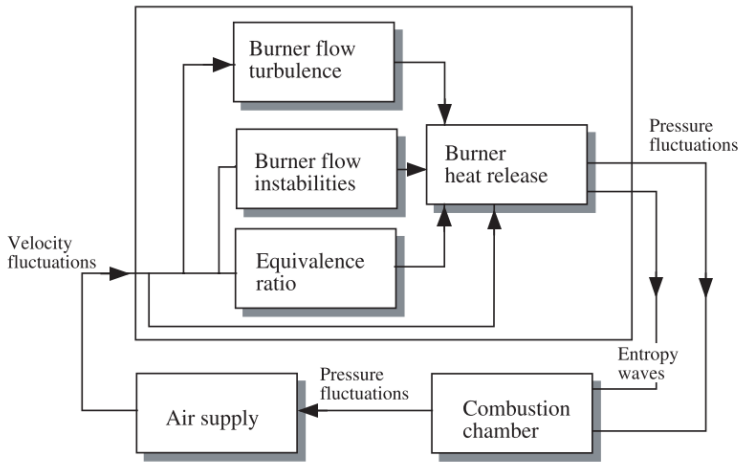

Figure 2.12: Elaboration on Figure 2.10, taking into account multiple driving mechanisms. Figure taken from Candel [9]

2.4.2 Driving Mechanisms of Thermoacoustics

The origin of thermoacoustic oscillations has been under debate for the past 70 years [9, 72]. Over the years, multiple mechanisms which are either a cause or a result of thermoacoustic instabilities have been found. This section describes the most widely known driving mechanisms and models behind it.

Sensitive Time Lag model

Combustion is a time dependent process and involves time lags. Systems which depend on time lags are prone to instabilities [9]. Based on this, the Sensitive Time Lag (STL) theory was developed during the 50's and 60's by Crocco and Cheng [73]. It is based on two parameters, amplification factor n and time lag τ. The time lag is a consequence of flame length and the geometry of the system and can be approximated or computed. An example of this is given in the Equivalence ratio fluctuations driving mechanism. The amplification factor n is unknown a priory and can either be set or derived from experiments and CFD. The instability mechanisms shown in the chain in Figure 2.12 are all based on a time lag and therefore directly related to the STL model.

Equivalence ratio fluctuations

A direct consequence of the STL model is the theorem about equivalence ratio fluctuations. Lieuwen and Zinn [74] point out that there is a relation between acoustics and a time-varying fuel and air mixture entering the combustion chamber [12]. Equivalence ratio fluctuations can only play a role in the instabilities, if they are driven by the combustion process and pressure oscillations and therefore close the feedback loop, not if they occur due to turbulent mixing.

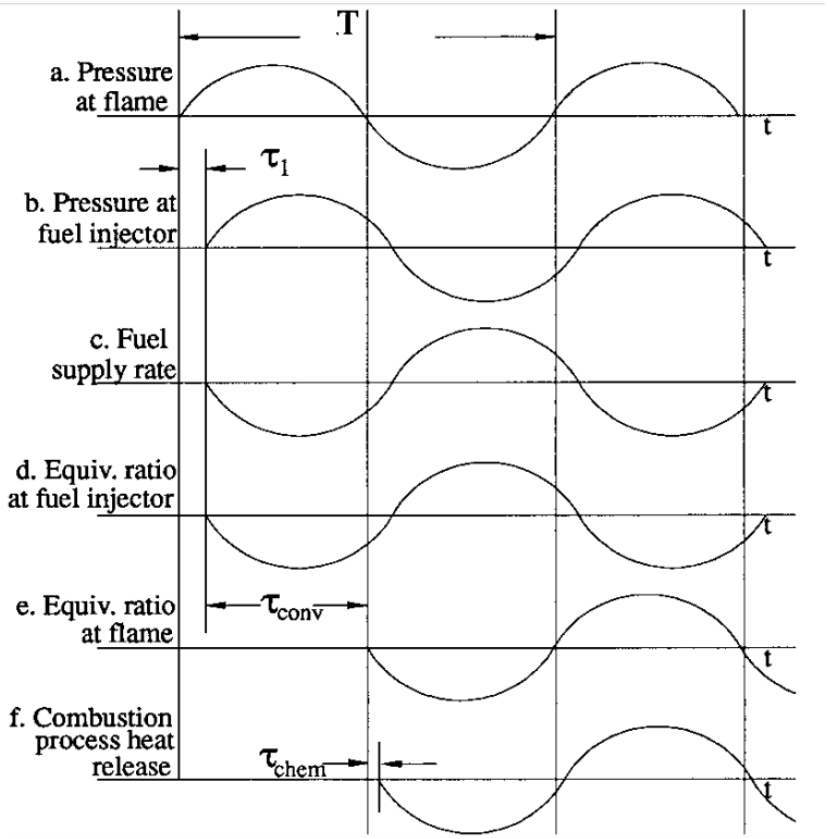

Figure 2.13: A description of the time lags responsible for the equivalence ratio fluctuations, taken from Lieuwen and Zinn [74].

Fluctuations in the supplied fuel and air cause equivalence ratio fluctuations according to Equation 2.51.

$$\frac{\phi'}{\bar{\phi}} = \frac{m'_f}{\bar{m}_f} - \frac{m'_0}{\bar{m}_0}, \tag{2.51}$$

where ϕ is the equivalence ratio, m_f the fuel mass flow, m_0 the mass flow of air and the quantities with a $'$ the fluctuations. Figure 2.13 provides an overview of how the mechanism of equivalence ratio fluctuations works. Consider an acoustic wave with period T at the flame. This wave will travel to the fuel inlet. The travel time is denoted as τ_1. At the fuel inlet, the pressure fluctuations caused by the wave influence how much fuel is inserted in the mixture. This variance in mixture is convected downstream to the flame. The convection time from fuel inlet to flame is τ_{conv}. The mixture is then burned and the duration is denoted with τ_{chem}. The convective time lag can be calculated as $\tau_{conv} = \frac{L_{inj}}{\bar{v}}$, where L_{inj} is the distance between the flame and the fuel inlet and $\bar{v}$ the mean convective velocity. The three times together can be transformed to a frequency by $f = \frac{1}{\tau_1+\tau_{conv}+\tau_{chem}}$. When this frequency aligns with a natural frequency of the system, the chances are high that this becomes an unstable longitudinal mode.

Flame-vortex interaction

Vortex interaction can drive multiple combustion instabilities. Vortex roll-ups are coupled with a longitudinal acoustic mode of the combustion chamber and are always in the low frequency range [9]. The vortex roll-ups change the flame surface area and cause an unsteady heat release [70]. The vortices grow downstream and only little is burned while moving downstream. Further away from the origin combustion place, the mixture is ignited, producing a pulse which can feed energy into one of the natural eigenfrequencies of the system [9]. Vortex shedding [75] is done at a certain frequency and some authors postulated that this is due to a Strouhal number of 0.1. However, this is not always the case and should not be considered as a fact. Generally, it is a combination of the acoustic eigenfrequencies of the system and the convective processes [76].

Intrinsic Thermoacoustics

Recent studies conducted by Hoeijmakers *et al.* [77], Emmert *et al.* [78] have brought to attention, that there may be another instability mechanism for thermoacoustics. Their studies focus on the effect of a flame without any reflective boundaries in axial direction, therefore there is no closed feedback loop anymore due to the fact that the acoustic waves, can no longer reflect back from the end of the combustion chamber to the flame. In this behavior, the acoustic waves are no longer considered as standing waves. The conclusion from these papers, is that a flame is intrinsically unstable, meaning that a flame can create its own local feedback loop, even if the acoustic waves do not travel back to the flame to perturb the heat release [79]. So far, this effect has only proven to be real for low velocities. It is difficult to depict this behaviour for high velocity flames. A study regarding this topic with velocities close to burner velocities would be very interesting. A brief summary of this behaviour is given by Poinsot [11].

Transverse oscillations

Up to recently, there was a lot of uncertainty with regard to HFD. In 2011, Schwing *et al.* [13] proposed a feedback mechanism, based on the creation of vortexes in the shear layer of the flame, close to the jet exit. The vortices are created due to the acoustic velocity of the transverse mode, deflecting the flow of unburnt mixture towards the front plate, shown in Figure 2.14. When the pressure sign switches sides, the vortices are forced back into the mean flow and convected downstream.
It is questionable whether this is the cause for HFD, or whether this feedback loop is responsible for the large amplitudes. It could very well be a side effect under the influence of transverse mode. No decisive evidence is provided in their paper.

A more promising model, predicting the HFD instabilities, is the flame centre oscillation induced by transverse acoustic velocity fluctuations [14]. Meaning that the heat release of the flame fluctuates in transverse direction on the same frequency as the active transverse acoustic mode. To capture and validate this effect will be one of the main targets of this thesis. A very important note Schwing and Sattelmayer [14] make, is that HFD is found in their setup for any swirl number, mass flow rate and preheat temperature. The only influence on the HFD

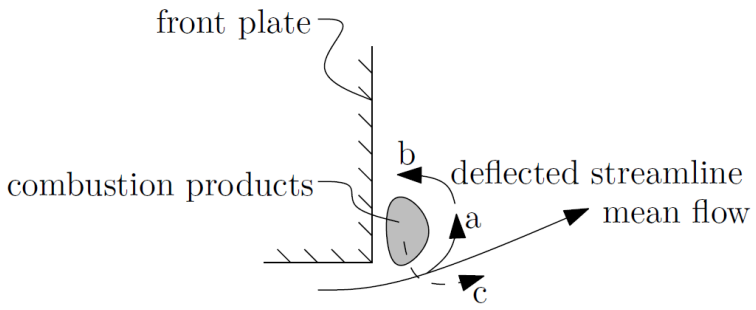

Figure 2.14: Sketch of the deviation of the mean flow in the shear layer of the flame due to pressure fluctuations, leading to the creation of vortices. Taken from Schwing *et al.* [13]

is the amount of thermal power. The higher the thermal power is, the more likely a system is to be unstable in the HFD range. The previous indicates that there may not necessarily be a characteristic time lag causing the high frequencies to be unstable. This is a very important conclusion, which will receive the necessary attention in this thesis. Furthermore, in Berger *et al.* [80], Hummel *et al.* [81] a model was proposed to predict which Eigen modes, especially the transverse modes, are unstable and their corresponding limit cycle amplitude. Their model is based on following observations:

- Flame displacement due to acoustic velocity fluctuations
- Flame deformation, induced by the displaced flame
- The mean heat release must overlap with the acoustic pressure mode
- Compact flame shape close to the burner outlet and chamber walls
- The higher the power density of the flames, the higher the limit cycle amplitude.

The proposed model is not implemented in this thesis and will therefore not be discussed in further detail. However being able to reproduce their observations in CFD is an important aspect of this work.

2.4.3 Terminology

Current terminology at SIEMENS splits the thermoacoustic behaviour in three frequency ranges based on frequencies of a combustion chamber of a Large Gas Turbine (LGT):

1. Low Frequency Dynamics (LFD), denoting the thermoacoustic behaviour below 100 Hz. The driving mechanisms behind this frequency range are not yet fully understood. The unstable frequencies in this range are also called system instabilities, as the wave lengths are so large that they usually travel multiple components of the gas turbine. Entropy waves for example cause LFD [82].
2. Intermediate Frequency Dynamics (IFD), representing the frequency range of 100 Hz $\sim$ 1000 Hz. Most of the mechanisms described above operate in the IFD range. In

this frequency range for the LGT of SIEMENS, the instabilities are always longitudinal and the wave propagation is parallel to the direction of the mean flow. The driving mechanisms from chapter subsection 2.4.3 drive the instabilities in this frequency range. These convective effects result in convective time lags.

3. HFD, usually used to describe frequencies above 1000 Hz and for this report the most interesting range. The wave direction for such frequencies is in the transverse direction of the mean flow. The wave lengths are thus so short, that they fit into the diameter of a combustion chamber.

2.5 Instability Mitigation

In order to run a lean premixed gas turbine at high efficiency and high power output, it is necessary to control the acoustic instabilities [12, 83]. Control can be done either active or passive. Active means that there are sensors and actuators, trying to interrupt the growth and sustainability of acoustic instabilities [76]. Active control was a solution SIEMENS used in the past [84], but is no longer of interest to SIEMENS in a LGT. Therefore active control is not discussed in this section. One could also tune a combustion chamber by changing the operating conditions or making use of fuel staging, but that option is not of importance for this work. Passive control consists of geometry modifications of the system or added hardware with damping capabilities and is the mitigation strategy described in more detail in this section.

Passive control contains no actuators or sensors, but relies on modifying the hardware. IFD instability mechanisms are mostly known and tackled by modifying hardware parameters such as the length between fuel inlet and combustion and the velocity of the mean flow through the jet carriers [74, 85]. So far, transverse combustion instabilities do not seem to depend on such hardware parameters. Therefor, in order to control the HFD combustion instabilities, while not being able to adjust the left side of Equation 2.50, the attenuation of acoustic oscillations has to increase. Two methods to achieve this, according to Culick [85] and Park [86]:

1. Resonators and Acoustic Liners
2. Baffles

It should be mentioned though, that Culick and Park describe ways of passive control for rocket engines. However, in terms of thermoacoustics, there are many similarities between rocket engines and gas turbine combustion engines. Therefor, passive control measures for rocket engines are also considered for gas turbines. Since the main goal of this study is to review the passive control abilities of the baffles, this will be the most thoroughly described passive control option. Resonators are also important though, as the baffles still need to prove itself to be an improvement compared them.

2.5.1 Resonators and Acoustic Liners

Resonators exist in different forms, but the most common one is the Helmholtz resonator [87]. The Helmholtz resonator is a passive control damping device and very practical to damp higher frequencies [12], due to the fact that higher frequencies tend to make the required

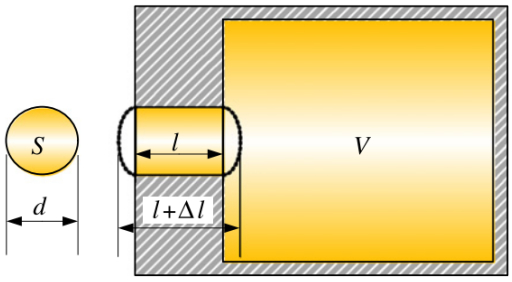

Figure 2.15: Schematic view of a typical Helmholtz resonator provided by [88]

volume of the resonator smaller. A Helmholtz resonator behaves like a mass - spring - damper system for acoustics. Certain wave lengths, depending on the geometry of the resonator, can push the air in the neck down. While the neck air is pushed down, the air in the volume is compressed. Thus the air in the neck is the acting mass and the air in the volume is acting as a spring. Not all frequencies are influenced by the resonator. The target frequency of a Helmholtz resonator can be calculated by Equation 2.52.

$$f = \frac{c_0}{2\pi}\sqrt{\frac{S}{Vl}}, \tag{2.52}$$

where c is the speed of sound in the medium, S is the cross section area of the orifice, l the length of the orifice and V is the volume of the cavity. Frequencies close to the calculated resonance frequencies will also be influenced by the Helmholtz resonator. Figure 2.15 is a schematic overview from of a Helmholtz resonator [88]. As stated before, Helmholtz resonators are typically used for higher frequencies.

Kim [88] provides a good study and an overview of the effect of Helmholtz resonators in a chamber. Cosic et all [89] give a more in depth review about the impact of flow effects on the acoustic damping capacity of the resonators. The problem with Helmholtz resonators is that they are placed on the combustor and in direct contact with the high temperature of the flame. Therefor the resonators have to be purged [90]. Usually the purging is done with air from the compressor and this fraction of air cannot be used anymore for combustion, thus lowering the output power of the gas turbine for a constant flame temperature [89].

Another type of resonators are quarter and half wave tubes. Half wave tubes are further examined by Park et all [91]. Sohn and Park compare the half wave, quarter wave tube and the Helmholtz resonators with each other [92]. They find that a quarter wave performs much better than a half wave tube in terms of damping. Furthermore they state that the Helmholtz resonator is the optimal choice, as it has the highest damping capacity and the most favourable geometry for a cylindrical combustor. Krebs at all [83] write about the implementation of Helmholtz resonators in a SIEMENS combustion chamber. The combustor with resonators is important for this research, because a baffled combustor should perform equally or better with regard to damping transverse thermoacoustic instabilities.

2.5.2 Baffles

The effect of baffles has already been thoroughly investigated for combustion chambers of rocket engines, but so far not for gas turbine combustion chambers. NASA [16, 17] summarized in 1972 and 1974 already what the effect of baffles on damping is and described some guide lines for designing baffled combustion chambers. They state, that baffles mainly damp transverse modes. In subsection 2.4.3 it was mentioned that HFD consists of transverse modes or combinations of transverse modes with radial and longitudinal modes, meaning that the damping induced by baffles will most likely only affect higher frequency instabilities.

Figure 2.16 is an example of how radial baffles with a baffle hub look like in a rocket chamber [93]. Comparing the configuration of the baffles with the pressure distribution of the first transverse mode in a cylinder (Figure 2.9) and keeping in mind that transverse modes can rotate in the combustion chamber [39], it is clear that the baffles are interfering in the pressure field of the mode. In order for the baffles to interfere with the transverse modes, the amount of radial baffles should at least be one order higher than the target mode and the number of baffles should be an odd integer. To achieve damping for the important first transverse mode, three baffles are required following the rules from Harje and Reardon [16]. Fortunately, the second transverse, consisting of four pressure anti-nodes, is also influenced by a configuration with three baffles, because the chamber is divided into three sections but the second transverse mode consists of four pressure anti-nodes. Generally, baffles also influence modes of an order higher than the amount of blades, but only if the order of the mode divided by the amount of blades it not an integer.

Harje and Reardon [16], NASA [17] described three mechanisms by which the baffles induce damping on transverse modes in a combustion chamber. The first is the way described above, by spatially interfering in the pressure field. The second mechanism is reduction of flow perturbations near the baffles. The third one, which was not fully understood at that time, was the dissipation of acoustic energy due to vortex generation and vortex destruction in the cavities between the baffles, this cavity is the parameter Δ in Figure 2.16. Furthermore, Feng *et al.* [94] state that the decrease in frequency of the oscillations is an effect caused by baffles and considered as an eliminating mechanism.

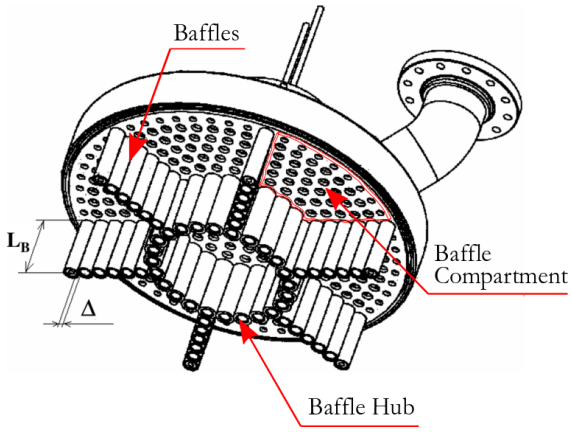

Figure 2.16: Schematic of a face plate with injector-formed baffles, provided by Lee *et al.* [93]

A summary of guidelines provided by NASA [16, 17] on how to design a combustion chamber with baffles to be most effective is given below.

1. Use an odd number of baffle blades to damp transverse modes, make sure that the amount of baffle blades divided by the order of the mode is not an integer.
2. To have a damping effect on radial modes, make a baffle hub at the velocity anti node, which would be in the centre of the burner for a gas turbine. The amount of hubs required is the same as the order of the target radial mode.
3. Consider designing the baffled compartments to be non symmetrical, tests have shown that damping is increased when the compartments are not equally spaced.
4. Avoid making too small baffle compartments, at some point adding more baffles will increase instabilities, not reduce them. The rule of thumb here is that the circumferential blade spacing divided by the target frequency's wave length should be between 0.2 and 0.4.
5. The baffles should extend close to the wall of the chamber.
6. Increasing the amount of baffles reduces the required length of the baffles. More baffles introduces more viscous damping in the baffle gaps. This effect will be thoroughly discusses further in this section. Being able to decrease the length of the baffles is important, as less baffle area is in the hot combustion zone, thus reducing the chance of thermal failure.
7. The optimal length of the baffles depends on the diameter of the combustion chamber. A length over combustion chamber diameter ratio between 0.2 and 0.3 is advised.

New research into the effect of viscous forces in the vicinity of the baffles have been conducted by Lee *et al.* [93] and Park *et al.* [59]. Lee *et al.* [93] found that, while changing the viscosity by changing the pressure in a cold acoustic test, the optimal baffle gap is somewhere in between 0.1 and $0.2mm$ for any level of viscosity, visualized in Figure 2.17. The main damping mechanism is the viscous dissipation occurring at the surface of the baffles. The gaps add extra damping by generating and destroying vortexes. For gaps larger than $0.2mm$, the acoustic waves can propagate through the holes and the extra damping by viscosity effects is smaller. In Park *et al.* [59] it was found with numerical solvers whether viscous forces have a big impact in a baffled configuration. They simulated it with a solver that in one scenario did not include viscous effects and in the other scenario did include viscous effects. It was shown that the solver with viscous forces indicated that a certain baffle gap produces a peak value of maximum damping, thus also indicating that the acoustics are largely influenced by the introduced viscosity near the baffles.

Furthermore they argue that introducing baffles lowers the transverse resonance frequencies, while the baffle gaps cause the resonant frequencies for transverse modes to increase in value. They further conclude that the optimum baffle gap size depends on the viscosity value and the optimum gap size increases with viscosity. Usually the viscosity in the burner is approximately five times higher than that of ambient air, resulting in an optimal baffle gap size of $0.2-0.3mm$. However, the change in viscosity is not paired with a change in pressure. Therefor, most likely, the results from Lee *et al.* [93] provides the optimal baffle gap size, but Park *et al.* [59] verify that viscosity is an important parameter for baffle gaps.

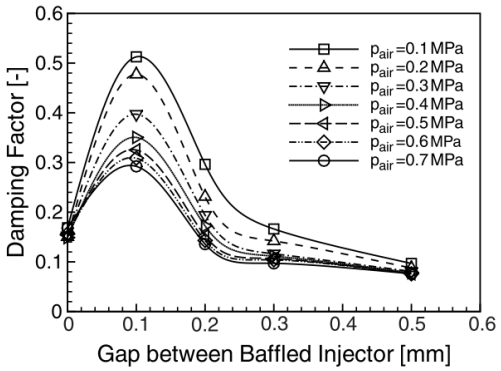

Figure 2.17: Damping factors for the first transverse acoustic oscillation as a function of baffle gaps for different viscosities induced by pressure differences. Provided by Lee *et al.* [93]

Important advantage of the increased damping caused by the baffle gaps, is that the length of the baffles can be reduced while maintaining or even increasing the same induced damping. Reducing the baffle lengths greatly reduces the thermal stresses at the baffle tips. The benefit of a baffled configuration compared to other configurations containing Helmholtz resonators or particulate matter lies in the amount of purge air required. Helmholtz resonators use quite an amount of purge flow, reducing the performance of a LGT. Baffles can be cooled with the air fuel mixture through the injectors. In theory there is no purge flow necessary. This would mean a larger increase of power output compared to the configuration using Helmholtz resonators as control devices.

Chapter 3

Solver Details

The accuracy of simulations of combustion chambers by CFD depends on the settings used for the calculations. Previous CFD simulations of LGT combustion chambers were not always successful in observing transverse combustion instabilities. Explanations could be that the discretization schemes were not correctly chosen, the grid size was too coarse or the chosen flame model is not suitable for simulating higher order thermoacoustic instabilities.
Furthermore, the flame shape in a CFD simulation is sensitive to chosen flame model and discretization schemes. It is assumed that the flame shape influences which eigenmodes can become unstable. Hence, this chapter covers an investigation in deriving the correct settings to simulate (higher order) transverse instabilities. For years, the CFD software OpenFOAM has been used by SIEMENS for LES calculations, but lately the computational solver StarCCM+ surfaced as an alternative. Both are addressed in this chapter.

This chapter is divided into two parts. The first section covers a detailed description of the discretization methods, wall functions and boundary conditions both CFD software packages offer. In the same section an introduction to numerical dissipation and numerical dispersion is given. Furthermore, a new excitation mechanism for triggering transverse oscillations in a simulation is introduced. With the help of this excitation mechanism, it is hopefully easier to observe HFD.

In the second part of this chapter, two validated approaches with regard to accurately simulating the flame shapes [95, 96] are tested for their performance on thermoacoustic instabilities. The simulations are conducted on a fraction (1/20) of the full domain of the S400, which is introduced in chapter five. This small domain will also be used for a mesh study with regard to flame length. The small domain will be described in more detail in the second part of this chapter.

3.1 Solving Methods

The previous chapter provided the theoretical outlay describing a fluid flow with combustion. The next step is to implement these formulas. The solving procedure can be divided into three steps. Namely:

1. Discretization of the partial differential equations
2. Pressure-Velocity coupling
3. Solving the resulting equations

3.1.1 Discretization

Currently three main approaches exist to approximate the set of equations computationally. These are Finite Differences (FD), Finite Elements (FE) and Finite Volumes (FV). Both OpenFOAM and StarCCM+ use the FV implementation. Therefor FV is the one that is explained here.
The first step in FV is to divide the domain of interest into a finite number of Control Volumes (CV). This is done by the mesh generator *snappyHexMesh* in this thesis. For each CV, the conservation equations are solved. Making use of Gauss's divergence theorem, the integral form of the transport equation for an arbitrary scalar quantity ϕ reads

$$\underbrace{\frac{d}{dt}\int_V \rho\phi dV}_{\text{Transient Term}} + \underbrace{\int_A \rho v\phi da}_{\text{Convective Flux}} = \underbrace{\int_A \tau\nabla\phi da}_{\text{Diffusive Flux}} + \underbrace{\int_V S_\phi dV}_{\text{Source Term}}, \tag{3.1}$$

where da is the surface vector, A the surface area of the CV and V the volume of the CV. The terms in Equation 3.1 have to be solved both in time and in space in a LES. The next sections describe in more detail what options there are for temporal and spatial discretization.

Temporal Discretization

In an unsteady flow, the set of equations in CFD are solved in time. There are multiple ways to do this. The options are divided by order. In this thesis, the discretization in time is either first order or second order. Higher order is possible, but not used due to the limited increase in accuracy while the computational time increased significantly [95].

- The simplest is the first order implicit discretization, also referred to as Backward Euler. Here ϕ is calculated by linear interpolation between the current time step $n+1$ and the previous time step n. With time step Δt, it is written as

$$\frac{d}{dt}\phi = \frac{\phi_{n+1} - \phi_n}{\Delta t} \tag{3.2}$$

.

- The second order accurate Backward Differencing Formula (BDF) is based on two previous time levels. The discretization is then

$$\frac{d}{dt}\phi = \left(\frac{3}{2}\phi_{n+1} - 2\phi + \frac{1}{2}\phi_{n-1}\right)\frac{1}{\Delta t}. \tag{3.3}$$

- The third option is to use a combination of the implicit scheme with an explicit scheme, also called Crank-Nicolson. Which is denoted by

$$\frac{d}{dt}\phi = \frac{f\phi_{n+1} + (1-f)\phi_n}{\Delta t}. \tag{3.4}$$

  Here, f represents the blending factor. $f = 0$ results in an fully explicit scheme and $f = 1$ equals a fully implicit discretization. A value between 0.8 and 0.9 for f is advised. Due to the combination of implicit and explicit, Crank-Nicolson is also second order accurate.
  The advantage of Crank-Nicolson over BDF(2) is the higher tendency to maintain numerical stability, while remaining quite accurate.

Crank-Nicolson is applied in the OpenFOAM calculations with a blending factor of 0.8. StarCCM+ does not contain Crank-Nicolson yet and therefore the BDF(2) temporal scheme is used.

Spatial Discretization

The convective flux requires solving in space. All the control volumes interact with neighbours and the border the control volumes share defines the influence they have on each other. The 2^{nd} order midpoint rule is applied to approximate the convective flux

$$\int_A J^\phi dA = \sum_f J_f^\phi a_f. \tag{3.5}$$

The total flux of J^ϕ is calculated by taking the sum of all the fluxes J_f^ϕ over all the cell faces f. In order to determine the fluxes, the cell centre values must be known. Figure 3.1 shows a 1-D grid, here α denotes a nodal variable and the subscripts U, C and D the upwind, central and downwind positions. At cell face f, the velocity v_f is known. A few discretization methods are summarized below.

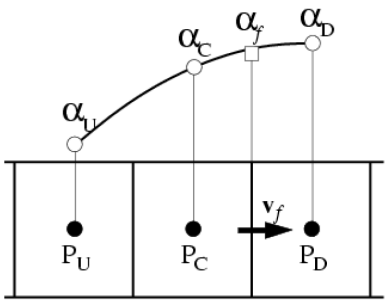

Figure 3.1: 1-D grid for convection, taken from StarCCM+ [97]

- First-Order Upwind (FOU) differencing scheme approximates the cell face value ϕ_f as a step function. It is first order accurate. Depending on the flow direction the convective flux is

$$(\dot{m}\phi)_f = \begin{cases} \dot{m}_f \phi_{f,0} & \text{for} \quad \dot{m}_f \geq 0 \\ \dot{m}_f \phi_{f,1} & \text{for} \quad \dot{m}_f < 0. \end{cases} \tag{3.6}$$

  A positive mass flux $\dot{m}_f \geq 0$ is leaving the cell and a negative mass flux $\dot{m}_f < 0$ enters the cell. The subscript 0 denotes the cell of interest and 1 the neighbouring cell. FOU is unconditionally bounded, making it numerically very stable, however the accuracy is limited with this first order approximation [97].

- Second-Order Upwind (SOU) differencing adds the gradients to the face values, so that $\phi_{f,0}$ and $\phi_{f,1}$ from Equation 3.6 become

$$\phi_{f,0} = \phi_0 + \mathbf{s}_0 \cdot (\nabla\phi)_{r,0} \qquad \phi_{f,1} = \phi_1 + \mathbf{s}_1 \cdot (\nabla\phi)_{r,1} \tag{3.7}$$

  with $(\nabla\phi)_{r,0}$ and $(\nabla\phi)_{r,1}$ denoting the gradients. The gradients can be derived with either the Hybrid Gauss-Lest Squares Method or the Green-Gauss Method. Both $\mathbf{s}_0$ and $\mathbf{s}_1$ represent the distance between cell centres.

- The Central-Differencing (CD) scheme derives the cell face center value by interpolating between the two nearest cell center values. The convective flux is then computed as

$$(\dot{m}\phi)_f = \dot{m}_f \left[f\phi_0 + (1-f)\phi_1 \right], \tag{3.8}$$

  where f is related to the mesh stretching. The CD scheme is second order accurate, but suffers from stability problems. The advantage over SOU, is that CD performs better in preserving the turbulent kinetic energy, making it a very useful scheme in a LES [98].

- The Bounded Central-Differencing (BCD) scheme combines the numerical accuracy of the CD scheme, but solves the stability problems by bounding it. The BCD scheme is

$$(\dot{m}\phi)_f = \begin{cases} \dot{m}_f \phi_{FOU} & \text{for} \quad \zeta < 0 \quad \text{or} \quad 1 < \zeta \\ \dot{m}_f \left(\sigma\phi_{CD} + (1-\sigma)\phi_{SOU} \right) & \text{for} \quad 0 \leq \zeta \leq 1. \end{cases} \tag{3.9}$$

  Here, ζ is a normalized variable based on local conditions and σ is a function of ζ such that $\sigma(0) = 0$ and $\sigma(\zeta) = 1$. A method to calculate ζ is

$$\zeta = \frac{\alpha_C - \alpha_U}{\alpha_D - \alpha_U}, \tag{3.10}$$

  where the values from Figure 3.1 are taken. To remain bounded, the scheme switches to a first-order upwind scheme when the convection boundedness criteria are not satisfied. On coarse meshes, the BCD can be more dissipative because of this switch.

Both OpenFOAM and StarCCM+ use the schemes above. In OpenFOAM, the BCD scheme is labeled as Gauss LimitedLineair and the FOU scheme is called Gauss Upwind.

3.1.2 Pressure Velocity Coupling

In an incompressible case, the Navier-Stokes equations do not provide a coupling between pressure and velocity. If the pressure field is known, the momentum equation provides the velocities, but the momentum equation does not explicitly contain the pressure. This problem can be solved by iterating until convergence is reached.

For compressible cases, the local density can be derived from the continuity equation. The density can be used to calculate the local pressure by solving the equation of state $p = p(\rho, T)$. Convergence and stabilization of the calculation can be enhanced using predictor-corrector schemes in combination with the equation of state. This approach is also defined as a Segregrated Flow. It is also possible to fully couple the pressure and velocity and convergence is reached by many iterations, which is referred to as the Coupled Flow approach.

Studies have shown that the difference in accuracy between both methods is negligible, while the Segrerated Flow option leads to a significant reduction in computational time [95]. As a result, in this framework a predictor-corrector approach is preferred. Three algorithms are used in this thesis, namely Semi-Implicit method for Pressure-Linked Equation (SIMPLE), Pressure Implicit Splitting of Operators (PISO) and PIMPLE, which is a combination of SIMPLE and PISO. SIMPLE, also referred to as Unsteady Implicit, was originally developed for steady state flows, but modifications to the pressure correction equation allowed for its use in transient flows. A flow chart, Figure 3.2, made by Indlekofer [95] explains the coupling methods in further detail.

Both algorithms start by guessing the pressure field p^*. Thereafter the discretized momentum equations must be solved in order to retrieve the velocity components u^*. The next step is to solve the pressure correction equation and then to correct the corresponding velocity fields. The SIMPLE algorithm checks at this point whether convergence has been reached, if not the loop can be repeated until the solution is converged.
The PISO algorithm checks convergence a step later, first another predictor-corrector step is performed. In theorem this leads to more computational time for the PISO algorithm. However there is a trade off, PISO requires usually less time to converge than SIMPLE. On the other hand, SIMPLE is able to handle higher Courant-Friedrichs-Lewy (CFL) numbers, while still providing high accuracy.

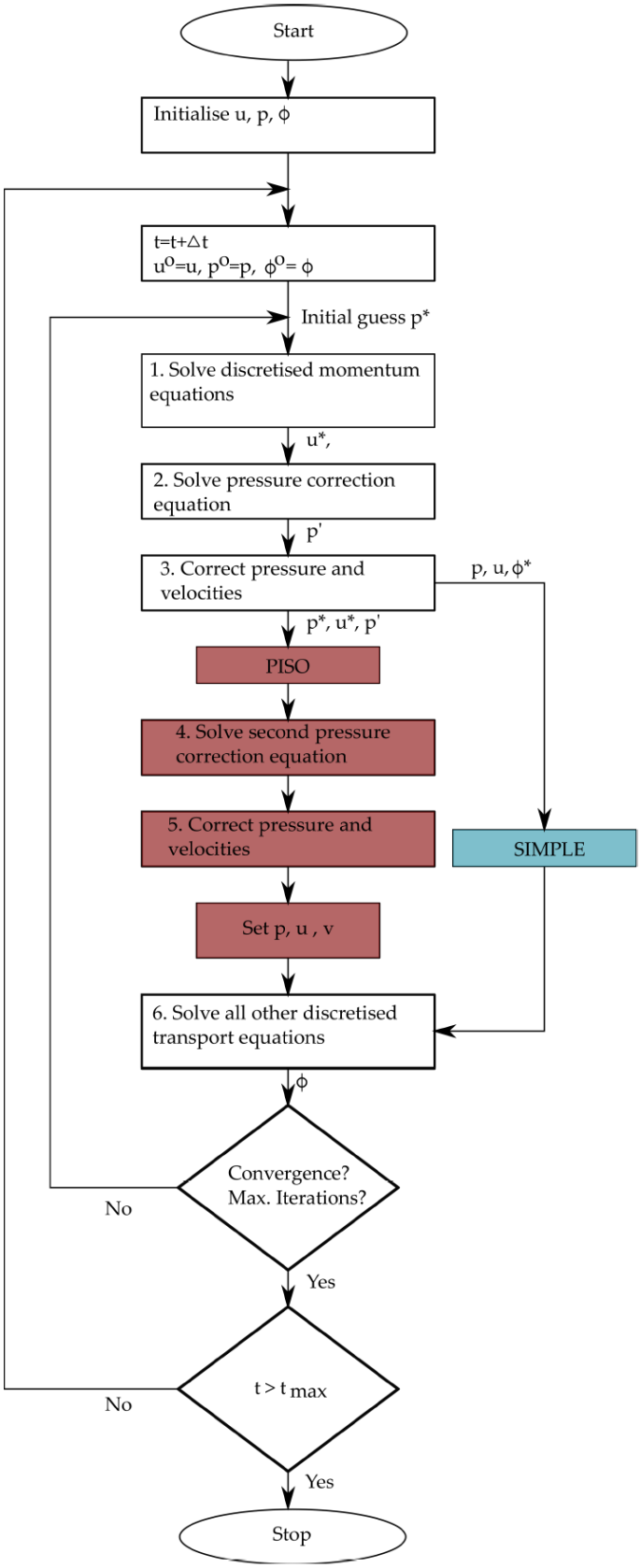

Figure 3.2: SIMPLE (blue) and PISO (red) captured in a flow chart, taken from Indlekofer [95].

3.1.3 Wall functions

In CFD, accurately solving at the walls is of utmost importance. In a turbulent flow, the walls are a source of vorticity. In combustion modelling, the amount of turbulence has a high impact on the flame shape. Therefor, an accurate prediction of flow and turbulent parameters across the wall boundary layer is essential. This can be done either by fully resolving the wall region, or by implementing a model. Resolving the wall is the most accurate approach, but requires that the first node in the grid is at $y^+ = 1$. For a RANS, where the total amount of cells is of less importance, it is a reasonable approach. However in a LES where the full domain is solved for every time step, the total amount of cells is a deal breaker. Wall functions are the preferred approach in a LES, to reduce to computational effort. For a full description on how wall functions work, the reader is referred to for example Refs [28, 29, 99]

OpenFOAM 2.4

The available wall functions in OpenFOAM can be divided into two groups, one calculates the value on the face of the first cell, the other calculates the value of the first cell centre. OpenFOAM allows for the important quantities to use separate wall functions. All wall functions are based on the Spalding Wall Law. The wall functions used in the simulations in this thesis in OpenFOAM are a pure zero-gradient boundary condition for the subgrid turbulence and a wall function that is based on the relation between u^+ and y^+ for the turbulent viscosity and turbulent thermal dissipation.

The logic behind the wall functions in OpenFOAM requires that the first node is always at least at values of $y^+ = 40$ or higher, else the results are inaccurate [99]. In reality this is difficult to achieve, the grid site is not uniform and the $y+$ value is also influenced by local fluctuations.

StarCCM+

In StarCCM+ it is not possible to set different wall functions for different quantities. One solution for the walls is to be chosen. The standard option is the all y^+ wall function, which is a hybrid treatment that uses a low y^+ value model for fine meshes and a high y^+ value model for coarse meshes. It also produces reasonable answers for meshes of intermediate resolution. When the wall-cell centroid lies within the buffer region of the boundary layer, a blending function is used to calculate the turbulence quantities. Figure 3.3 visualizes this approach.

3.1.4 Boundary Conditions

Thermoacoustic behaviour in a LES is influenced by the boundary conditions. It matters for example whether the inlet and outlet are reflective or non-reflective boundary conditions. The three boundary conditions of interest in this thesis are:

- The reflective boundary condition, or fixed pressure condition
- The non-reflective boundary condition
- Mass flow inlet

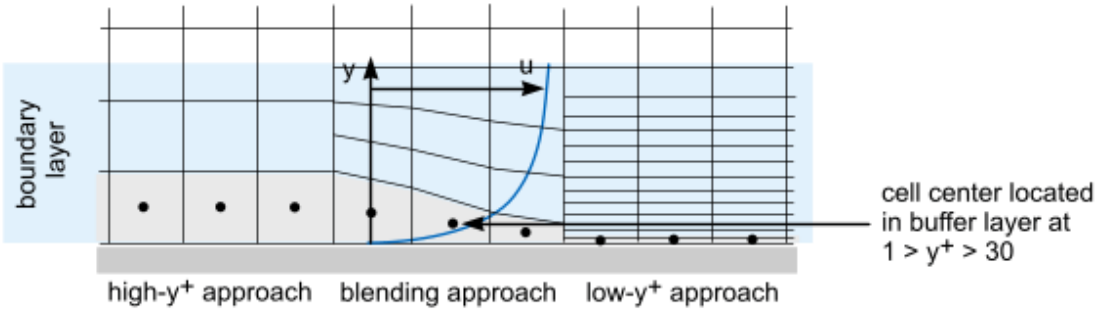

Figure 3.3: Overview of the hybrid wall function implemented in StarCCM+, taken from the StarCCM+ manual

Non-Reflective Boundary Condition

Unfortunately, StarCCM+ does not have a properly working non-reflective boundary condition [95] and a work-around is used in this thesis. OpenFOAM has two working non-reflective boundary conditions, which are called the Advective and the Wave Transmissive boundary conditions. Both solve the equation

$$\frac{D\phi}{Dt} \approx \frac{\partial \phi}{\partial t} + U_n \cdot \frac{\partial \phi}{\partial n} = 0 \tag{3.11}$$

Where it is assumed that the advection velocity is parallel to the boundary normal direction ($U = U_n$). In OpenFOAM, the advective boundary condition simply sets $U_n = u_n$, with u_n denoting the velocity normal to the boundary.
The Wave Transmissive sets $U_n = u_n + c$ and c, the speed of sound, is approximated here as $c = \sqrt{\gamma/\psi}$. Where γ is the ratio of specific heats and ψ compressibility.

StarCCM+ lacks a non-reflective boundary condition. The closest to a non-reflective boundary condition is the Freestream condition. The Freestream boundary condition is basically a zero gradient boundary condition when the flow leaves the domain or a fixed value when the flow enters the domain. However, the Freestream boundary condition causes the pressure in the domain to drift [95].
A method to overcome this, is to use a sponge layer at the outlet, as proposed by Indlekofer [95]. The sponge layer gradually adjusts the velocity near the outlet of the domain to a predefined value. The incoming velocity, and therefor also the pressure, fluctuations are smoothed out. The sponge layer introduces a source term into the momentum equation. Which reads as

$$S = k \cdot g(x)(u - u_{mapped}). \tag{3.12}$$

Equation 3.12 consists out of the strength factor k, the geometrical definition $g(x)$, the velocity in the LES v and a locally predefined velocity v_{mapped}. The geometrical definition is an exponential function (visualized in Figure 3.4) to smooth the incoming fluctuations out. As a result the pressure does not drift anymore.
The downside is that this method can only be used at the outlet of the domain. In some scenarios, a non-reflective inlet is desired. This is currently not possible in StarCCM+.

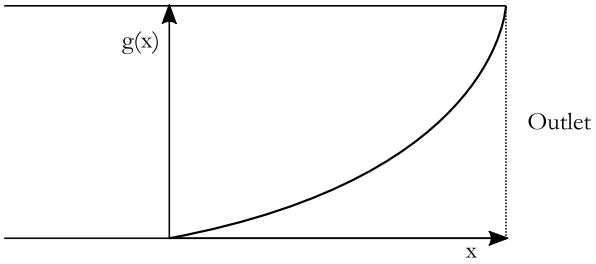

Figure 3.4: The spatial orientation of the sponge layer

Reflective Boundary Condition

The reflective boundary condition is a pressure outlet. The user specifies the pressure at the outlet and the solver will try to maintain that pressure. Incoming pressure waves will act as if the outlet is a wall and are therefor reflected.

3.1.5 Modelling Errors

Modelling of thermoacoustic instabilities requires an accurate treatment of the numerical terms. Numerical errors introduced by discretization methods must be reduced to a minimum. Typically two types of errors compromise the accuracy of a propagating wave in a numerical domain. Namely numerical dissipation and numerical dispersion. Numerical dissipation is associated with amplitude errors, while numerical dispersion causes phase errors. Figure 3.5 visualizes the stated numerical errors.

Three important parameters in the world of modelling errors with regard to wave propagation are the Courant number, the CFL number and the amount of cells per wave length. The Courant number is defined as [61]

$$Co = \frac{|v|\Delta t}{\Delta x} \tag{3.13}$$

and specifies the relation between the convective velocity, time step and mesh size. Large

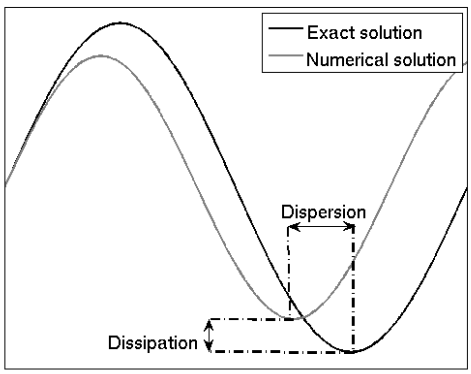

Figure 3.5: Definition of dissipation and dispersion, taken from Krediet [61]

values result in inaccurate results. As a rule of thumb in combustion modelling, $Co < 0.3$ is used in order to keep the simulations numerically stable.

$$CFL = \frac{(|v| + c_0)\,\Delta t}{\Delta x} \tag{3.14}$$

The CFL number depends on the speed of sound c_0 in combination with the convective velocity v. The influence of the CFL number and the amount of cells per wave length on the numerical dissipation and dispersion of propagating waves has been thoroughly investigated by Krediet [61] and his recommendations will be used as a guideline in this thesis. He derived for example that 50 cells per wave length and $CFL = 2$ results in no dispersion and only a small amount of dissipation. For 100 cells per wave length and $CFL = 2$ there is negligible dissipation.

3.1.6 Excitation Mechanisms

Usually LES simulations performed to capture thermoacoustic instabilities are so called self-excited simulations, e.g. there are no artificial perturbations added to the system. However, self-excited is not always sufficient to be able to observe all the unstable frequencies [100]. Sometimes, unstable transverse modes require a little push in the right direction. In order to push the simulated operating point over the edge, an artificial perturbation can be added to the system. Juniper [101] perturbed the system by applying background noise. As a consequence, more oscillations in the domain were recorded.

Urbano *et al.* [100] tried a different approach, namely to 'pressure bomb' the system. In the LES simulations conducted, a region of cells was set to its pressure plus an arbitrary amount of pressure. This sudden jump in pressure behaves like a bomb, explaining the name of the mechanism. The perturbation led to an increase of unsteadiness. The location of the pressure bomb can be freely chosen. Now this allows triggering a reaction of any eigenmode that the user would like to see. Pressure bombing is done for every geometry in this report. A full explanation how the pressure bomb works can be found in Appendix D.

3.2 Numerical Solvers and Parameters Study

The main target of this thesis is to simulate the effective damping on transverse oscillations by introducing baffles in a gas turbine combustion chamber. At the beginning of this chapter it has been stated that it is not trivial to simulate transverse instabilities in CFD. This section aims to derive the optimum flame model and settings to simulate HFD. For this investigation, a fraction (1/20) of the domain of a full combustion chamber of SIEMENS (the S400) has been taken.
The geometry of the S400 is different from what has previously been simulated by SIEMENS. The diameter of the jets is 10 mm in the S400 compared to the usual 20 mm or 40 mm. The smaller jet diameter introduces new uncertainties. A few of them summed up here:

- The diameter of the premix passages, also called ducts, is only 10 mm. The smallest duct diameter in previous simulations was 20 mm. Due to the smaller duct diameter, the flow in the ducts is less turbulent, as Reynolds number scales directly with the diameter. Furthermore a higher pressure loss occurs in the ducts. The question arises whether the old settings, tuned for the 20 and 40 mm ducts still provide accurate results.
- The space between neighboring flames can be as small as 4 mm. It is unknown whether the flames would merge into one big flame front or act as independent flames.
- There is no experimental data with regard to the flame shapes or lengths for the 10 mm ducts. Making it difficult to determine what is correct and what is not. Usually as a rule of thumb, there is a flame length over duct diameter ratio in the range of 4 to 7 [102].

The dimensions of the geometry of this sample case are taken in such a way that it is representative for the S400 and includes the difficulties specified above. Nine ducts lead out of a plenum with arbitrary radius into a rectangular flow box. The spacing of the ducts is exactly the same as in the S400. The size of the flowbox or combustion chamber is $340x65x60$ mm. The length of the ducts is 252 mm, which is a generalization of the geometry of the S400. The length of the combustion chamber is long enough to make sure flames do not extend out of the domain, but the refinement of the flame zones is only 200 mm downstream. Mixing is not resolved in all future simulations, a perfect mixture is assumed. Methane, CH_4, is the inserted fuel.

Everything that is required for accurately simulating the S400, is first tested on this smaller case. This way, all the important parameters can be investigated, while keeping computational costs low. All the simulations here are LES, because this is also the method that will be applied to capture the combustion instabilities of the S400. The presented case has been investigated in both OpenFOAM 2.4 and StarCCM+. Turbulent effects impacting combustion and thermoacoustic results derived in this section serve as lesson learned for simulating the S400.

3.2.1 Settings

The present section covers the choosen settings for the CFD calculations. The influence of selecting the right schemes and models is demonstrated by comparing velocity profiles through

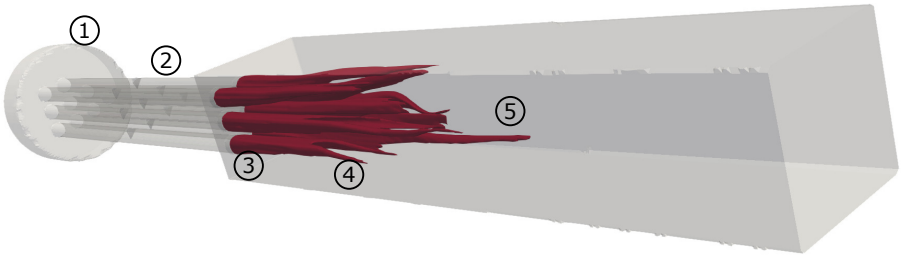

Figure 3.6: 3D overview of the sample case. The outer shell is made transparant and for an indication how the flames look like in the domain, the flames are also shown. The flames are derived by a first order upwind scheme. From 1 to 5 there is, the plenum, the ducts/jets, the jet exit, the flames and the combustion chamber.

the domain, flame shapes and the axial positions of centre of heat releases.

Pressure-Velocity Coupling

Both OpenFOAM and StarCCM+ make use of a segregated flow solver, meaning that a pressure-velocity coupling algorithm needs to be implemented. For OpenFOAM this is the implicit PIMPLE algorithm and in StarCCM+ the SIMPLE algorithm. The difference in pressure-velocity coupling here is based on the fact that there is no PIMPLE in StarCCM+, neither allows StarCCM+ to use PISO with a second order temporal solver. The difference in physical accuracy between the pressure-velocity coupling methods should be negligible according to Refs [103, 104], as long as convergence is reached.
Choosing between the coupling methods is a matter of convergence and computational time. In a LES, particularly in the simulations conducted in this report, the time steps are usually small to be able to resolve the physics of interest. For small time steps, SIMPLE is recommend over PISO to decrease computational time [98].

Flame models

Three combustion models have been described in subsection 2.2.4. In OpenFOAM, ATF in combination with FGM to handle the chemistry is the validated approach [96]. The subgrid wrinkling model constant is set to 0.5, which is in line with what the authors of the model recommend [54].
For StarCCM+, the only validated flame model was the FGM Kinetic Rate. No model constant has to be set.

Discretization

The discretization schemes used in OpenFOAM and StarCCM+ can be found in Table 3.1. The meaning of the names of the schemes was stated before in section 3.1.1. The reason for choosing Bounded Central Differencing over second order upwind for the convective part, is that the former model preserves the turbulent kinetic better energy [97]. Unbounded Central

Table 3.1: Discretization schemes used in the LES of the sample case

OpenFOAM 2.4		Scheme	Order
Temporal		Crank-Nicolson	$1^{st}/2^{nd}$ blend
Gradient	(default)	Gauss linear	2^{nd}
Gradient	(velocity)	Gauss linear, limited	2^{nd}
Convective	(default)	Gauss linear	2^{nd}
Convective	(velocity)	Gauss linear, limited	2^{nd}
Convective	(scalars)	Gauss linear upwind, limited	2^{nd}
Diffusive		Gauss linear, limited	2^{nd}
StarCCM+		Scheme	Order
Temporal		Backwards Differencing	2^{nd}
Gradient	(default)	Hybrid Gauss-LSQ	2^{nd}
Convective	(default)	Bounded Central-Differencing	2^{nd}
Diffusive		Bounded Central-Differencing	2^{nd}

Differencing for convection was never stable in neither OpenFOAM and StarCCM+, not even for fully developed solutions with an extreme small time step.

Subgrid Models

In StarCCM+ there is no option to choose the One Equation Eddy model, whereas in OpenFOAM 2.4 the WALE subgrid model is not available. The recommendation from Dederichs and Beck [102] to take the One Equation Eddy model for the OpenFOAM calculation has been followed up. In the StarCCM+ calculation, the standard recommendation is to use their WALE subgrid model, which is also the one used in the present section [97].

Mixing and Boundary Conditions

In order to reduce the complexity, mixing is not resolved in the simulations. All calculations were conducted with an initial perfect mixture condition. Furthermore, thermoacoustics influence the flame shape and the velocity profile. In order to prevent thermoacoustics, the outlet is set to Wave Transmissive for OpenFOAM. This is only done in the sections with regard to flame shapes. Later for the thermoacoustic comparison the outlets are both set to Pressure Outlet with a fixed pressure. In StarCCM+ the outlet is set to a Freestream condition, in combination with a Sponge Layer. Both inlets are Mass Flow inlets and are fully reflective. The walls are all adiabatic.

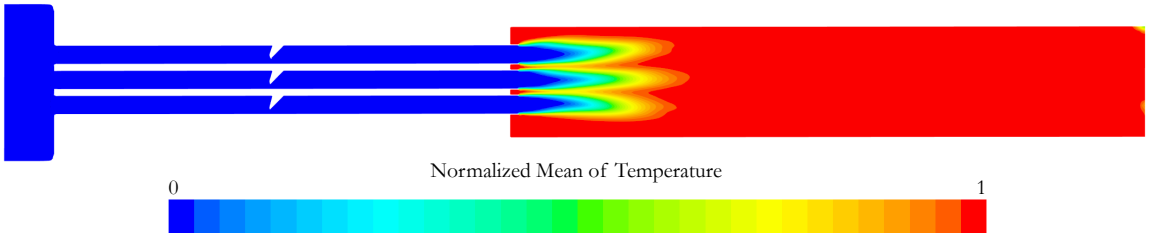

Figure 3.7: The normalized mean temperature field of a cut through of the sample case

3.2.2 Results

CFD calculations have been conducted in both StarCCM+ and OpenFOAM on the same mesh. Figure 3.8 depicts the importance of choosing second order for the convective schemes. It can be seen that there is almost no turbulence in the flow (right hand side Figure 3.8). The results origin from the OpenFOAM simulation, conducted with 14 cells per flame diameter, as advised by Dederichs and Beck [102] and Goeb [96]. The right hand side of the figure below indicates that the first order upwind scheme produces less turbulence than the second order scheme, resulting in nonphysically long flames, which can be seen in Figure 3.6. The mean velocity profiles both show a hump on the right side of the jet exits. This is caused by the vortex generators. Figure 3.7 shows the mean temperature field in a 2-D cut-through of the sample case, where it can be seen that the flames are not merged together in one flame front.

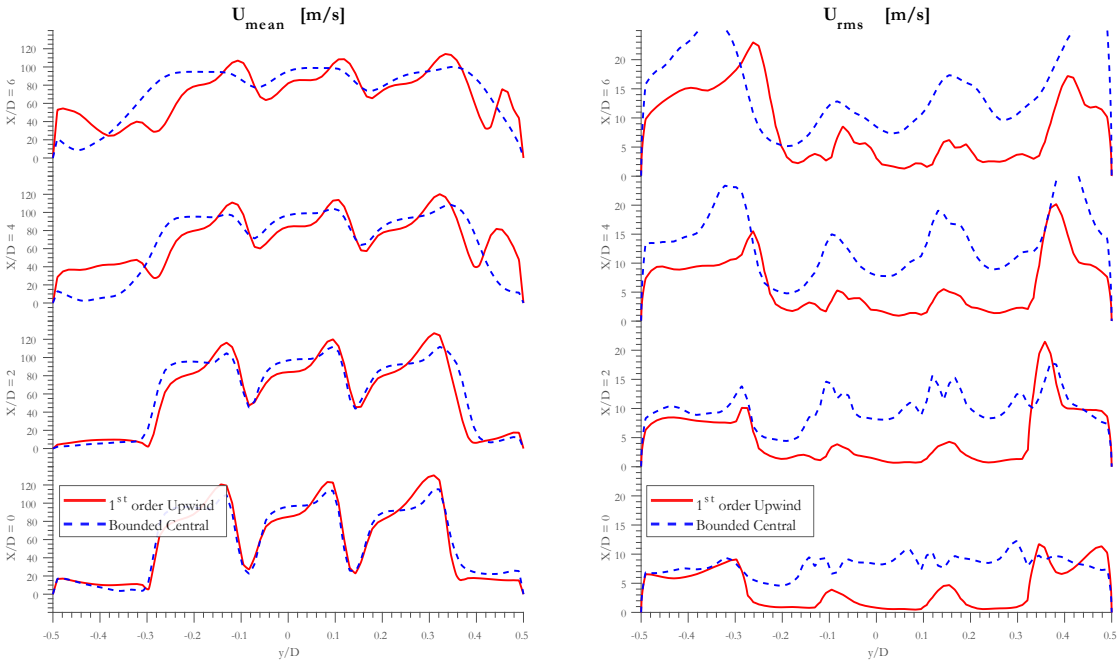

Figure 3.8: The importance of using a second order scheme for the momentum equation. The left hand side of the figure depicts the mean velocity, the right hand side the root mean square of the velocity fluctuations. From bottom to top is the data over a line through the domain in transverse direction, with increasing distance from the jet exit.

Subgrid

A comparison between the behavior of both the One Equation Eddy and the WALE subgrid models is necessary before thermoacoustic results can be discussed. It is important that the modelling procedures do not influence the thermoacoustic behaviour signifcantly. Figure 3.9 depicts the resulting velocity profiles in the same manner as Figure 3.8. The hump in the velocity profile is not visible for the WALE subgrid model. The vortex generators in this case are placed 0.116 mm behind the jet exit, meaning that approximately 12 jet diameters further the effect of the vortex generators is not visible. Whether this is a correct prediction by the WALE subgrid model is not clear. It does seem to be in line with the amount of turbulence generated at the walls, visible in the bottom picture on the right hand side of Figure 3.9. The red line, representing the WALE results, depicts higher values of turbulence than the One Equation Eddy model. This could be a possible reason for the difference in velocity profile. Also, the WALE velocity profile seems to smears out faster and the turbulence tends to decay slightly faster.

In order to demonstrate the effect of different turbulent subgrid models on the flame shape, the progress variable has been tracked over the most centre flame in Figure 3.6. The middle flame resembles the majority of the flames in the S400, as most of the flames will be tucked in between other flames. The tracking is done by drawing a virtual line through the flame in axial and transverse direction. Figure 3.10a is a line in axial direction through the centre of the middle flame, tracking the progress variable over it. Figure 3.10b is a line in transverse

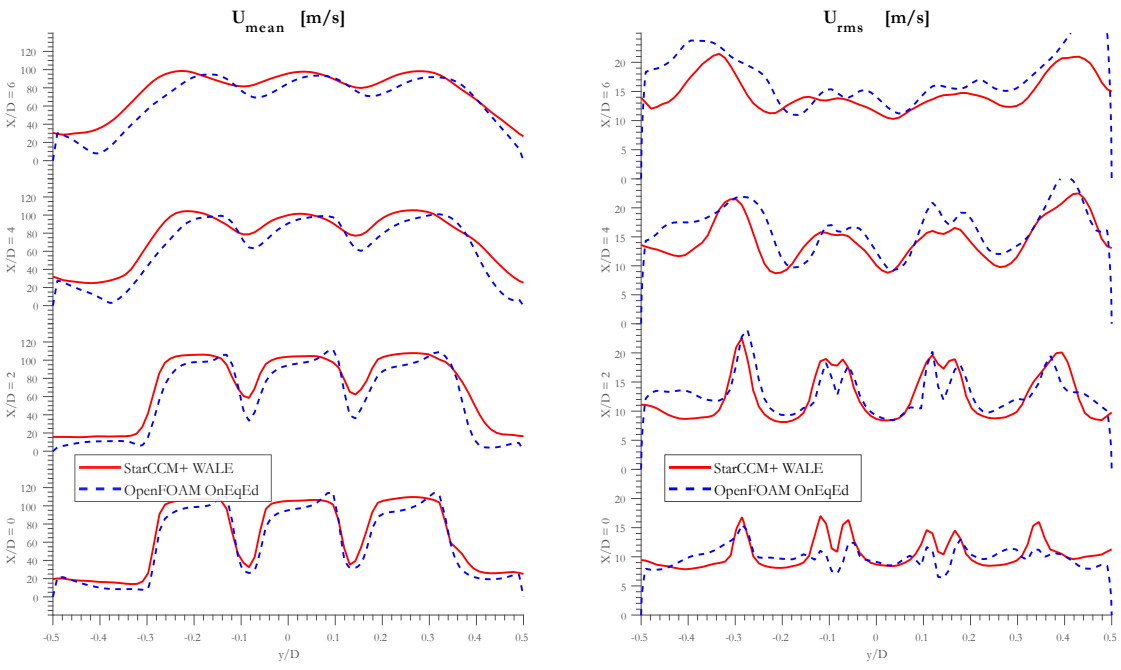

Figure 3.9: Subgrid performance on the velocity field and the turbulence. The left hand side of the figure depicts the mean velocity, the right hand side the root mean square of the velocity fluctuations. From bottom to top is the data over a line through the domain in transverse direction, with increasing distance from the jet exit.

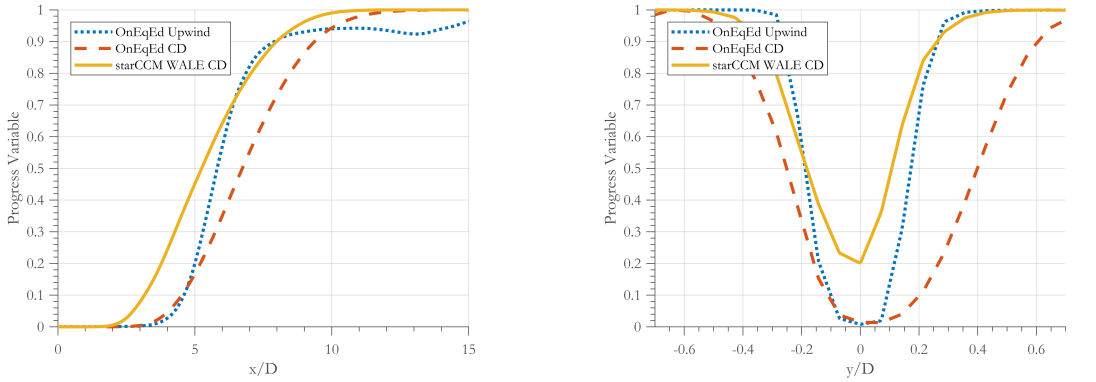

(a) Progress variable in axial direction **(b)** Progress variable in transverse direction

Figure 3.10: The progress variable of the center flame derived in axial and transverse direction

direction of the flame at a distance of $x/D = 2$ of the jet exit. The results from the first order upwind scheme are also added, to visualize the importance of second order schemes over first order.

Figure 3.10 indicates that the difference between first and second order with regard to flame shape is small. Here, analyzing only one flame can provide misleading results. While the shape of middle flame for the first order scheme is not that different from the second order solution, the outer flames are at least twice as long. A more accurate method to compare flame shapes, is to compare the axial centre of total heat release. This way, the spatial structure of all flames is taken into account. The results are shown in Table 3.2.

The StarCCM+ calculation with FGM Kinetic Rate results in a slightly larger axial centre of heat release than the OpenFOAM case with ATF, but the difference is only 6%. In transverse direction of the flame (Figure 3.10b), the StarCCM+ calculation results in a smaller flame than the OpenFOAM calculation. There are two explanations for this behavior. One was that the flames in the OpenFOAM calculation seem to attach to each other at jet exit at some points in time. The other reason is that a very small self-excited transverse acoustic mode was occurring in StarCCM+. Thermoacoustics compress the flame shape and therefor a slightly smaller flame in transverse direction can be expected.

Mesh Dependency Study

The amount of cells per flame influences flame shape [102]. To be sure that the 14 cells per diameter, as advised by Goeb [96], is indeed enough to accurately simulate the flames, a mesh

Table 3.2: The axial centre of heat release per subgrid model, where COHR stands for Centre of Heat Release, OnEqEd for One Equation Eddy and CD for Central Differencing

Axial COHR	OnEqEd, 1^st order	OnEqEd, CD	WALE CD
14 Cells	60.60 mm	43.7 mm	46.6 mm

dependency study is conducted. The investigated amount of cells per flame diameter were 10, 14 and 21 cells and the results can be found in Table 3.3.
The meshes were made with *snappyHexMesh*, an open-source mesh tool, compatible with OpenFOAM. The meshes have been exported to StarCCM+, so that there is no difference in mesh per cell case. The meshes were refined up till 150 mm away from the jet exit. The ducts contained two layers, with an average y^+ value of 60 for the first grid point distance. The grid in the ducts is the same for every mesh, to exclude any effects in that region. As can be seen from Table 3.3, the total amount of cells increases rapidly by adding more cells per flame diameter.

For the 10 and 14 cells per flame diameter, the StarCCM+ calculation results in a slightly larger value for the axial centre of heat release than OpenFOAM does with a model constant of 0.5. Moreover, in OpenFOAM, the amount of cells does not cause any significant changes in axial flame length. The 21 cells per flame diameter does seem to influence the axial flame length of the StarCCM+ compared to the less cells per flame diameter. However, a self-excited oscillation between flames and the plenum, even though there was a sponge at the outlet, caused the flame length to decrease.

Table 3.3: The axial centre of heat release dependent on mesh, flame model and subgrid model

Axial COHR	10 Cells	14 Cells	21 Cells
OpenFOAM	42.6 mm	43.7 mm	43.4 mm
StarCCM+	45.6 mm	46.6 mm	40.7 mm
Total amount of cells	1.3 mil	3.3 mil	7.1 mil

Based on the results shown in Table 3.3 it is decided to proceed with 14 cells per flame diameter. The reduction in total amount of cells compared to the 21 cells per flame diameter is significant, while the flame shape remains almost the same for both cases.

3.2.3 Thermoacoustic Comparison Flame Models

This section covers the thermoacoustic results of the two approaches. Namely the OpenFOAM approach with the ATF in combination with a subgrid wrinkling model and the StarCCM+ approach FGM. All simulations in this section are performed on the 14 cells per flame diameter mesh. The CFL number for all calculations was set to 1, corresponding to a time step of $0.7E-6$ s .

Both approaches are simulated self-excited and pressure bombed. Figure 3.11 depicts the results for the self-excited approach performed in StarCCM+ . Figure 3.12 shows the results for the perturbed StarCCM+ simulation. Figure 3.13 is the result of the self-excited approach in OpenFOAM and Figure 3.14 shows the results of the perturbed OpenFOAM simulation.
Figure 3.11-3.14 are derived by analyzing a pressure probe, which is for all four cases in the same position. The raw signal is depicted in the plot in the top right hand corner. The corresponding spectrogram is shown in the color plot below. The x-axes, depicting the time, on both plots correspond to each other. In the bottom left hand graph, a standard Fast Fourier Transform (FFT) visualizes the active frequencies a bit clearer. No window has been applied to this FFT. In the same graph, the Rayleigh criterion for every frequency is

plotted. The Rayleigh criterion here is derived over a box containing all flames. Therefor the Rayleigh criterion in this situation, can only account for longitudinal fluctuations. The box fully contains the transverse acoustic mode, as a result transverse instabilities are averaged out.
The Rayleigh criterion is normalized to half the value of the maximum of the FFT for visibility. The top left hand picture is the normalized Rayleigh criterion for the highest value of the Rayleigh criterion over frequencies. This plot indicates the phase between heat release and pressure fluctuations. The dotted line is the average, which has a maximum of 0.5 by definition in the current setup.

Interestingly, the StarCCM+ self-excited calculation (Figure 3.11), starts with some oscillations at approximately 650 Hz, 1830 Hz and 6500 Hz, before a mode at 25 kHz becomes the prominent unstable frequency with an amplitude of around 0.15 bar. On the other hand, perturbing this case results in clear unstable modes at 1830 Hz and 6500 Hz, with a limit cycle amplitude for the 6500 Hz of almost 0.6 bar. The 6500 Hz is later identified as the first transverse mode (Figure 4.4), while the 1830 Hz is a higher order longitudinal mode. The difference in results between a self-excited and pressure bombed calculation, shows the downside of not performing a perturbed pressure field calculation. Some highly unstable modes can then be completely missed by simulations.

Clearly, Figure 3.11 and Figure 3.12 show more activity in the higher frequency regime than Figure 3.13 and Figure 3.14. When the pressure bomb is applied in OpenFOAM, the same frequencies are triggered as in the StarCCM+ case, however they do not sustain. Both self-excited and perturbed approach in OpenFOAM end up having the 650 Hz mode as most unstable mode.
The normalized Rayleigh criterion of the StarCCM+ calculation, the heat release fluctuations and the pressure fluctuations for the 1824 Hz are almost perfectly in phase, while for the 650 Hz the phase difference is larger. This explains partly why the limit cycle amplitude for the 1824 Hz is much higher than that of the 650 Hz. Please note in this section that the simulated time is not equal for all cases. When a clear trend was visible, the simulations were stopped. Therefor, the frequency interval for the Rayleigh plots is not the same. Small differences in exact frequencies are expected.

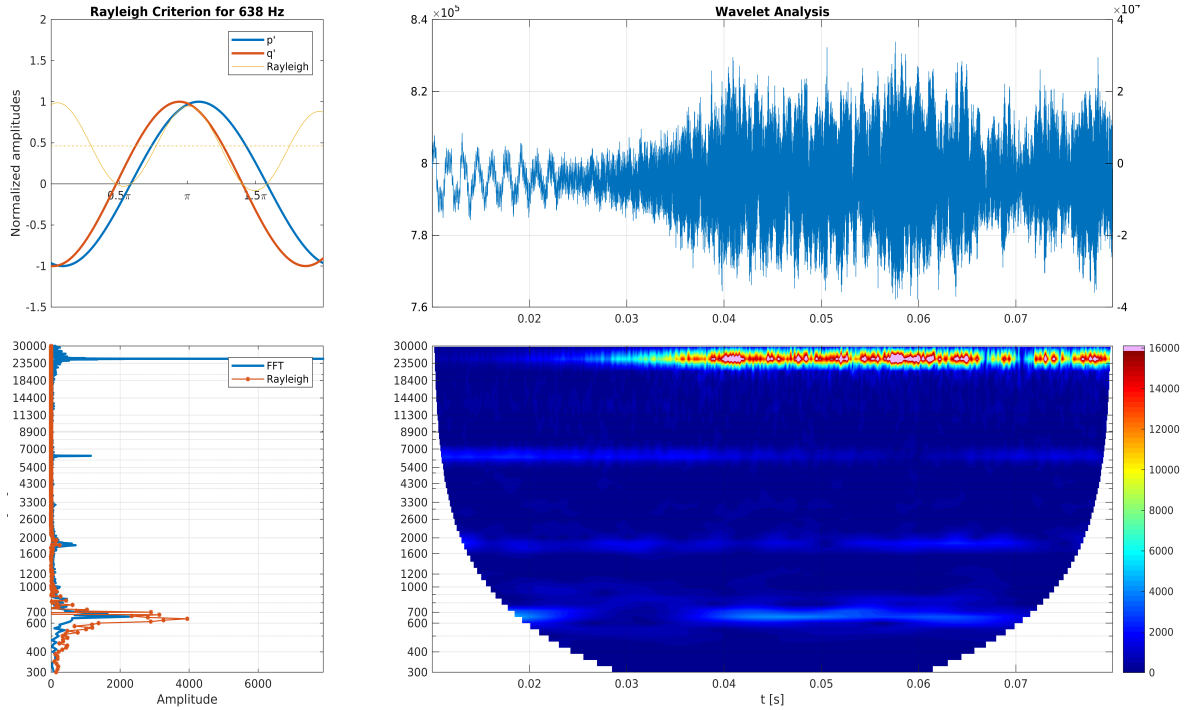

Figure 3.11: Acoustic analysis of the self-excited results of the StarCCM+ case

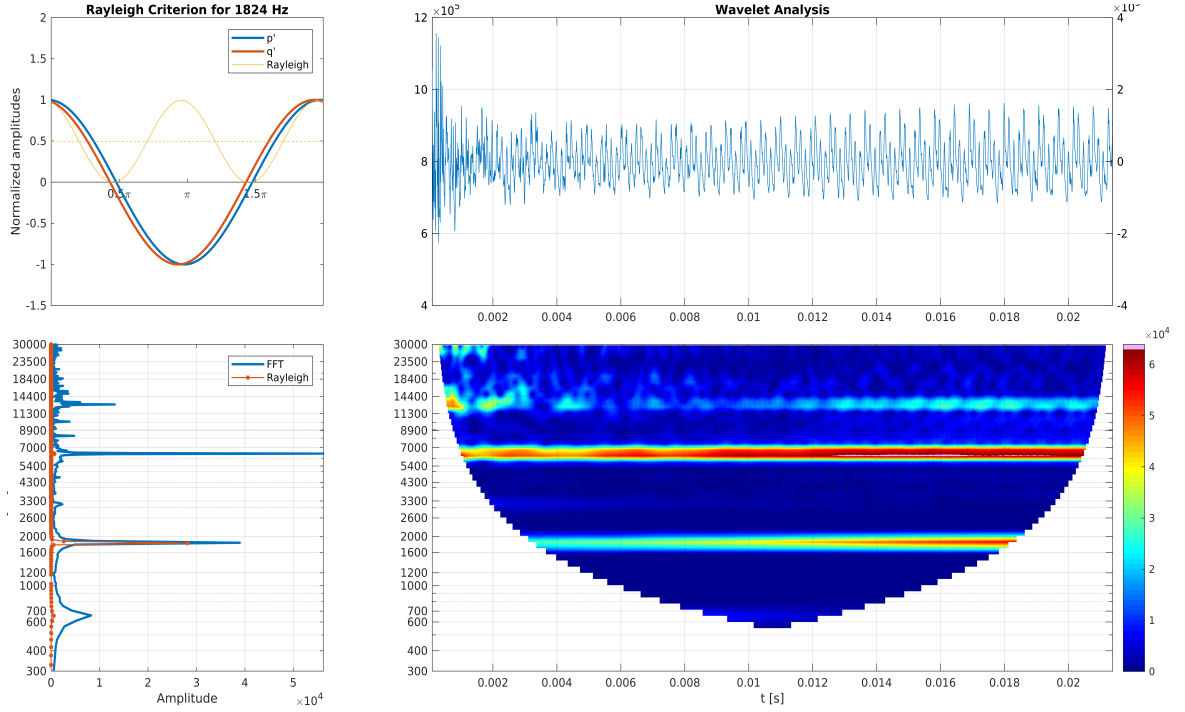

Figure 3.12: Acoustic analysis of the pressure perturbed results of the StarCCM+ case

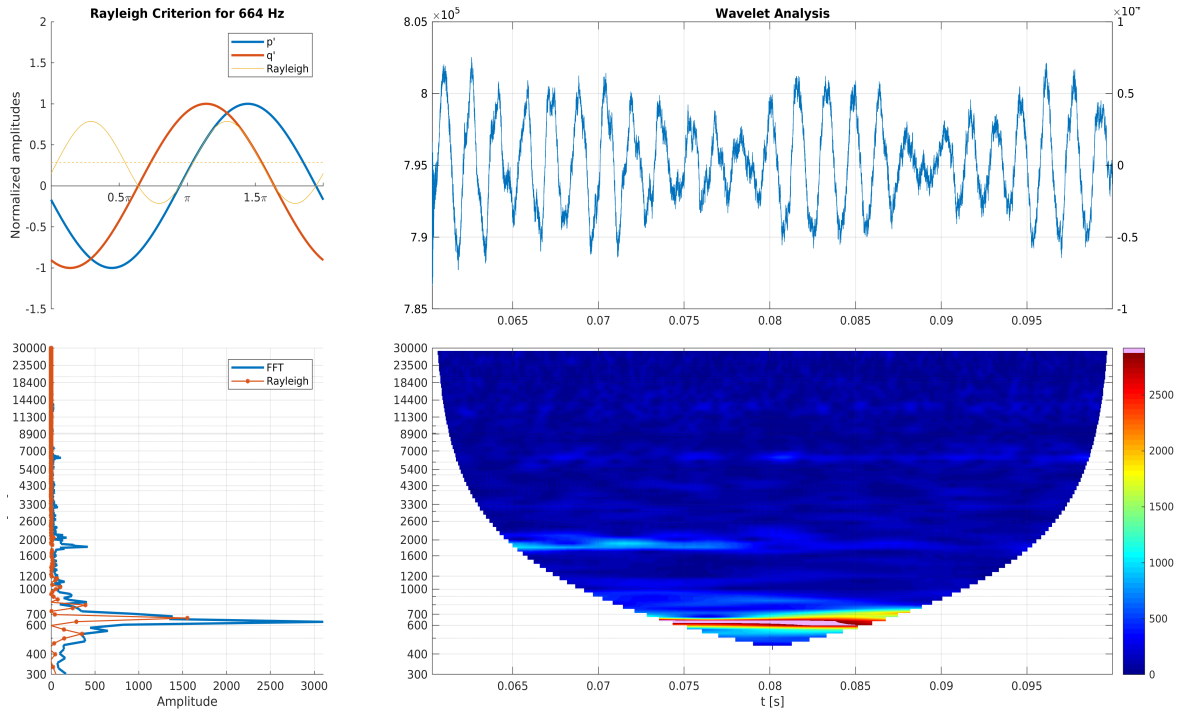

Figure 3.13: Acoustic analysis of the self-excited results of the OpenFOAM case

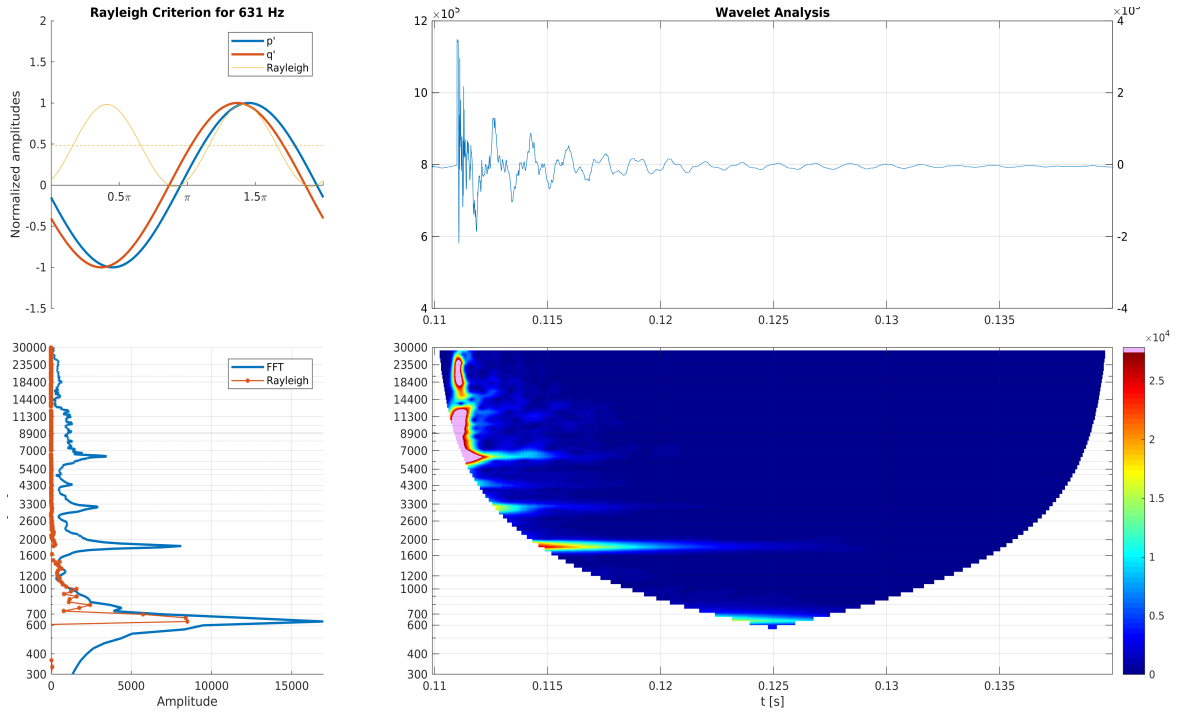

Figure 3.14: Acoustic analysis of the pressure perturbed results of the OpenFOAM case

The self-excited case in StarCCM+ eventually shows an instability occurring at $\sim$ 25 kHz. The corresponding wave length for that frequency is small. A few calculations enables insight in whether these small wave lengths are possible to simulate or whether this oscillation is a numerical artifact.
The speed of sound in the burned region is approximately 800 ms^{-1}. The absolute grid size per cell was 0.7 mm. The wave length at 25 kHz equals to

$$\lambda = \frac{c_0}{f} = \frac{800\ ms^{-1}}{25000\ Hz} = 0.032\ m. \tag{3.15}$$

This means that the number of cells per wave length, which is an important criterion in thermoacoustics [61],

$$n = \frac{\lambda}{\Delta} = \frac{0.032\ m}{0.7e^{-3}\ m} \approx 46, \tag{3.16}$$

where n is the amount of cells and λ the wave length. According to Krediet [61], with an CFL number of 1, this is on the edge of what could accurately be simulated.

Previously, it was stated that the simulations did not solve any mixing and that a perfect mixture is assumed. Up till now, it remains unclear whether HFD is related to convective time lag instabilities [14]. The fact that limit cycles are reached for transverse mode without mixing, means that equivalence ratio fluctuations do not play a role here.

3.3 Conclusion

The goal of this chapter was to derive the optimum settings for simulating transverse oscillations in combustion chamber. It was observed that the settings used in StarCCM+ resulted in more visible high frequency oscillations compared to the settings used in OpenFOAM. On the other hand, the derived amplitudes in StarCCM are large. Normally the oscillations are in the range of approximately $0.5 \sim 2\%$ [105, 106] of the mean pressure. In this calculation the oscillations are almost 10% of the mean pressure.

As there are no experimental results which can confirm either of these settings, there is no saying in which setting is more accurate. Therefore the decision is based on the answer to the question, which setting results in more observed transverse oscillations. The settings used in StarCCM+ is the clear answer here. Hence, all calculations from this point on are conducted in StarCCM+ with its corresponding settings derived in this chapter.

Furthermore, the mesh study with regard to flame shape indicated that the difference between using 14 and 21 cells per flame diameter is small. The amount of cells which can be saved, and thus reduce required computational power and costs, is on the other hand significant, which can be derived from Table 3.2. Before a decision is made on the amount of cells per flame diameter for the full S400 domain, a study into numerical dissipation and dispersion with regard to thermoacoustics in the small domain has to be performed, which is done in the next chapter.

The remaining open questions were whether the settings for the 20 mm and 40 mm jets apply to the 10 mm jets and if a perfect mixture can simulate transverse thermoacoustic instabilities. In Figure 3.7 it is shown that the flames look proportional to the suggested L/D ratio between 4 and 7. On top of that, the flames are not artificially merged together due to a too coarse grid. There is no reason to assume that the old settings do not also apply for the 10 mm jets. Furthermore, it is shown that it is not required to resolve mixing to simulate transverse instabilities.

Chapter 4

Thermoacoustic Results of the Sample Case

In the previous chapter, it was observed in Figure 3.11 and Figure 3.12 that already in the small domain, quite some (transverse) thermoacoustic oscillations occur. Due to the fact that the computational expenses for this smaller domain are much lower than for the full domain of the S400, this smaller domain is used for a more in depth analysis of thermoacoustic behaviour in a combustion chamber. The questions that will be answered in this chapter are:

1. How much influence do numerical dissipation and dispersion have on the predicted thermoacoustic behaviour?

2. Are the acoustic modes predicted by CFD all eigenfrequencies of the domain?

3. What is the influence of the flame shape (or flame length) on thermoacoustics instabilities in the system?

4. Are the heat release centres of the flames oscillating on the same frequency as the acoustic frequencies in the domain? And how does the flame centre movement looks like?

5. Is there a way to predict in the frequency domain which eigenfrequencies of the domain are most likely to become unstable?

As far as possible, the answers to these questions are given in sections 4.1 - 4.5. StarCCM+ and its corresponding settings from section 3.2 are used in this chapter to derive the results. In addition, a new pressure bomb method is introduced in section 4.1, in order to avoid any influence of the chosen bomb location.

4.1 Numerical Dissipation and Dispersion

In this section, numerical dissipation and dispersion are tried to quantify as a function of the CFL number and mesh size. The recommendation from literature is to find an optimum in CFL number and amount of cells per wavelength [102]. The first set of simulations are conducted with a grid size of 10, 14 and 21 cells per flame diameter, while keeping the CFL constant at a value of 1. The second set of simulations varied the CFL number, while keeping the grid size constant (14 cells per flame diameter).

The sponge layer at the outlet has been removed and a perfect mixture was again assumed. All simulations were brought to their limit cycle in a new way, namely by activating a progress variable ignitor during run time in the LES. The ignitor is a volume section which immediately burns everything it can burn and it is placed at the jet exit. Allowing the ignitor to be active for a short time during a LES results in a major impulse to the system and is comparable to the pressure bomb.
The pressure bomb can be tedious and would not always be numerically stable. The ignitor approach was always stable and didn't require any tuning. The results are thereby easier to compare and the limit cycle amplitude should not depend on the excitation. In order to eradicate any influence by the excitation mechanism the ignitor was the preferred approach over the pressure bomb. The FFTs were computed over 20 ms of limit cycle time for all cases. For a frequency of 6500 Hz, this would mean that it will be resolved approximately 130 times. The resulting frequency interval of the FFT, Δf, is 50 Hz for all simulations.

Figure 4.1 depicts the result for a varying CFL, while the same grid has been used. This is the 14 cells per flame diameter mesh, with a 0.7 mm absolute grid size in the flame region. As a result the amount of cells per wave length for a frequency of for example $1.3kHz$ equals 115. In line with Krediet [61], a bit of dispersion can be observed for a CFL of 4, compared to its lower values in Figure 4.1. A CFL number of 2 does not differ in predicted frequency compared to a CFL of 1. Small differences in amplitude can be seen, but the signals in Figure 4.1 indicate that the signal is not always constant. Meaning that the sample time is most likely too short to fully compare amplitudes here.

Figure 4.2 shows the result of the mesh study on thermoacoustics in the sample case. In all simulations here, the CFL was kept constant at a value of 1. The corresponding time steps for the 10, 14 and 21 cells were respectively $1E-6$ s, $0.7E-6$ s and $0.5E-6$ s. It turned out to be difficult to compare meshes with regard to amplitudes. The spatial position of the acoustic mode changed under the influence of the mesh. Therefore again, it is not straightforward to compare amplitudes here.

The verdict in this section, is that it is difficult to fairly compare amplitudes. However, there are indications that a mesh of 14 cells per flame diameter performs equally well as the 21 cells per flame diameter with constant CFL number. At $CFL = 4$, numerical dispersion surfaces for the $6500Hz$ mode. Based on these results, a mesh containing 14 cells per flame diameter and a CFL number of two is assumed accurate enough, while keeping computational expenses to a minimum.

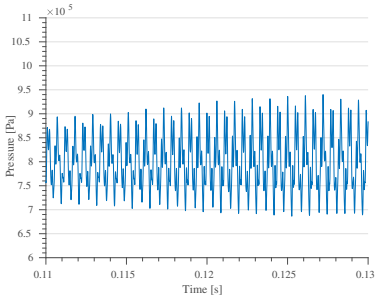

(a) Pressure Signal for CFL = 4

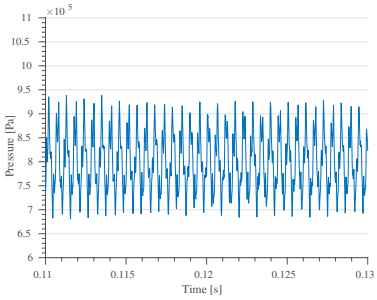

(b) Pressure Signal for CFL = 2

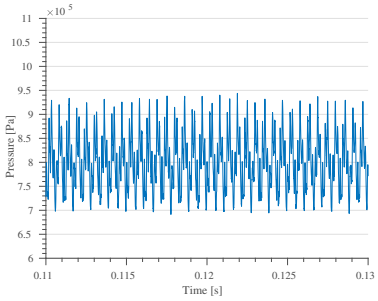

(c) Pressure Signal for CFL =1

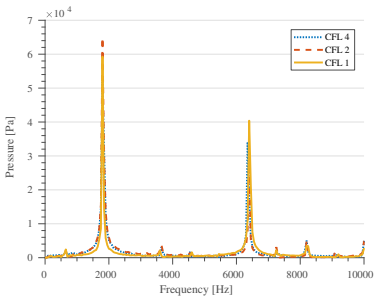

(d) Comparison FFT of CFL numbers

Figure 4.1: The influence of the acoustic CFL number on the accuracy of the simulations. The mesh is constant, the CFL number is varied.

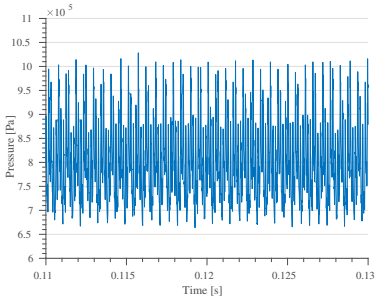

(a) Pressure Signal for 10 Cells

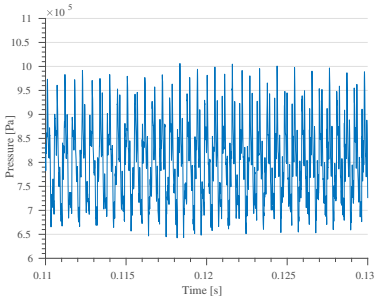

(b) Pressure Signal 14 for Cells

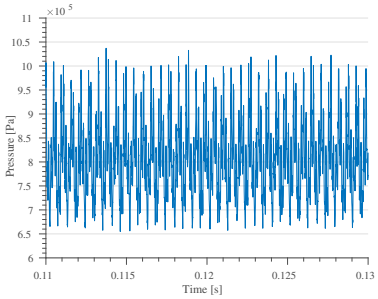

(c) Pressure Signal 21 for Cells

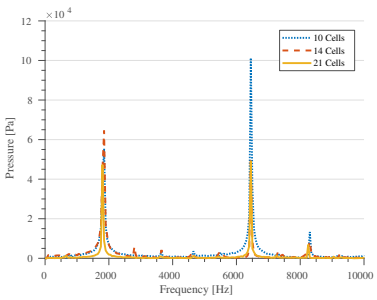

(d) Comparison FFT of mesh size

Figure 4.2: The influence of the grid size on the accuracy of the simulations. The mesh is varied, the CFL number is constant.

4.2 Acoustic Mode Comparison

In this section, a comparison is made between the acoustic modes predicted by CFD and a Helmholtz solver. The idea of this comparison, is to check whether the predicted frequencies and corresponding mode shapes by CFD make physical sense. Furthermore, it is a wish of gas turbine combustion development teams to simulate and make accurate predictions in the frequency domain, as opposed to the time domain of a LES. Directly solving in the frequency domain is computationally much cheaper than solving in the time domain. A match between CFD predicted mode shapes from the time domain with its counterpart in the frequency domain is the first step to validate if such an approach is viable.

The figures in section 4.1 show that the CFD calculations result in high amplitude oscillations at approximately 1800 Hz and 6500 Hz. Smaller amplitudes are found for frequencies of approximately 3600 Hz, 8205 Hz and 10005 Hz. Out of the boundaries of Figure 4.1 and Figure 4.2 are two peaks, namely 12820 Hz and 13700 Hz. Both are visible in the spectogram in Figure 3.12.

In order to derive the eigenfrequencies of the system by COMSOL, the geometry and temperature field were imported from CFD. A different mesh had to be made because the mesh from *snappyHexMesh* was not compatible. It was found during the process that differences in mesh result in small differences in the predicted frequencies. This deviation was in the order of 10 Hz. There was no forcing applied to derive the mode shapes in the frequency domain. In StarCCM+, the corresponding mode shapes are visualized by means of a Discrete Fourier Transform (DFT) of the pressure on the surface of the domain, derived with Hahn as a window function. The sampling time was 30 ms. Figure 4.3 till Figure 4.6 show the mode shapes predicted by CFD on the left hand side. On the right hand side, the corresponding eigenfrequencies of the domain, predicted by the Helmholtz solver from COMSOL Multiphysics are visualized.

The resemblance of the first two acoustic modes, shown in Figure 4.3 and Figure 4.4 for their CFD and Helmholtz solver counterpart is striking. The predicted value for the frequencies slightly differ, namely 1800 Hz versus 1875 Hz and 6550 Hz versus 6575 Hz by respectively the CFD and the eigenfrequency solver. The differences in absolute frequencies can be explained by the fact that the mesh was not the same. Moreover, the temperature field was extracted from a RANS, whilst in a LES under the influence of thermoacoustics, the flame lengths tend to be almost 40 % shorter. Note that the legend has been removed for visibility. It was not possible to normalize the output values. Therefor the min and max values, which determine the orientation of the colors, have been set manually in order to make the comparison realistic.

The acoustic mode of approximately 1800 Hz in Figure 4.3 is identified as the third longitudinal mode and the mode in Figure 4.4 corresponds to the first transverse mode. The first transverse wave is a standing wave in this setup. Interestingly in Figure 4.4 the acoustic mode is also very active in the ducts. Meaning that the ducts acoustically couple with the combustion chamber. This effect is explained in more detail in section 4.4.

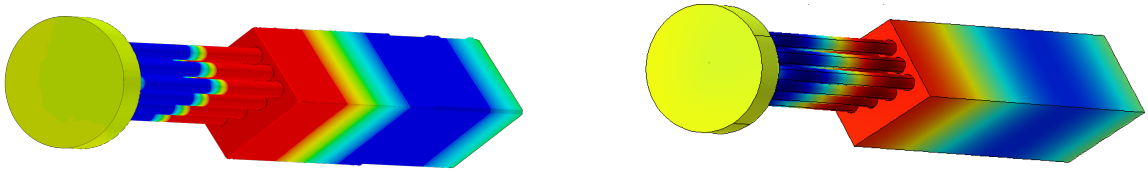

(a) CFD 1800 Hz **(b)** COMSOL 1875Hz

Figure 4.3: Mode shape comparison between what CFD predicts and the nearest in COMSOL derived eigenfrequency of the system (3L).

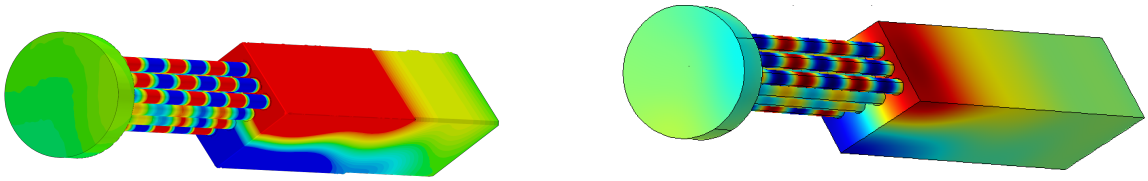

(a) CFD 6500 Hz **(b)** COMSOL 6590Hz

Figure 4.4: Mode shape comparison between what CFD predicts and the nearest in COMSOL derived eigenfrequency of the system (1T).

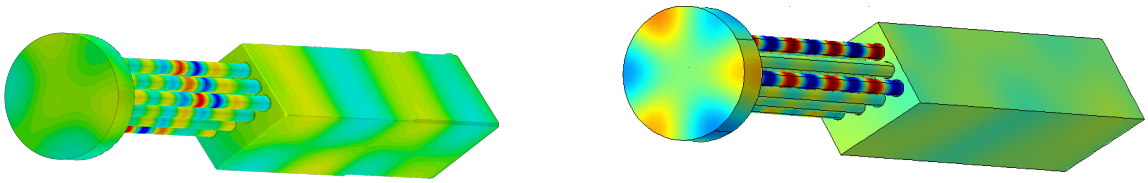

(a) CFD 8250 Hz **(b)** COMSOL 8260 Hz

Figure 4.5: Mode shape comparison between what CFD predicts and the nearest in COMSOL derived eigenfrequency of the system (1T2L).

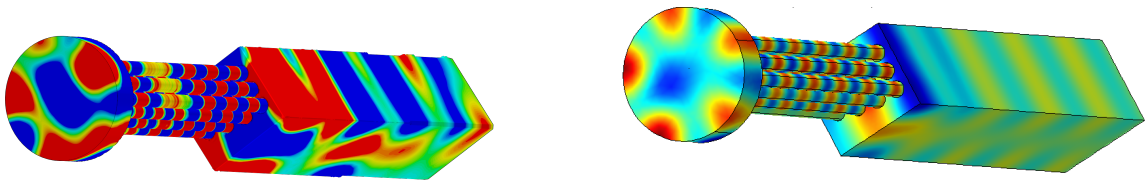

(a) CFD 12900 Hz **(b)** COMSOL 12820 Hz

Figure 4.6: Mode shape comparison between what CFD predicts and the nearest in COMSOL derived eigenfrequency of the system (2T).

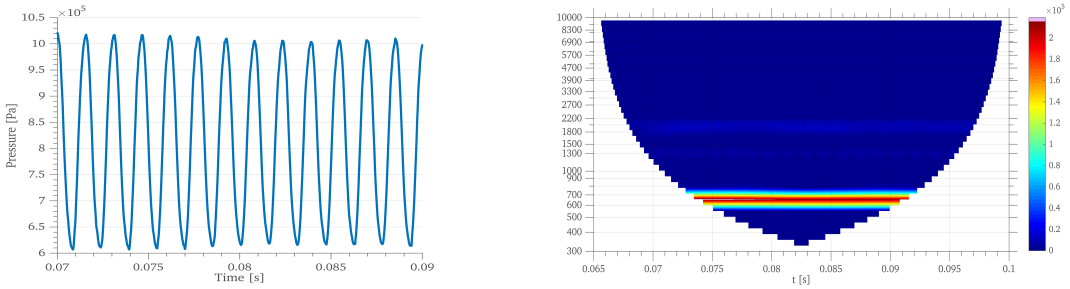

(a) Pressure signal **(b)** Pressure spectrogram

Figure 4.7: The signal and its corresponding frequency spectrum for an elongated flame.

The peak predicted at 8250 Hz has a much lower amplitude than the 1800 Hz and 6550 Hz and finding its matching frequency with the eigenfrequency solver was difficult. The eigenfrequency depicted on the right hand side of Figure 4.5 is the closest guess. The higher the frequency, the more difficult it is to manually determine which are matching mode shapes. Again, the mode shape picked in Figure 4.6 is a best guess. The mode shape from CFD seems to be deformed when compared to its COMSOL counterpart. It can not be ruled out that diffusion at these small wave lengths results in the deformation. Especially in the plenum, which does not contain any mesh refinements. The question that arises now, is whether it is possible to derive an equation in the frequency domain that could automatically select the corresponding mode shapes. Section 4.5 elaborates on this subject.

4.3 Flame Shape

This section covers the influence of the flame length on the thermoacoustic behaviour in the sample case. In order to exclusively determine the effect of flame length, every parameter remains constant, except the chemical burn rate coefficient, which determines how quick a flame burns. A lower value for the burn rate, results in a longer flame, without changing the geometry or the turbulence of the system.

Figure 4.7 displays the thermoacoustic results of the described setup. Again, the 14 cells per flame diameter mesh is used in combination with a CFL number of 1 and a perfect mixture is assumed. The measuring position is the same as the one in the previous two sections and the excitation mechanism is the ignitor approach.

Changing the burn rate of the flame has a significant impact in the thermoacoustic behaviour. There is no longer any HFD visible in the spectrum, see Figure 4.7b. Only one active mode remains, the 650 Hz, which is the first longitudinal mode in the system. The corresponding limit cycle amplitude for this single frequency is approximately 2 *bar*. In fact, due to the large acoustics in the system, the resulting mean flame length is not larger than with the original burn rate. The influence of the thermoacoustic instability on the flames is shown in Figure 4.8. The air fuel mixture reaches further into the combustion chamber (t_1), due to the lower burning rate. Then the cold mixture breaks up into vortices (t_2). These vortices recirculate (t_3), causing the mixture to burn upstream (t_4). The process then repeats itself. This phenomena is the same as the flame-vortex interaction described in section 2.4. The

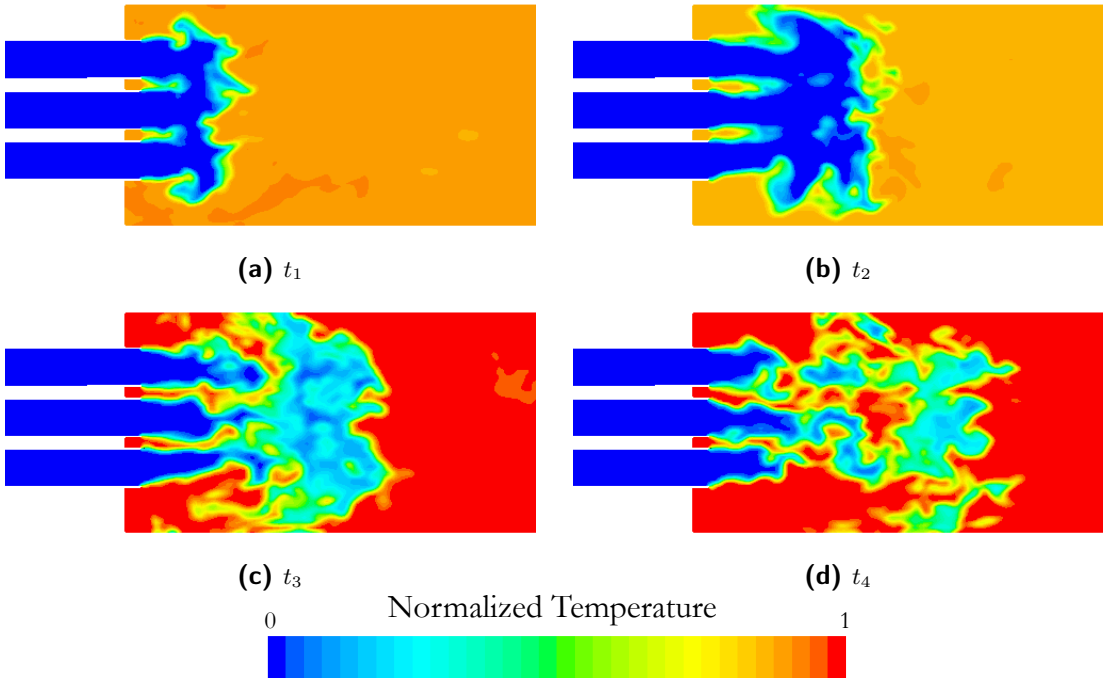

Figure 4.8: Vortex Shedding caused by a lower burn rate

effect of the convective time lag theorem is clearly visible through these simulations.

A few conclusions can be derived from the results in this section. Namely:

1. In simulations with an initial perfect mixture condition IFD instabilities can still occur.
2. Large longitudinal waves through a system leave no room for transverse thermoacoustic instabilities to occur.
3. Burn rate (Flame shape) has a significant impact on the frequency of the instability in the system.

The results derived in this subsection are interesting and show that eliminating the longitudinal instabilities may be necessary in order to observe transverse instabilities in CFD simulations. The flame-vortex phenomena is interesting and it should be investigated further what the exact causes are and why this occurs on the 650 Hz eigenmode and not the 1850 Hz. However that is not in the scope of this thesis.

4.4 Flame Displacement

In subsection 2.4.2, a hypothesis to explain the root cause of HFD is that the maximum and minimum heat release position of the flames oscillate under the influence of a transverse acoustic field. The heat release fluctuation couples with the acoustic mode and they amplify each other [14]. It is investigated on the sample case, whether this mechanism can be reproduced. This is done by tracking the spatial movement of the heat release centres of the flames. The same settings as in the previous sections have been used and the corresponding pressure field was already shown in Figure 3.12.

The flame centres movement is tracked by placing a virtual cylinder in front of the jet exit. A passive scalar is inserted in the ducts to distinguish the flames. A conditional heat release integration is made over the volume of the cylinder. More detailed information on this can be found in the Appendix. The heat release centre is then tracked by

$$\vec{x}_{q_{centre}} = \frac{\int_V \vec{x} \cdot q dV}{\int_V q dV}. \tag{4.1}$$

Over the same cylinder, the average pressure is calculated, which is later used for indicating the Rayleigh Criterion per flame. The spatial heat release centre transverse motion of all nine flames is decomposed into the frequency domain. From here on, the heat release spatial motion of a flame is also called flame motion. The corresponding spectograms of the transverse oscillation of the heat release centre of two flames are shown in Figure 4.9. The left spectogram represents a flame on the outskirts of the domain and the right spectogram the centre flame. Both spectograms show, that the frequencies of the oscillation of the heat release centre of the flames aligns with that of the acoustic frequencies, depicted in Figure 3.12. It can also be observed in the same spectograms, that the flames move on the 13000 Hz acoustic mode. The amplitudes in the lower frequency range are most likely either noise or caused by turbulence fluctuations. The spectrum on the left visualizes that the outer flames actually move in transverse direction on the 1800 Hz, which is unexpected. The 1800 Hz is a pure longitudinal motion (Figure 4.3), the flames should displace only in axial direction.

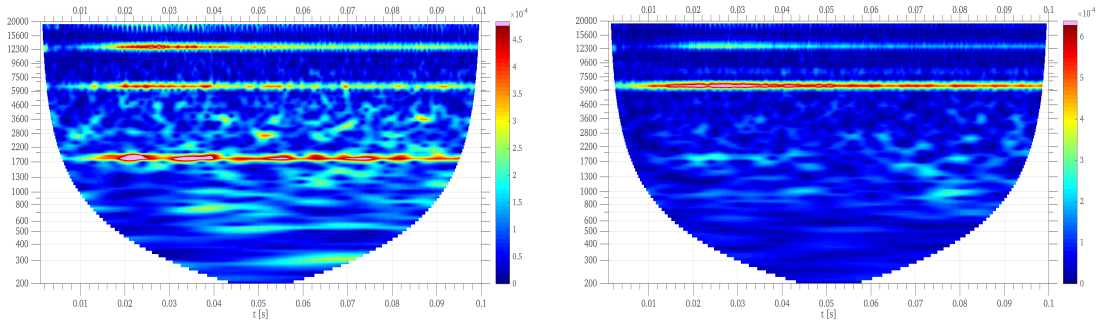

(a) Outer flame **(b)** Centre flame

Figure 4.9: Spectograms of the transverse heat release centre oscillation in the frequency domain of two flames in the small domain. A red color indicates that the heat release oscillates on the corresponding frequency shown on the left axis.

A closer look into the motion of all the flames per interesting frequency is provided by Figure 4.10, Figure 4.11 and Figure 4.12. In these three figures, the figures on the left hand side visualize the filtered spatial flame motion per frequency for all flames. The arrow in the figure indicates the starting point and the moving direction. The colors of the rings represents higher and lower pressure, red for higher pressure and blue for lower pressure. The thickness of the rings visualizes the heat release, where a thicker ring is equal to a high value of heat release and a smaller ring equals low values of heat release. Together the colors and thickness of the rings are a visualization of the Rayleigh criterion.
The pictures on the right in Figure 4.10, Figure 4.11 and Figure 4.12 depict the phase angle of the axial movement of the heat release centres with respect to the centre flame. The figure is a 2D front view of the jet exit.

Figure 4.10a, showing the flame behaviour for a frequency of $1800Hz$ indicates that the outer flames do indeed displace in transverse direction, even though this displacement is much smaller than its axial component. All flames tend to move inwards. This is most likely due to the fact that the flames attract each other. Figure 4.10b indicates that the axial flame movement of all flames is not in phase. A phase difference of approximately 80 degrees between the flames on the left side (y values lower than zero) and the flames on the right side (y values higher than zero) can be observed. It remains unclear why the flames on this frequency do not move in phase in axial direction. The question arises whether a non-linear coupling exists between the $1800Hz$ and the higher order active frequencies in the system.

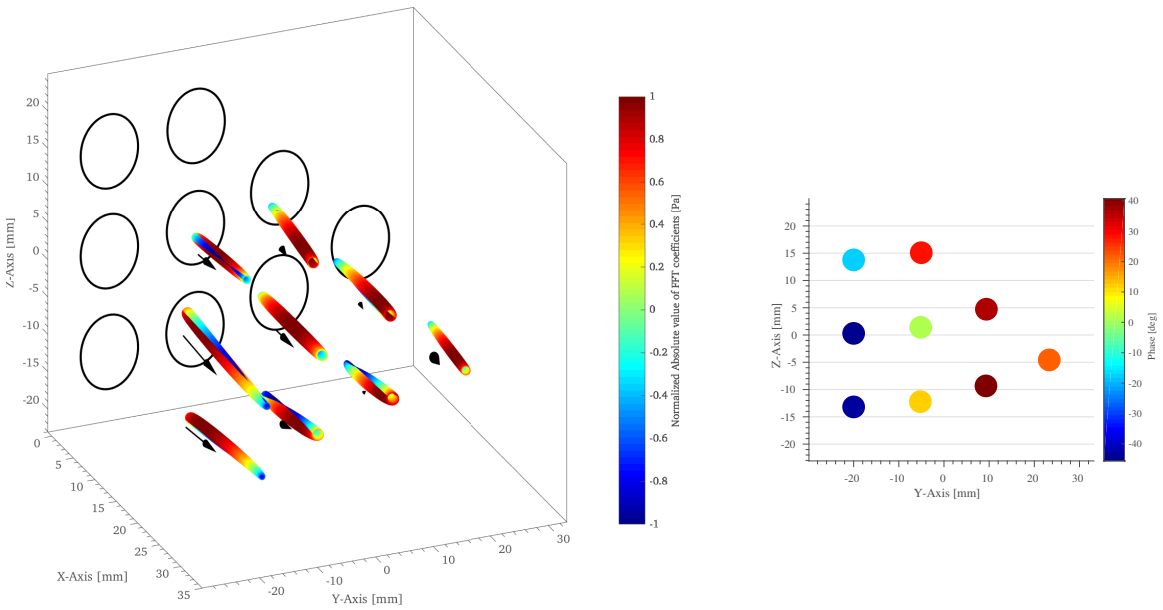

(a) Flame motion, amplified twice **(b)** Phase (deg) axial flame motion

Figure 4.10: Visualization of the flame motion on a frequency of 1800Hz

Figure 4.11a and Figure 4.11b visualize the spatial heat release centre displacement and phase of the axial flame movement for the 6500 Hz mode in the domain. The corresponding pressure distribution can be found in Figure 4.4. The flame spatial motion can be interpreted as follows. Following the pressure distribution, high and low pressure occur in the direction of the y-axis. The flames in the high pressure amplitude regions displace mostly in axial direction, with a small transverse component. This is due to the fact that a high pressure in the flame region results in less fresh air fuel mixture that enters the combustion chamber, whereas a low pressure allows more air fuel mixture to enter the combustion chamber. Thus the outer flames displace mostly in longitudinal direction, following the sign of the pressure.

The flames in the centre, around $y = 0$ are heavily influenced by the acoustic velocity fluctuations induced by pressure distribution of the acoustic mode. Where the outer flames show axial movement, the flames in the centre mostly move in transverse direction. This makes sense, the velocity anti-node lies exactly in the centre region for the $6450Hz$ mode.
The phase plot of the axial movement of the flames for the $6450Hz$ mode supports the hypothesis that the flames also displace in longitudinal direction for a transverse instability according to the switch of pressure sign. The flames on the right side of the domain, for $y > 0$ have a phase difference for the axial movement of approximately 180 degrees with regard to the flames on the left ($y < 0$).

The flame motion on a frequency of $12820Hz$, with its pressure distribution shown in Figure 4.6, is demonstrated in Figure 4.12. The mode was earlier identified as the second transverse mode. Meaning that two velocity anti-nodes are now situated over the y-axis. The velocity anti-nodes are in between the rows (in z-direction) of jets. As seen before, the flames in a velocity anti-node tend to oscillate in transverse direction. The phase plot aligns with the pressure distribution, the centre flames are all in phase now, while the outer flames lag 180 degrees behind.

The motion of the flames at their limit cycle behaviour is important knowledge. Combustion chamber designers can think of ways to deny the center flames to drive the transverse modes. For example, a solution in this case could be to set up a wall in x-direction through the combustion chamber, dividing the flames into two parts. Or one could elongate the outer jets in axial direction, while the inner jets remain at their current length. The middle flames can then no longer drive the first transverse mode. Note that higher order modes most likely will find a way to sustain. The wall through the center for example will interfere in the velocity anti-node of the first transverse mode, but the wave length of the second transverse mode can then fit in the divided flame zones.

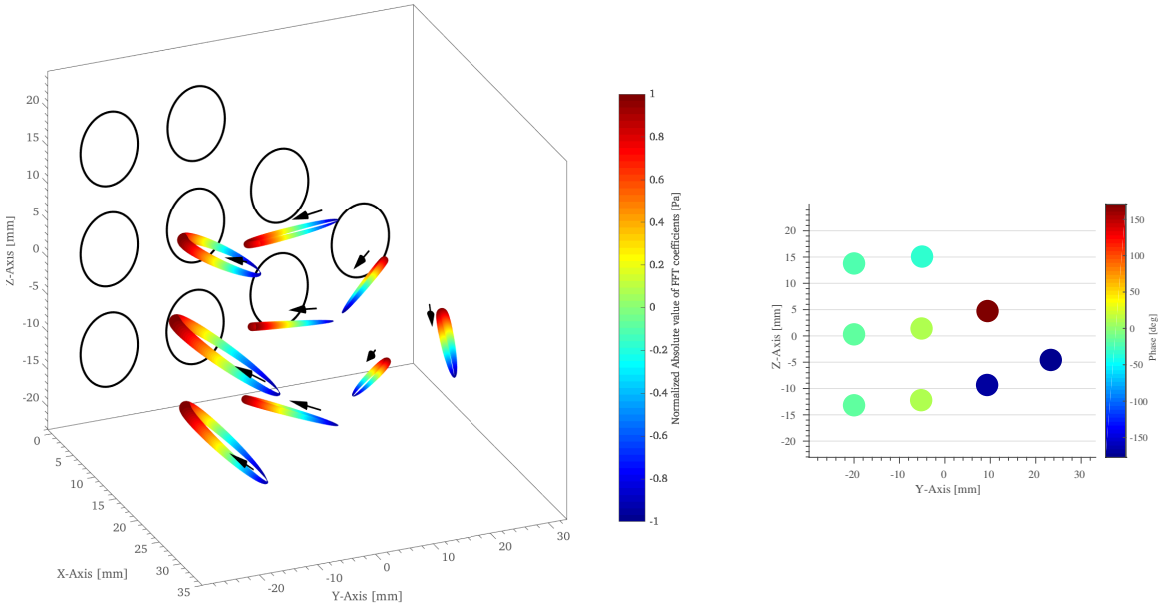

(a) Flame motion, amplified five times **(b)** Phase (deg) axial flame motion

Figure 4.11: Visualization of the flame motion on a frequency of 6450Hz

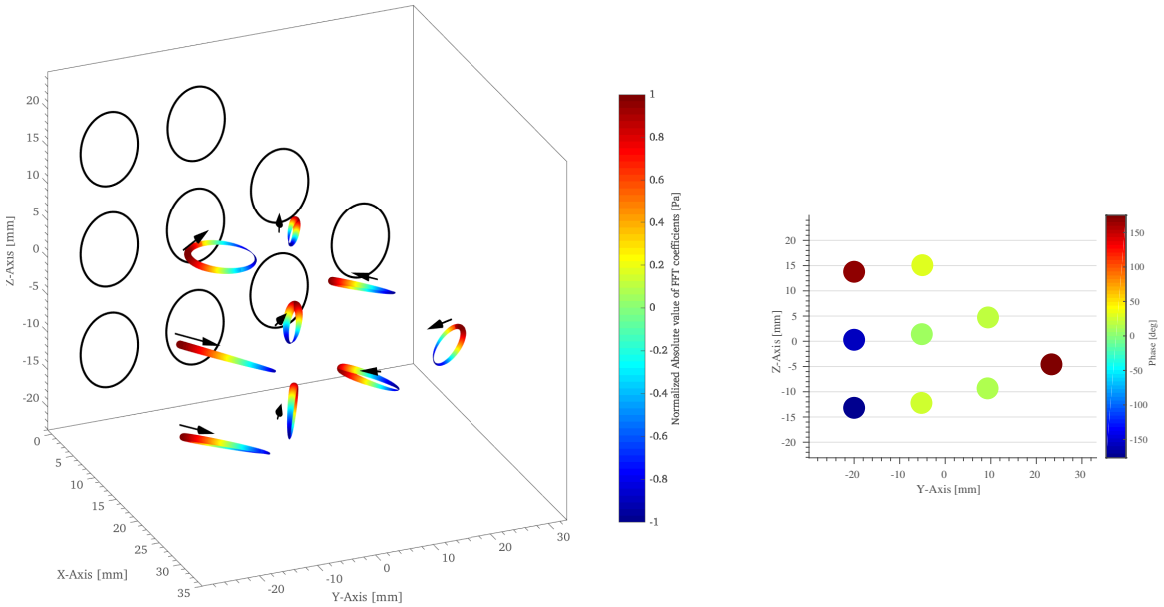

(a) Flame motion, amplified ten times **(b)** Phase (deg) axial flame motion

Figure 4.12: Visualization of the flame motion on a frequency of 12900Hz

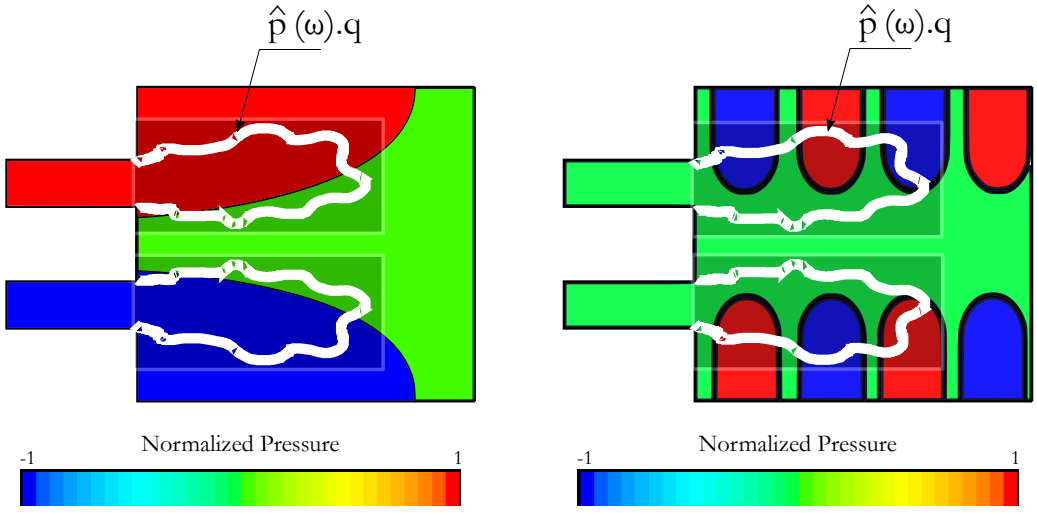

(a) PMR for the 1T **(b)** PMR for a higher order mode

Figure 4.13: Overview of the Poor Man's Rayleigh criterion on a 2D cut. White denotes the heat release, the colors represent the pressure field and the transparent boxes the virtual cylinders.

4.5 Poor Mans Rayleigh Criterion

A Helmholtz solver produces hundreds of eigenmodes for a simple domain, such as the sample case in this thesis. A question that arose in section 4.2, was if it would be possible to automatically find corresponding mode shapes with an eigenfrequency solver to those predicted by CFD. This question is here rephrased to: is it possible to predict in the frequency domain which eigenfrequencies are most likely to become unstable in a combustion chamber? It was already shown that HFD can be simulated without resolving mixing. Secondly, the predicted mode shapes in CFD more or less always match a eigenfrequency predicted by a Helmholtz solver. Furthermore, the coupling of the heat release oscillation and the acoustic modes has been proven.
As a consequence of this coupling, it seems that the flames must anchor in either a pressure or velocity anti-node of the eigenmode of the system in order to become unstable. With all these relations in mind, a method, known as the Poor Man's Rayleigh (PMR) criterion, is tried out on the sample case. In order to derive the PMR criterion, the temperature field and the heat release field of a RANS of the sample case have been imported in COMSOL Multiphysics. The eigenfrequencies of the system were again derived with the ACPR module of COMSOL. The output of the ACPR module is the complex pressure, $\hat{p}$, per eigenfrequency. To account for the fact that the flames must overlap with the anti-nodes of the eigenfrequency of the system, the heat release is multiplied by the derived absolute value of $\hat{p}$.

Another assumption here, is that a flame is compact and does not respond to wave lengths smaller than the flame itself, see for example Figure 4.13b, where the wave in axial direction is smaller than the flame in axial direction. In Figure 4.13a, the wave in transverse direction is not smaller than the flame in transverse direction. This assumption is a source for discussion, however it improved the results for this setup. In order to take this assumption into account,

virtual cylinders were created at each flame position. The heat release is multiplied with $\hat{p}$ and integrated over each cylinder. After the integration the absolute value is taken and summed over all cylinders. If the compact flame assumption would not have been used, the cylinder approach is not required. Integrating the heat release with the absolute value of $\hat{p}$ would be sufficient in that scenario. The last step is to divide the formulation by the integrated heat release, to end up with a general formulation. The corresponding formula is

$$PMR = \sum_{n=1}^{9} \left(\frac{\left| \int_V \hat{p}(\omega) \cdot q \; dV_n \right|}{\int_V q \; dV_{domain}} \right), \tag{4.2}$$

where q denotes the mean heat release derived from CFD. The result is plotted in Figure 4.14a. The blue line is the FFT of a pressure probe in the 21 cells per flame diameter case with an acoustic CFL number of 1. The coloured circles are PMR values for each frequency derived with COMSOL. The red circles represent the longitudinal modes without any transverse components. The green circles are eigenmodes with a transverse component. The circles with a filled yellow color are matching mode shapes between CFD and the Helmholtz solver.
Separating between the pure longitudinal modes and the modes with a transverse component is important, as the PMR criterion is expected to show incorrect results for the longitudinal modes. Convective time lag influences can not be sorted out by this formulation, while these can heavily influence the results for the longitudinal modes. This effect was shown for example in section 4.3.

In order to ensure visibility in Figure 4.14 and to keep things simple, only the matching mode shapes for the three highest amplitudes of the FFT were colored in. It can be seen that the PMR has some ability to predict the interesting eigenfrequencies. The highest peaks from the PMR match that of the most active acoustic modes predicted by CFD. A closer look at for

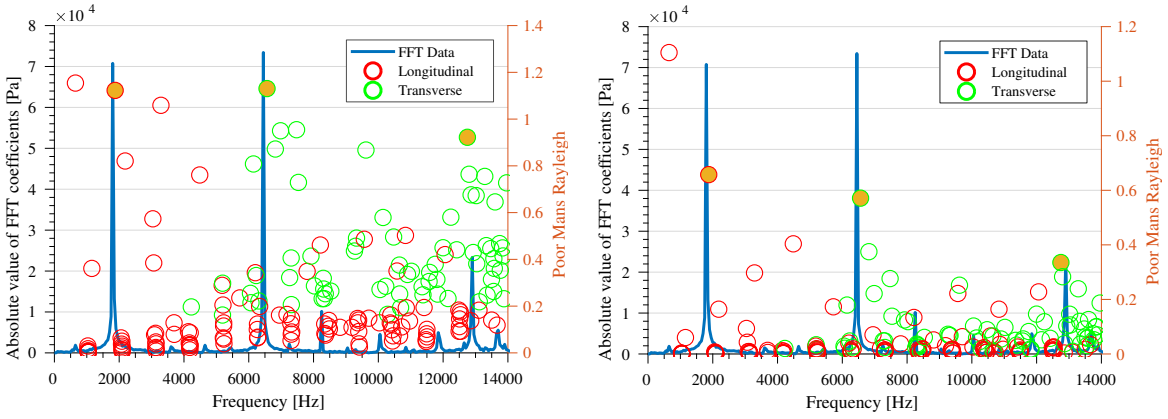

(a) Poor Man's Rayleigh criterion **(b)** Normalized Poor Man's Rayleigh criterion

Figure 4.14: The result of the Poor Man's Rayleigh criterion on the small domain. The red circles are pure longitudinal modes found by the Helmholtz solver, the green circles denote the modes which contain a transverse component in their acoustic mode. The circles filled with a yellow color are matching mode shapes between CFD and the Helmholtz solver.

example the $6500Hz$ region, shows that a heap of eigenmodes has a high PMR value there. Interestingly, only the $6500Hz$ is active in the CFD, all the others in that region are not observed in CFD. A possible explanation could be that all these eigenfrequencies belong to the same family, meaning that they are all first order transverse modes with either a different orientation or a different longitudinal component. The CFD then becomes unstable for the mode with the highest PMR value of the family of modes.

In the current PMR formulation, a lot of eigenfrequencies have an above average amplitude. For example the PMR value of the $9600Hz$ is quite high, while there is no corresponding unstable frequency found in the CFD calculation.
In the current formulation, it does not matter whether the $\hat{p}$ of a eigenfrequency has its maximum value in the flame zone or somewhere else. In other words, the maximum anti-node of the eigenmode does not necessarily lie in the flame zone. Whether this is a problem is not proven. However, a modification to Equation 4.2 can easily take this into account. The derived $\hat{p}$ is normalized by dividing it by its maximum value in the domain

$$PMR_{norm} = \sum_{n=1}^{9} \left(\frac{\left| \int_V \hat{p}(\omega) \cdot q \; dV_n \right|}{max(\hat{p}(\omega)) \cdot \int_V q \; dV_{domain}} \right). \tag{4.3}$$

The results of the normalized PMR can be found in Figure 4.14b. It seems that a few more eigenfrequencies are filtered out by the maximum anti-node assumption. Especially the difference in absolute value of the PMR value between the matching modes and the modes in the same family has increased. It is questionable whether this assumption is physical. For further research it would be interesting to take the same small domain as presented in this thesis and modify it by using resonators or geometry changes until a different mode in the family of the first order transverse modes has a higher PMR value. Then, run a CFD simulation and observe whether the newly predicted most unstable frequency in the family becomes the dominant unstable frequency.

An important conclusion which can be derived from this section, is that the behaviour and origin of transverse instabilities might not be as complex as expected. As presented here, it seems that high values of PMR correspond to the unstable frequencies predicted by the CFD calculations. What this data also indicates, is that actively damping out a certain frequency does not necessarily cure a system of thermoacoustic oscillations. A different unstable frequency could surface, probably with a somewhat lower amplitude. Taking into account the results from section 4.3, large oscillations of one frequency result in that other frequencies might not find 'room' to be unstable. Curing the system of this $650Hz$ mode, would most likely enable other modes such as the first transverse to become unstable.

4.6 Conclusion

The aim of this chapter was to gain more insight in HFD. The origin of the transverse thermoacoustic oscillations in a combustion chamber has not been found, but this is also out of the scope of this thesis. What has been derived, is what occurs during the limit cycle of transverse oscillations. Based on that, mitigation strategies can be refined. The questions posed in the introduction of this chapter have all been answered. Below is a short summary.

1. Numerical dissipation and dispersion play a marginal role in the chosen grid and timesteps. The 14 cells per flame diameter in combination with $CFL = 2$ performed equally to 21 cells per flame diameter with a $CFL = 1$. Too large CFL numbers result in numerical dispersion.
2. Practically all acoustic modes derived from CFD align with the eigenmodes of the system predicted by COMSOL. Some acoustic modes predicted by CFD were slightly deformed compared to their COMSOL counterpart.
3. It has been observed that a slower burn rate causes a lower order longitudinal mode to become active. The amplitude of this oscillation was so large, that other modes were no longer active in the domain.
4. The heat release centres of the flames couple to the acoustic modes in the domain. Interesting data has been acquired for the transverse modes. Namely that the flames in the pressure anti-nodes oscillate in longitudinal direction due to the high and low pressure they endure. The centre flames move in transverse direction because they anchor in a velocity anti-node.
5. The so called Poor Mans Rayleigh criterion has been introduced as a possible mechanism to weight all the eigenmodes from an eigenfrequency solver. It derives a value by calculating the overlap between the pressure distribution of an eigenfrequency with the heat release from CFD. The results were so promising, that it may be possible to predict which eigenmodes are most likely to become unstable in a combustion chamber.

The answers to question four and five combined can provide information on how to avoid transverse oscillations in a combustion chamber. It seems that the geometry of a system should be altered in such a way that the acoustic eigenmode does no longer overlap with the heat release. The PMR criterion can be used to optimize the geometry. The next chapter discusses such a geometry modification, namely baffles.

Chapter 5

Numerical Results of the S400

This chapter is devoted to the results of the simulations conducted on the S400 burner with regard to thermoacoustic instabilities. In particular, the effect of baffles on the thermoacoustic behaviour of the system is investigated here. Consequently, other parameters such as thermodynamic efficiency or pressure drop in the jets are not of interest.

High pressure tests have already been conducted on the S400, with and without baffles implemented. Therefore, both a domain with and without baffles are simulated. The numerical results are compared against the experimental results in this chapter.

In the high pressure tests, the desired operating point could not be reached due to an instability at a frequency of 1180 Hz. Later, this mode is identified as a combination of the first transverse and the first longitudinal mode (1T1L). The simulated case of the S400 without baffles is therefore at a virtual optimum operating point. Introducing baffles in the experiments enabled the operators to reach the optimum operating point. This operating point is the one simulated for both the S400 with and without baffles. The aim of these simulations is to reproduce the acoustic damping by baffles as seen in the experiments. It is expected that introducing baffles in the S400 will lower the frequency on which the 1T1L operates [91, 94].

All the knowledge about HFD which was derived in section 3.2 has been taken into account and used in this chapter. The outlay of this chapter is as follows

1. Domain, Mesh and Settings
2. Thermoacoustic results
3. Discussion of results

5.1 Domain, Mesh and Settings

The S400 was already briefly introduced in section 3.2. It is a burner, which consists of 408 jets. The jets are circular tubes protruding in the combustion chamber. The flames anchor at the jet exit, sometimes referred to as flame holders. Figure 5.1 contains the whole computational domain. The air fuel mixture enters on the left hand side into the plenum. The air does not enter in axial direction, but in the YZ-direction in the plenum. The mixture flows through slots into the jets. At the jet exit, the mixture burns. A part of the mixture is directed to the pilot flame. The center pilot flame is a large swirled flame, which has a great impact on the stability of the system with regard to IFD instabilities [15].

The settings of the CFD calculation for the S400 overlap with the settings used in section 3.2 for the StarCCM+ calculations. The mesh is slightly different. While again 14 cells per flame diameter is used, the jet carrier region is an imported region and must be resolved accurately. Below is an overview of the generated mesh for the S400 and boundary conditions are described in more detail.

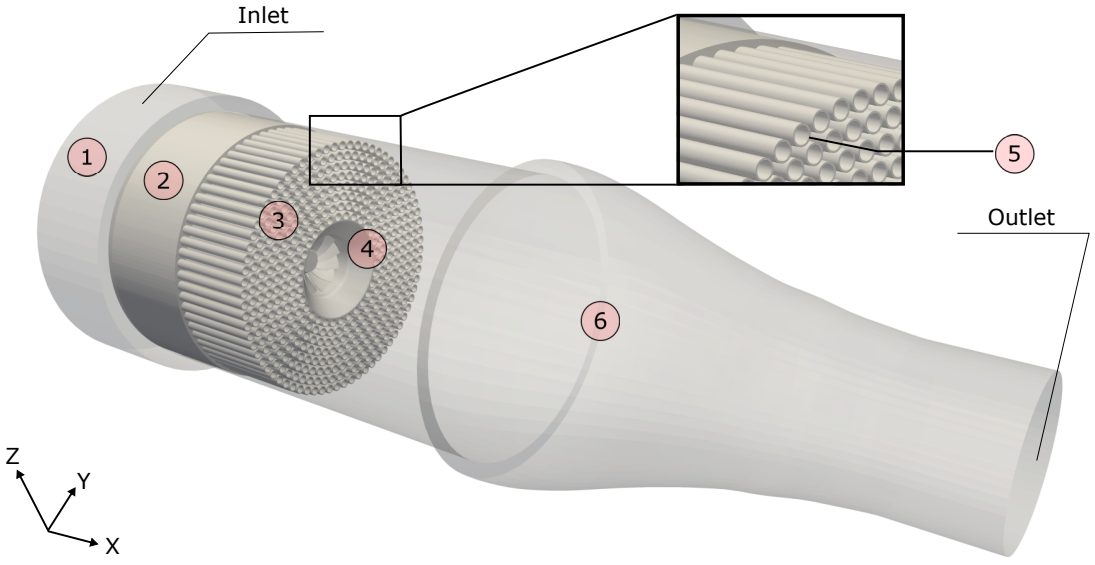

Figure 5.1: Overview of the computational domain of the S400 burner. With, (1) the plenum, (2) the slots, (3) the jets/jets, (4) the pilot/swirler, (5) the area outside the protruding jets (jet carrier) and (6) the transition.

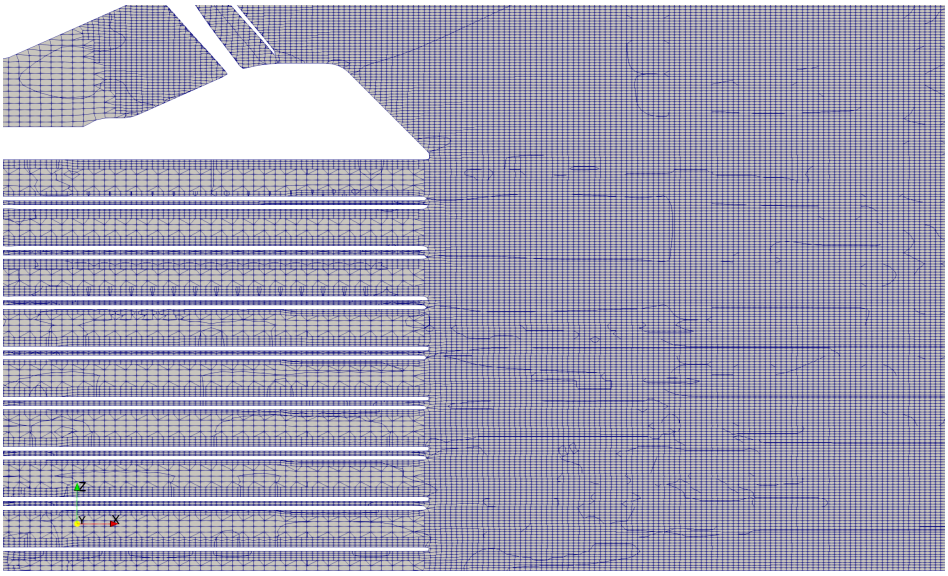

(a) Mesh side view

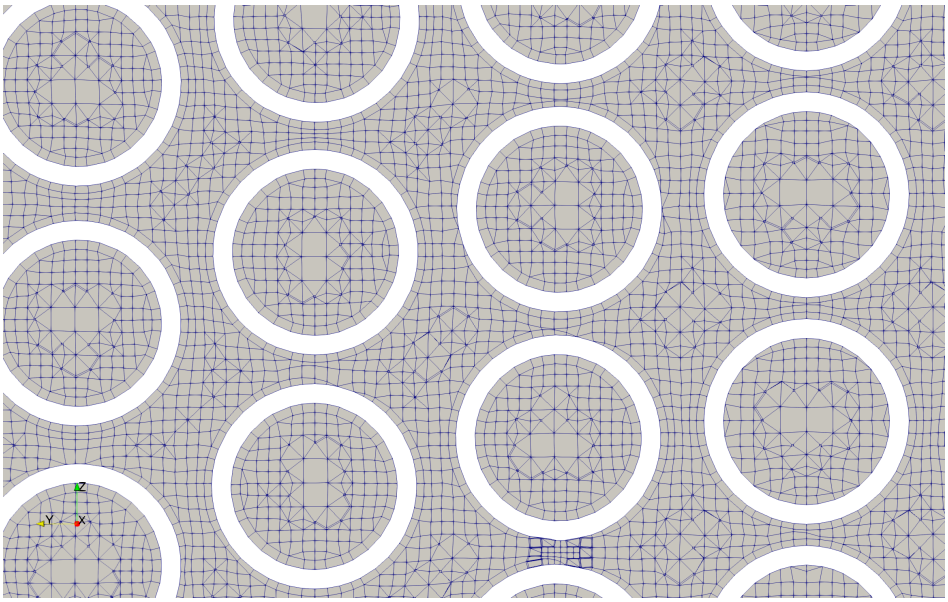

(b) Mesh front view jets

Figure 5.2: Images of the mesh for the S400 burner. The upper image is a cut through the domain in the XZ-plane, the lower image is a cut through of the mesh in the jets in the YZ-plane.

5.1.1 Baffles

The S400, which is an assembly name for the numbers 2, 3 and 4 from Figure 5.1, can be modified to contain baffles. The baffles consist of elongated jets and material has been added between the elongated jets to prevent fluid from flowing in between baffle compartments in circumferential direction. The elongation of the jets is done over a row of jets spanning from the pilot to the outer wall. A total of six baffles are added to the S400, with an elongation of 50 mm into the flame region. Therefore the amount of baffle compartments is also equal to six. The resulting geometries of the S400 with and without baffles can be found in Figure 5.3.

5.1.2 Mesh

The generated mesh of the S400 computational domain is roughly divided in four parts, namely the jet carrier region, the jets, the flame region and the remaining parts. Especially the jet carrier region required special attention. Figure 5.2 shows two snapshots of the generated mesh. Below are all important mesh regions briefly described.

Jet Carrier

The space between jets could be as small as 1 mm. In between these jets, at least three cells are necessary in order to capture viscous effects on the thermoacoustics by the shearing over the jets. The result is that a cell size of approximately 0.33 mm was required to resolve the jet carrier region, denoted as (5) in Figure 5.1. Figure 5.2 shows the generated mesh. Figure 5.2b is a 2D cut trough in the Y-Z plane in the jet carrier region. It is expected that the eigenmodes oscillate through the jet carrier region. The small gaps between the jets should

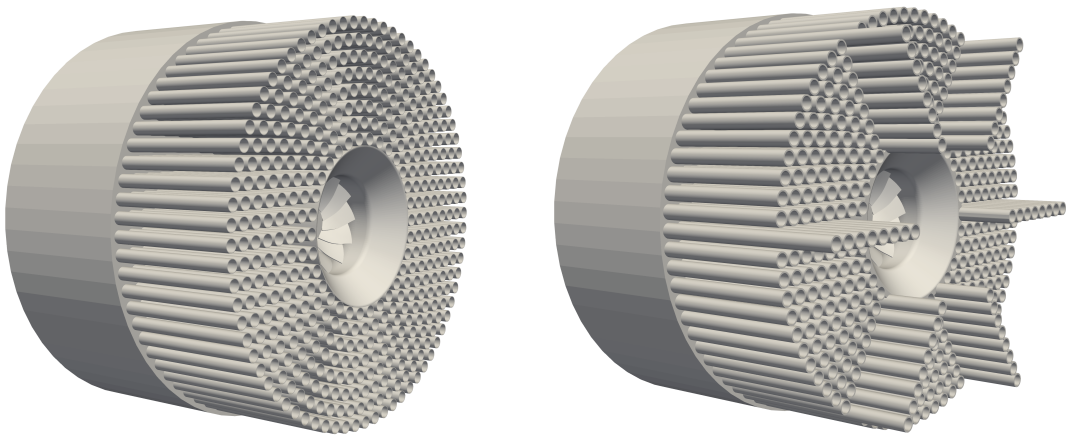

(a) Without Baffles **(b)** With Baffles

Figure 5.3: The geometries of the S400 with and without baffles

have a damping effect due to viscosity effects. Therefore it is important to refine the mesh in the jet carrier region.

The outside wall of the jets contains a layer, shown in Figure 5.2b. *SnappyHexMesh* had difficulties extruding all layers when they became too small, so the resulting layer size is a trade-off between what is possible and what is desired. Multiple smaller layers would have been better to capture all viscosity effects, but was never achieved. The mesh contains larger cells in regions further away from the jets. The resulting mesh is far from uniform in this region. When the cells between the jets became too small, *snappyHexMesh* would convert the area into artificial baffles by merging the jets. Local refinements had to be made to prevent this, which can be seen in the lower half of Figure 5.2b.

Jets

The jets have been resolved slightly different as in the sample case from section 3.2. Instead of two layers, now one layer is extracted. This had a practical reason, *SnappyHexMesh* was unable to extract two layers for all the jets. Even in the current set up with only one layer, it was not always possible to extract the layers, visible on the right hand side of Figure 5.2b. However, the neighbouring cells in the jets are approximately the same size as the layers, meaning that the loss of the second layer is negligible. The layer size is set so that the y^+ value equals approximately 50 in the jets. The core of the jets is less resolved, the save-up in cells was in the order of a million cells, while the accuracy is not compromised [96].

Flame Region

In section 4.1 it was shown that even 10 cells per flame diameter can still predict quite accurately the thermoacoustics in a system. Every refinement level increases the amount of cells with a factor of 2^3. Ten cells per flame diameter would mean a significant reduction of cells. However, it turned out that a more optimum ratio of refinements and total amount of cells could be achieved when 14 cells per flame diameter is used. Less cells per flame diameter required more local refinements in the jet carrier region. In the end the local refinements contributed so heavily to the total amount of cells, that it was more economical to use 14 cells per flame diameter.
The refined flame area span from the jet exit, to 175 mm in downstream direction over the whole crossection. Fluctuations in axial flame lengths are then also captured on this finer mesh.

Other regions

The remaining regions are the plenum, the slots and the transition. In these regions the least amount of interesting activity is expected. After the initial refinement in the flame region, the region in the transition has half the mesh refinement the flame region has. The slots had 7 cells per diameter and the plenum was not refined. The largest cells in the plenum were approximately 5 mm in length. The swirler is refined until no more artificial baffles between the swirler blades exists.

End Result

The total amount of cells for the full domain of the S400 is 37 million. The length of the cells in the flame and jet carrier region in transverse direction is 0.7 mm. The speed of sound in the burned region is about 800 ms^{-1}. The wave length for a frequency of 10 kHz equals 0.081 m here. The amount of cells per wave is then > 100.

5.1.3 Settings

All simulations in this section resolve no mixing, a perfect mixture is assumed. Moreover, the same schemes as in section 3.2 are used. The boundary conditions are of more importance for the S400. Methane, CH_4, is the inserted fuel.

Schemes and CFL number

The same schemes from Table 3.1 apply here. For the CFL in the flame and jet carrier region a value of 2 was the result of the chosen time step, namely $1.5E-6$ s. The grid size, combined with this CFL number should enable the observation of very short waves [61]. The Co number is of less interest. Due to the fact that the SIMPLE algorithm is used, the solution is stable even for $Co > 1$. The amount of inner iterations is 7.

Boundary Conditions

Due to confidentially reasons, the absolute values of the mass flow and the fuel mixture fraction are not stated here. The inlet condition is a mass flow inlet. The outlet is set to a free-stream boundary condition in combination with a sponge layer. As previously seen in section 4.3, large longitudinal waves through the system can eliminate the transverse waves. The transverse waves do not reach the outlet and are therefore not affected by the sponge layer, while the system is cured of longitudinal waves. The correct outlet pressure is found by a RANS simulation. The operating pressure is 8 bar.

Furthermore, all walls are set to adiabatic. This is a deviation from the experimental setup, where heat transfer through walls is unavoidable. The adiabatic walls increase the amount of energy in the combustion chamber, which results in more thermal power per flame. An increase of thermal power should result in more observable transverse instabilities [13]. Subsequently, adiabatic walls are easy to implement in CFD.
The consequence is that the temperature near the walls and in the jet carrier region (there is no heat transfer between the unburnt mixture and burnt mixture in this region) is higher than in the experiments. It is known from Equation 2.45 that the wave length depends on the speed of sound and the speed of sound increases with temperature. The result is that for the same eigenmode, the corresponding frequencies in the simulations should be slightly higher.

5.2 Thermoacoustic Results

This section covers the numerical results of the simulations of the S400 with and without baffles. Both cases are run self-excited and pressure bombed. The self-excited cases are simulated for 100 ms of physical time, the pressure bombed cases for only 60 ms. This results section is divided into three parts, namely

- Pressure probe analysis
- Mode shapes
- Comparison with experimental data

The first two parts compare simulation results of the S400 without and with baffles. In the third part, the results of the simulations of the S400 with and without baffles are compared to the experimental results.

5.2.1 Pressure Probes

The results for a pressure probe for the S400 without baffles self-excited are shown in Figure 5.4. The figure is shaped the same as for example Figure 3.11. The Rayleigh criterion is no longer shown in Figure 5.4. The spectogram and FFT in Figure 5.4 indicate that the S400 without baffles has multiple unstable modes in the high frequency domain. After approximately 40 ms the first instabilities start to occur. Most prominent are the modes around 1.3 kHz and the higher order modes in the range of $7 - 10$ kHz. The modes around 1.3 kHz are found to be all 1T1L modes. Also, bursts of instabilities occur in the frequency range of $3 \sim 4$ kHz in the bombed case. The corresponding mode shapes can be found in subsection 5.2.2 or in the Appendix.
The acoustic results for the S400 without baffles and using the pressure bomb as an excitation mechanism are shown in Figure 5.5. Instabilities now occur from the start. Interestingly in the bombed case there is an unstable mode at 2 kHz, which is the 2T2L mode. In the experiments this mode was also active at a frequency of 1.8 kHz.

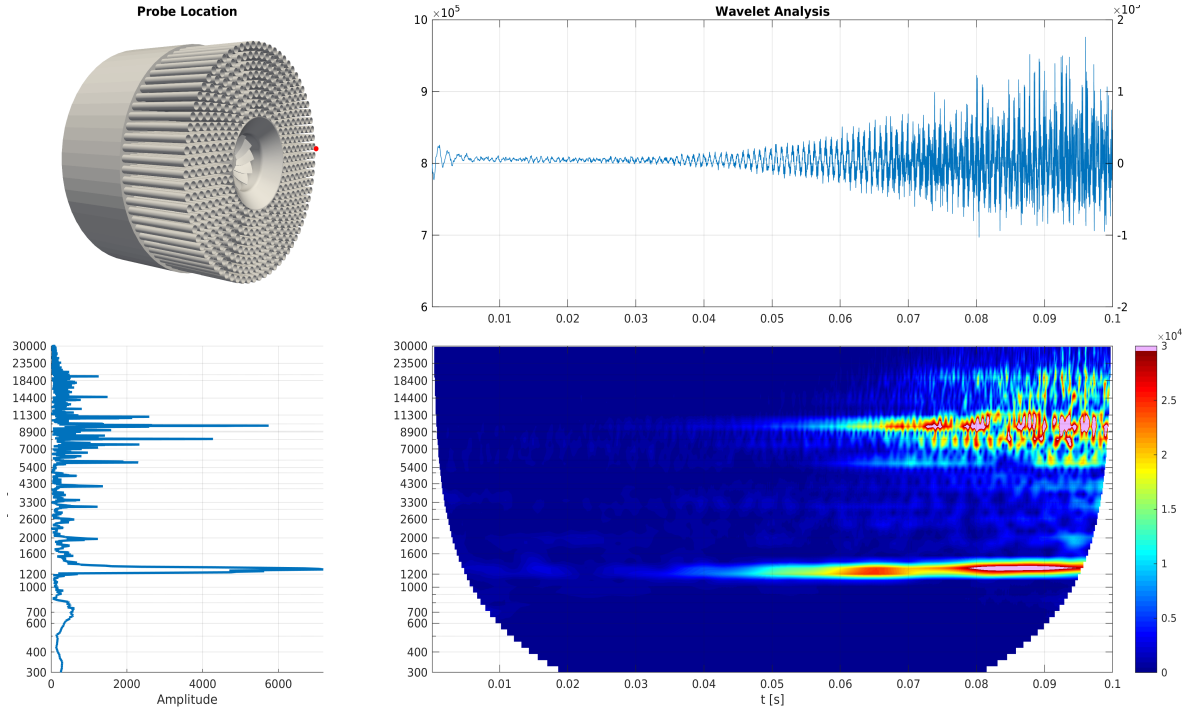

Figure 5.4: Acoustic analysis of the self-excited results of the S400 without baffles

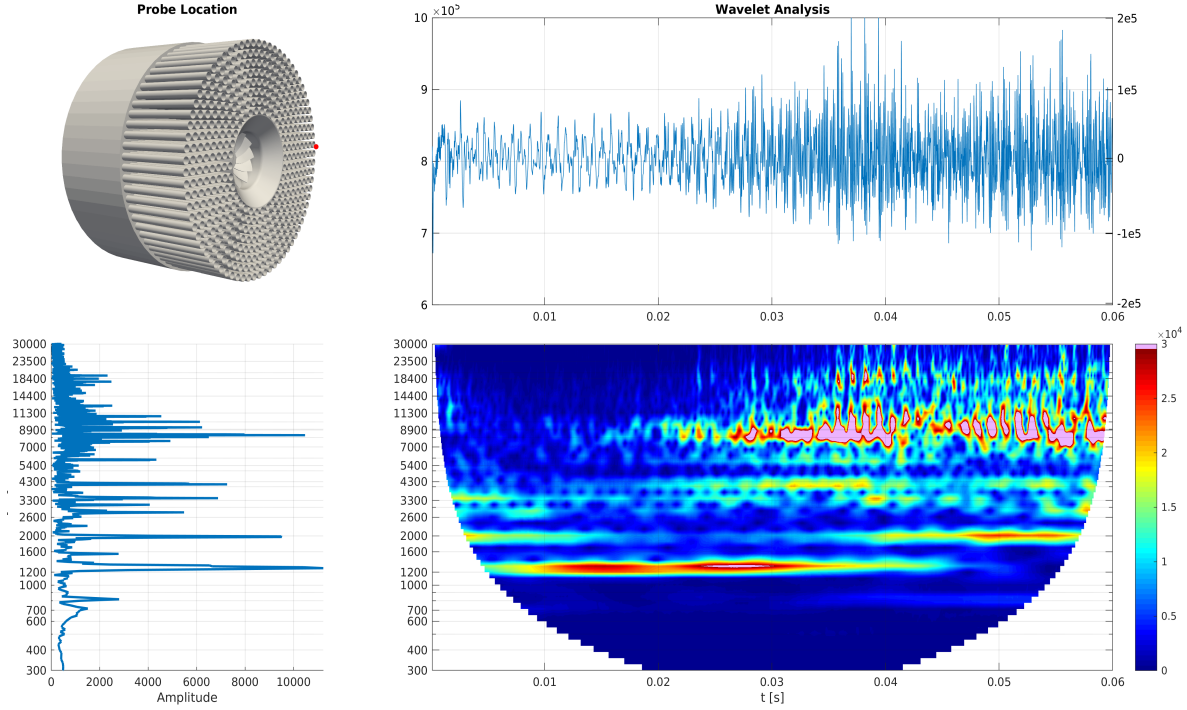

Figure 5.5: Acoustic analysis of the pressure bombed results of the S400 without baffles

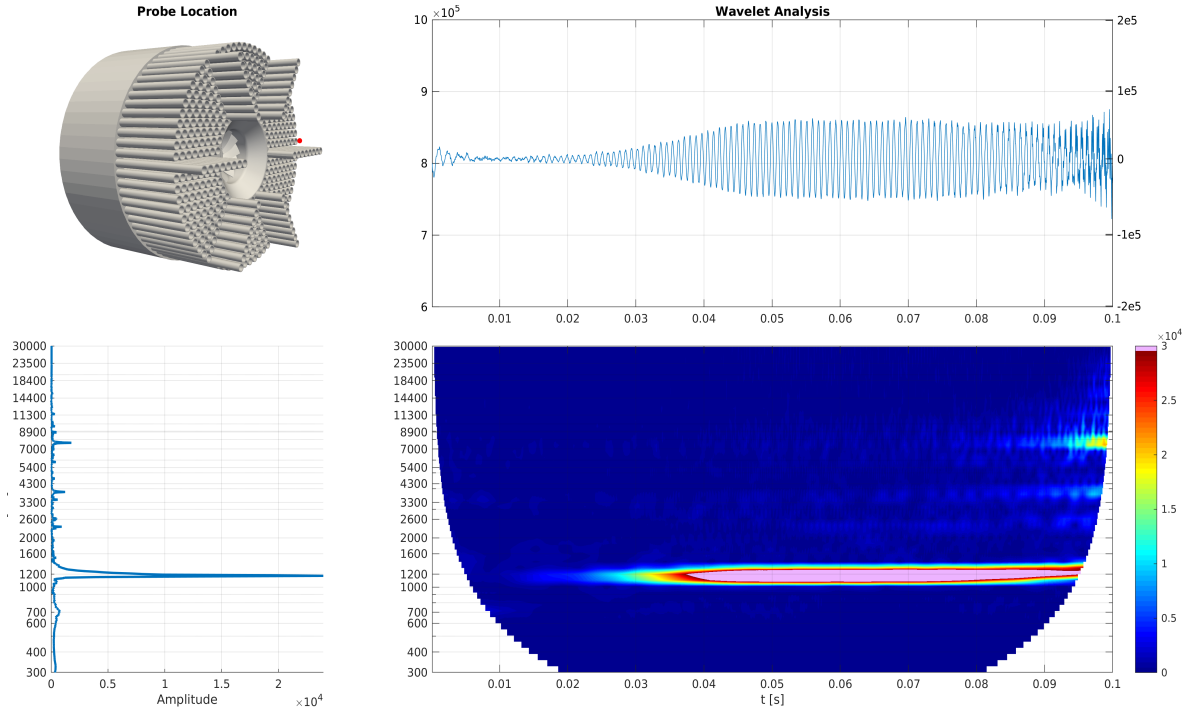

Figure 5.6: Acoustic analysis of the self-excited results of the S400 with baffles

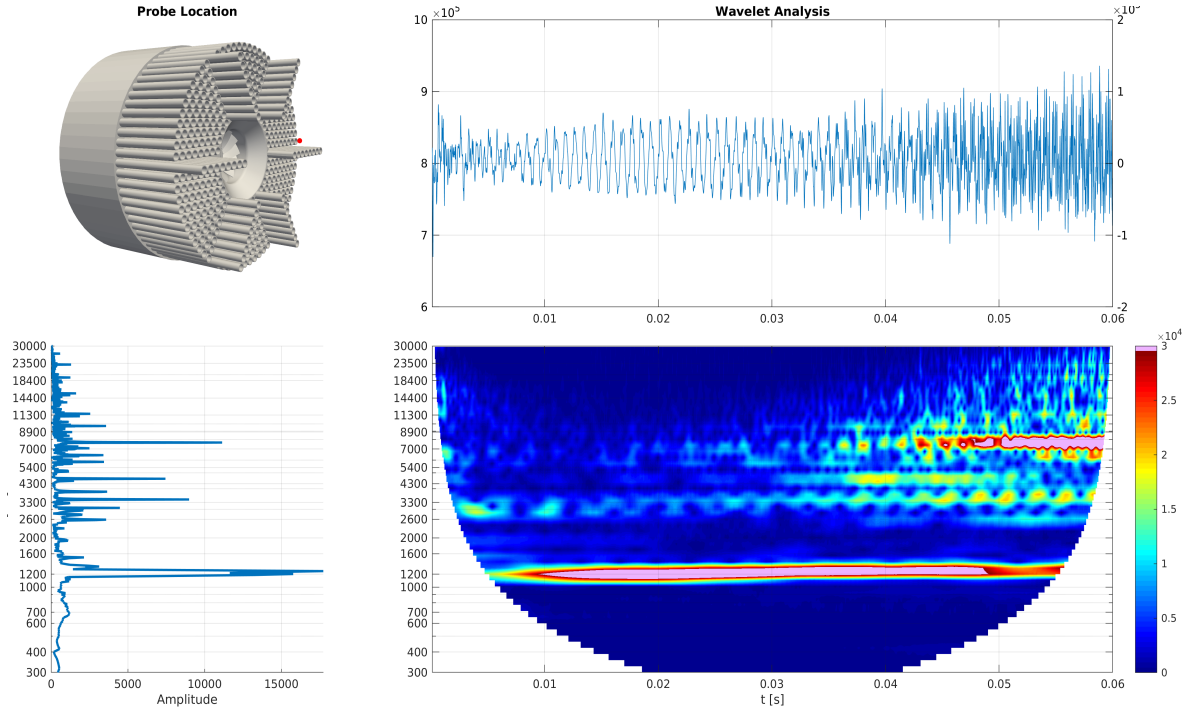

Figure 5.7: Acoustic analysis of the pressure bombed results of the S400 with baffles

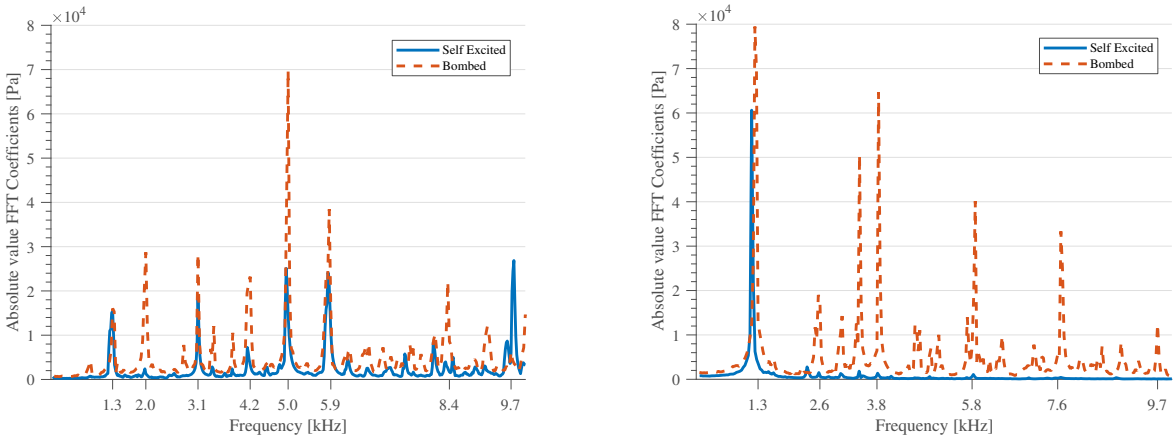

(a) S400 without baffles spectrum

(b) S400 with baffles spectrum

Figure 5.8: Frequency spectra for the S400 with and without baffles. The blue lines denote the self-excited cases and the dashed red line the bombed cases.

Figure 5.6 depicts the acoustic results of the S400 self-excited case with baffles. The difference between the S400 with and without baffles in these simulations is enthralling. For the first 90 ms in the self-excited baffled S400, no transverse thermoacoustic instabilities, except unstable 1T1L modes at $\sim 1200Hz$ occur. Later in the simulation, an instability at 7.6 kHz surfaces, which is the sixth transverse mode.
The bombed S400 with baffles (Figure 5.7) confirms the trend of the self-excited case. The 1T1L is very active and later in the simulations instabilities around 7.6 kHz arise. The experiments showed a significant reduction in amplitude for all transverse instabilities, also for the 1T1L, when the baffles were implemented. The simulations show the same trend for all transverse modes, except for the 1T1L and the sixth transverse mode. A more detailed explanation of this behaviour is given in section 5.3.

Based on the presented results, it is difficult to decisively conclude that the baffles cure a system of HFD. The derived amplitudes in the baffled S400 simulation remain quite high and the baffles seem to enhance the 1T1L mode. The signals in Figure 5.6-5.9 in this section indicate that the absolute pressure signal amplitude has a lower value for the S400 with baffles than for the S400 without baffles simulation. The comparison in signals of the bombed S400 with and without baffles indicates that the baffled S400 does not show these extreme high peaks.

The results, when using pressure signals for comparing two different geometries, can be misleading. The position of the mode is not constant for different geometries. For example it could be that for the S400 without baffles, the analyzed probe is exactly in the pressure antinode of an active frequency, while for the S400 with baffles for the same frequency the probe is in the node. Furthermore, analyzing only one probe means that some modes, which have their pressure node at the probe location are missed.
A method to overcome the last problem is to use multiple probes through the domain. In the simulations conducted in this chapter, over 500 probes were recording the pressure. All probes are decomposed. Per frequency, the ten maximum values are taken. Values outside of the 95% confidence interval are not taken into account. An average of the remaining values

per frequency is the result in Figure 5.8. The decomposition is done from $50ms \sim 100ms$ for the self-excited case and $30ms \sim 60ms$ for the bombed case.
Figure 5.8 proves that indeed some unstable modes were not observed by the pressure probes in Figure 5.4 till Figure 5.7. For example, the spectrum for the S400 without baffles clarifies that at 5.0 kHz and 5.9 kHz high amplitude modes exist, which were only vaguely seen in the spectrum of Figure 5.4 and Figure 5.5.
Figure 5.8b indicates that the thermoacoustic instabilities are much heavier in the S400 with baffles than in the S400 without baffles. However it has been argued before, that comparing different geometries for thermoacoustic behaviour is most likely to result in misleading results. Moreover, it is difficult to say whether the bombed case has reached a limit cycle for all the active modes in the spectrum in Figure 5.8. The pressure bombed approach only provides an indication here for which acoustic modes can become unstable in the domain.

Another point for discussion is the simulation time. Only 100 ms is simulated and it can be seen that for the S400 with baffles (Figure 5.6), around $90ms$ the pressure signal amplitude is increasing. More runtime would increase the accuracy of the results, however these simulations are expensive and therefore 100 ms was set as a limit of simulation time.

5.2.2 Mode Shapes

Figure 5.9 and Figure 5.10 represent the 1T1L mode in respectively the S400 without and with baffles. The result is a DFT over a 2D crossection in the Z-X plane and the Z-Y plane.

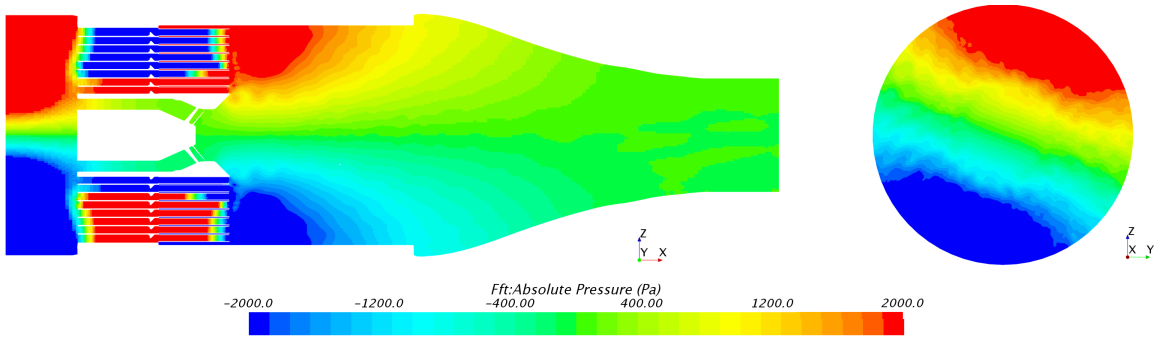

Figure 5.9: FFT of the 1T1L acoustic mode in the S400 without baffles - 1264 Hz

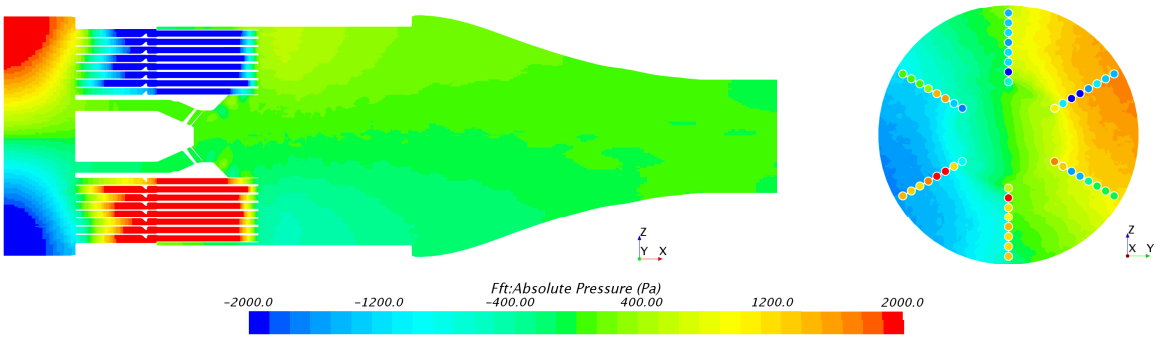

Figure 5.10: FFT of the 1T1L acoustic mode in the S400 with baffles - 1180 Hz

Other mode shapes of higher order can be found in the Appendix. In both geometries, the 1T1L mode oscillates mainly in the plenum, the ducts and the flame area. However it seems that the 1T1L of the baffled S400 is less active in the flame region, due to the fact that the pressure anti-nodes lie in the jets only, which contradicts what was derived in section 4.5, namely that the pressure anti-nodes must overlap with the heat release in space. The cut through shown in Figure 5.10 does not show that the 1T1L is actually heavily oscillating in the baffle compartments. This is confirmed by Figure 5.12.

The frequency of the 1T1L in the baffled S400 is lower than in the S400 without baffles. The pressure distribution of both modes provides an explanation why. As a consequence of the elongation of the ducts the region in which the acoustic mode is active contains more unburnt mixture. The speed of sound, which determines the wave length per frequency, is lower in colder mixtures. Therefore the frequency of the natural acoustic mode corresponding to the 1T1L will also be lower.

5.2.3 Comparison with Experiments

Based on the simulations the geometry can be altered and improved before it is tested in reality. This time it is the other way around, before the start of this thesis, experiments of a baffled combustor have already been conducted. The simulated geometries are generic approximations of the burners from the experiments. This subsection therefore covers the comparison between simulated results and experimental results, as far as that is possible.

Even though the simulated S400 domain is a generic approach of the experimental setup, a comparison between them is still interesting. Especially in the regime of 0 $Hz \sim 3000$ Hz, where the wave lengths are assumed too large to be influenced by small geometry changes. Table 5.1 contains the results of both the experiments and the simulations. The exact frequency and mode order are the compared values.
Due to confidentiality reasons, absolute amplitudes found in the experiments are not shown here. The experiments showed that the implementation of baffles in the S400 decreased the amplitude of the 1T1L such that the S400 could be operated at the optimum operating point, while it was on the edge of stability. The measurement position in the experiments is roughly at the same location as the probe in subsection 5.2.1.

Table 5.1: Active frequencies in S400 domain, simulations compared with experiments. The * denotes a guess, it is not sure whether the experimental frequencies equal the sixth transverse mode.

	Setup	$1T$	$1T1L$	$2T2L$	$6T^*$
Experiment	No Baffles	850 Hz	1170 Hz	1820 Hz	7500 Hz
Simulation	No Baffles	870 Hz	1260 Hz	2000 Hz	7700 Hz
Experiment	Baffled	850 Hz	1109 Hz	1750 Hz	7500 Hz
Simulation	Baffled	-	1180 Hz	2550 Hz	7700 Hz

Table 5.1 shows that the results from the simulations align with the experimental results. It has been argued before that the temperature in the S400 combustion chamber simulations is higher than in reality due to the adiabatic walls. The difference in temperature is most likely responsible for the difference in frequency for the active 1T1L and 2T2L mode.
It has been stated that introducing baffles in the domain will decrease the frequency of the transverse modes. This is confirmed by both the experiments and the simulations as shown in the third and fourth column of Table 5.1.

Previous simulations of similar cases [96] did not show any high frequency oscillations higher than the 1T1L mode, while their experimental counterpart later did show HFD. The settings used for the S400 simulations in this thesis result in a higher density of visible high frequency instabilities. The downside is that the used flame model predicts which eigenmodes of the system can become unstable, but is unable to provide usable results for the corresponding amplitudes.

So far no detailed explanation has been given as to why the exact behaviour of the experiments (where the S400 with baffles showed a significant decrease in amplitude for the 1T1L mode) is not reproduced in the simulations. The next section covers the in depth analysis of the thermoacoustic in the S400.

5.3 S400 Results Discussion

In the previous section it was derived by simulations that the implementation of baffles in the S400 caused (1) the frequencies of the transverse modes to lower, (2) the 1T1L mode to be the only remaining mode for the self-excited simulation and (3) the pressure bomb initialization resulted in a higher density of transverse instabilities. The high pressure tests indicated that implementing baffles in the S400 eliminated most of the high frequency oscillations, however the 1T1L mode remained unstable with a lower limit cycle amplitude than in the S400 without baffles. In this section, an in depth explanation about the differences between simulation and experimental results in the thermoacoustic trends is given. Furthermore, the question whether modes are standing or spinning in the S400 combustion chamber is answered.

5.3.1 Rotating Modes

In section 2.3 it was stated that the propagation of an acoustic wave is not always standing in a cylindrical geometry, but can also be rotating. Knowledge about the spatial behaviour of the acoustic mode allows for more fitting mitigation measures. For example, baffles are thought to prevent acoustic modes from spinning, due to the spatial blockage they form.

Figure 5.11 and Figure 5.12 visualize how the 1T1L mode propagates through the domain with and without baffles in a 2D-cut through the jet carrier region. It can be seen that for both cases the modes are spinning. This is unexpected, the baffles should prevent the 1T1L from spinning. To learn why the 1T1L is still spinning in the baffled S400 a closer look in to the flame behaviour is necessary, which is given in the Appendix. In order to derive Figure 5.11 and Figure 5.12 a DFT of the absolute pressure field over the 2D cut is made, with a sampling

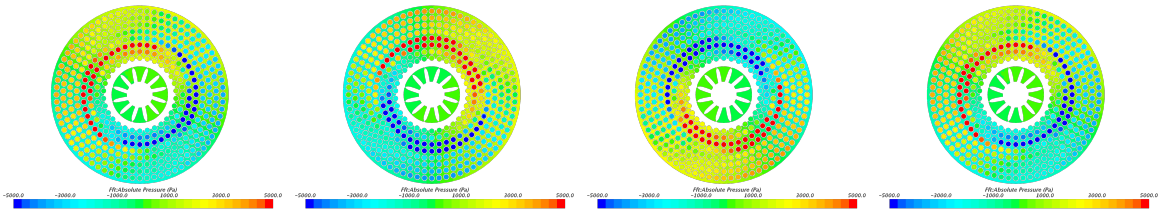

(a) t = 0 **(b)** t = $\frac{1}{3}T$ **(c)** t = $\frac{2}{3}T$ **(d)** t = T

Figure 5.11: Clockwise Rotating behaviour of the 1T1L in the S400 without baffles

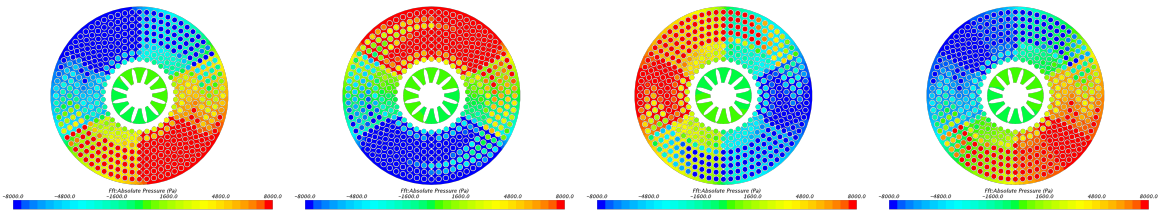

(a) t = 0 **(b)** t = $\frac{1}{3}T$ **(c)** t = $\frac{2}{3}T$ **(d)** t = T

Figure 5.12: Counter Clockwise Rotating behaviour of the 1T1L in the S400 with baffles

time of 20 ms. The propagation (Figure 5.11 and Figure 5.12 a to d) is then derived by taking different starting points of the DFT in one period of the pressure oscillation.

Figure 5.11 indicates that the 1T1L in the S400 without baffles has lower amplitudes in the jet carrier region than in the jets. It seems that the mode is driven by the pumping effect of the jets, which was previously seen in section 4.4. Also, especially the third and fourth row of ducts are active for the 1T1L mode. Remember that the fluid in the ducts is cold, while the temperature of the fluid in the jet carrier region is hot and that the length of a wave depends on the temperature of the medium. The acoustic mode corresponding to the radius of the third and fourth row of jets couples with the acoustic mode corresponding to the diameter of the combustion chamber. The reason why there are two rows of jets active and not one, is that the outer of the two rows of jets probably has a slightly lower eigenfrequency than the combustion chamber eigenfrequency and the inner row of jets a slightly higher one.

In the S400 with baffles, there seems to be no coupling between the third and fourth row of jets and the combustion chamber. In Figure 5.12 the 1T1L pressure anti-nodes move from baffle compartment to baffle compartment in the circumferential direction. Furthermore, the pressure in the jets of the S400 with baffles is ahead of the pressure field in the jet carrier region. This makes sense, the pressure in the jets couples with the pressure at the flames with a certain time lag, corresponding to the axial distance of the 2D cut to the flames. Later in this report it is shown that the lack of baffles in the centre (as for example in Figure 2.16) explains why the 1T1L rotates even though baffles are implemented.

Damping the transverse oscillations in a combustion chamber is usually conducted by Helmholtz resonators which are placed on the walls in the flame region. Therefore they consume quite some cooling air. Knowledge about the spatial orientation of the dominant mode, the 1T1L, enables new insights in possible mitigation strategies. For example, it has been shown that the jets acoustically couple with the combustion chamber. Meaning that

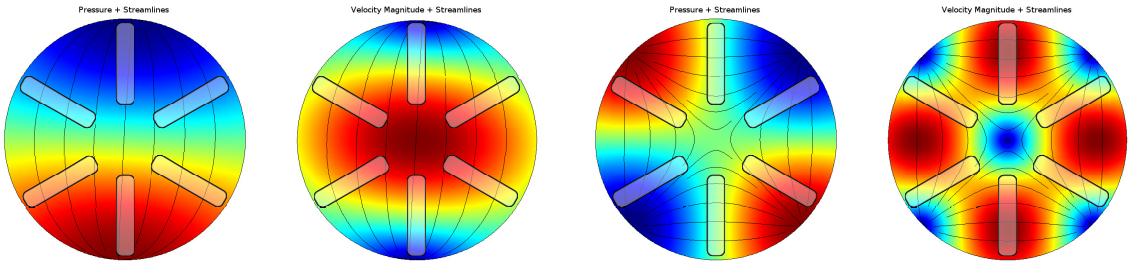

(a) 1T Pressure **(b)** 1T Velocity **(c)** 2T Pressure **(d)** 2T Velocity

Figure 5.10: The pressure and velocity distribution for the first and second transverse acoustic mode in a cylinder.

damping mechanisms could also be placed in the cold regime of the jets, where they do not require any cooling air.

5.3.2 The First Transverse Mode

A pressing question is why the 1T1L is not acoustically damped by the simulated baffle configuration. In subsection 2.5.2 it was already discussed that in order to affect the first transverse mode in a combustion chamber, the amount of baffles should not be an even integer. The S400 contained six baffles, thus violating this rule. Furthermore, the S400 did not have a baffle hub such as in Figure 2.16. While not explicitly mentioned by Harje and Reardon [16], the hub probably has a significant damping impact on the first transverse mode.

The latter is explained by having an idea how the acoustic pressure and velocity are distributed for the transverse modes in a cylinder. Figure 5.10 visualizes this. The orientation of the baffles as implemented in the S400 is indicated by the transparent blocks in the figures. The colors blue and red denote the minima and maxima of the acoustic pressure and velocity. It can be observed that the 1T has a velocity maximum in the core of the cylinder, see Figure 5.10b. In the S400, the centre is not baffled. This means that the velocity anti-node of the 1T is not affected by the baffles. For comparison, the 2T acoustic pressure and velocity distribution is also shown (Figure 5.10c). The velocity anti-nodes are in the outer region of the cylinder. The baffles form blockades in the velocity anti-nodes of the 2T and therefore the 2T can not sustain. The streamlines confirm this hypothesis. For the 2T, the baffles interfere with almost all the streamlines, but for the 1T the streamlines in the core of the cylinder are partly untouched. Therefore, the 1T can sustain in the baffled setup.

The current implementation of the baffles in experimental combustor is sufficient to influence higher order transverse acoustic modes, but lacks the ability to damp the first transverse mode. In order to affect the first transverse mode, symmetry of baffle compartments should be avoided and a baffle hub could be implemented.

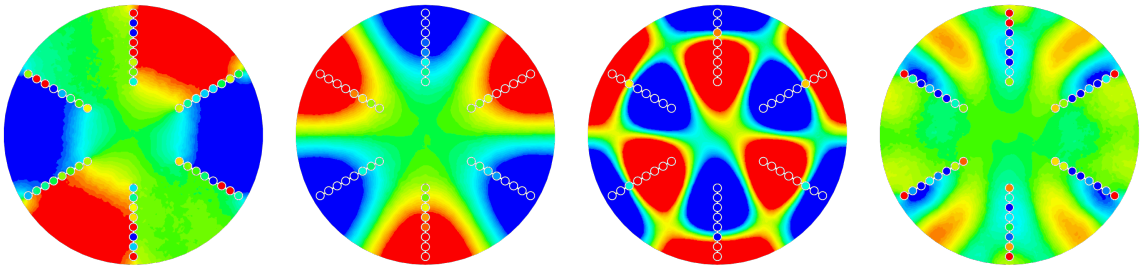

(a) 3067 Hz **(b)** 3800 Hz **(c)** 5867 Hz **(d)** 7700 Hz

Figure 5.11: Acoustic modes in the S400 with baffles, from the pressure bombed calculation

5.3.3 Higher Order Modes

Previously, it was shown that in the pressure bombed S400 with baffles case multiple higher order modes sustain. Whether they would sustain if a longer period of physical time would be simulated can not be answered here. However it is interesting to find out why especially these modes are triggered by the pressure bomb. Figure 5.11 contains the pressure distribution over a 2-D cut through the flame region of the four most active acoustic modes in the S400 with baffles simulation according to Figure 5.8.

Figure 5.11a shows that the 3067 Hz ($2T$) mode also benefits from the symmetry and lack of baffles in the centre of the domain and can therefore sustain. The other three figures show that their modes sustain in a baffle compartment. The 5867 Hz is a $3T1R$ mode and is also able to sustain per compartment. Interestingly, the 7700 Hz mode can be identified as a sixth transverse mode, but does not seem to be so intense in the 2-D cut as the other modes, while having a significant amplitude in Figure 5.8. With the current data, it is difficult to derive what the cause of the instability at this frequency is. It could be that the pressure anti-nodes are exactly very intense between this 2-D cut and the jet exit. Furthermore, it is suspicious that the order of the mode equals the amount of baffle compartments.

This subsection confirms the importance of a baffle hub. Some modes are able to sustain due to the lack of it. Moreover, higher order modes which fit in the baffle compartments may still be a problem. It would be interesting to simulate in the future the influence of the baffle gaps as discussed in section 2.5 on these higher order modes.

5.4 Conclusion

In the experiments the baffles had a significant impact on the stability of the system. The amplitude of the 1T1L was significantly lower with baffles implemented in the S400 and all the other higher order modes were also of less amplitude. The simulation results did not fully align with the experimental results. The amplitude of the 1T1L acoustic mode when the baffles were implemented in the simulations actually increased. On the other hand, there are indications that the simulations are able to predict that the baffles have a damping effect on higher order transverse modes. Below is a summary of all the uncertainties that come with these kinds of experiments and simulations.

- The experiments were conducted with only two pressure measurement points. Discussed before in subsection 5.2.1, this can lead to missing important higher order modes that have a pressure node at these two measurement points. Axial displacement of acoustic modes due to geometry changes can lead to misleading information about the acoustic modes.
- The FGM Kinetic Rate flame model is extremely responsive to thermoacoustic instabilities. Possibly too responsive. The derived amplitudes are three orders of magnitude higher than in experiments. It is thereby difficult to conclude something about the amplitudes of the instabilities.
- The observed simulation time is much smaller than the observed experimental time. It could be that acoustic activity is not observed, due to the fact that it has not surfaced yet.
- The mesh is quite coarse in the jet carrier region. Sometimes only two cells are responsible for capturing all the viscous effects. Therefore, numerical dissipation could influence the acoustic damping by viscosity effects.

Taking into account all the uncertainties, there are definitely conclusions to be drawn from the simulations of the S400. The most pressing are

- The lack of a baffle hub, which closes all the baffle compartments of from each other, allows the first transverse to bypass the baffles.
- Equal sized baffle compartments allow higher order acoustic modes with wave lengths equal to the baffle compartment size to fit in these compartments. Therefore the baffle compartments should not all be of equal size.
- The 1T1L, the most dominant mode in both cases, is a rotating and not a standing wave. Surprisingly, it also rotates in the baffled setup. This is probably due to the pilot flame, which drives the flames in the compartments. More information about this can be found in the Appendix.
- The simulations show the same trends as the experiments. Namely that the implementation of baffles in a system lowers the frequency of the 1T1L. On top of that, the frequencies of the first unstable frequencies are not far off from each other and the difference can be explained by the difference in temperature in the domain, especially in the jet carrier region.

Chapter 6

Conclusion and Recommendations

In this concluding chapter, the research questions are evaluated. Recommendations based upon the simulations conducted in this thesis are given in the second section of this chapter. Uncertainties with regard to the conducted simulations can be found in the sub conclusion of the previous chapter (section 5.4). The primary research question is stated here again

- What is the damping ability by baffles in a gas turbine combustion chamber with regard to transverse acoustic oscillations?

And the secondary research questions were

- What are the optimum settings for simulating transverse combustion instabilities?
- How do the flames couple to transverse oscillations and what does their spatial movement looks like?
- Can a method be derived to predict a priory which (transverse) eigenfrequencies of a domain are most likely to become unstable?

6.1 Conclusion

The aim of this thesis is to provide more insight in the damping induced by implementing baffles in an industrial scale gas turbine combustion chamber with regard to transverse combustion instabilities. SIEMENS conducted experiments on a burner, named the S400, and it is tested with and without baffles.

The optimum settings for simulating high frequency combustion instabilities were derived in the third chapter. The simulations conducted with the FGM Kinetic Rate flame model in StarCCM+ resulted in more visible high frequency instabilities. Both self-excited and pressure bombed transverse oscillations were observed in the simulations conducted on a small domain. Based on these simulations, the other two secondary research questions could be answered.

A newly implemented post-processing technique enabled to track the movement of the heat release centres per flame. It is confirmed in this thesis that the flame centres oscillate with the same frequencies as the acoustic frequencies in the combustor and thereby confirming the latest research conducted on this topic [14, 107]. In more detail, it was shown that flames burning in the pressure anti-nodes of a transverse acoustic mode oscillate in longitudinal direction due to the switch of high and low pressure in these regions. The centre flames are heavily influenced by the velocity anti-node and their motion is in transverse direction.

The eigenfrequency solver from COMSOL Multiphysics was used to further verify the Computational Fluid Dynamics (CFD) results. The eigenmodes found by COMSOL were similar to the acoustic modes found in CFD. Depending on the geometry the eigenfrequency solver finds hundreds of eigenmodes. In order to distinguish the COMSOL derived eigenmodes, they had to be handpicked. The question arose if there is a method that could simplify this process.
To answer this question, the so called Poor Man's Rayleigh (PMR) criterion was introduced. This formulation determines a value based on the overlap of the pressure anti-nodes with the heat release of the flames. It is called the Poor Man's Rayleigh criterion, because the heat release is a mean value from a RANS simulation. The results of the PMR criterion were promising and besides it being a helpful tool for selecting the right eigenmodes, it also has potential to enable optimizing combustion chambers in the frequency domain.

With the newly acquired insights in flame behaviour under the influence of transverse thermoacoustics instabilities, the impact of the baffles on the acoustic stability of the S400 is studied. Six baffles equally dividing the cross sectional area of the combustion chamber were elongated 50 mm into the domain. The experimental results indicated that the baffles damped the transverse instabilities in the S400, but the results were not decisive and especially the first transverse mode remained active.
The simulation results did not provide a decisive answer on the primary research question. The simulation results indicated that the first transverse mode can sustain in the combustion chamber, due to the fact that the centre of the combustion chamber is not blocked off by baffles. Moreover, it has been deduced that the transverse modes (in the simulation) are not standing waves, but rotate in the domain and that the premix passages acoustically couple with the combustion chamber. Moreover, it was also captured by the simulations that implementing baffles in a combustion chamber results in a lower frequency for the first transverse first longitudinal acoustic mode, which was also observed in the high pressure tests. In terms of acoustic amplitudes it proved difficult to derive answers. The amplitudes in the simulations are three orders of magnitude higher than in the experiments. However, the simulations did provide insight in the mechanisms of transverse combustion instabilities in both the smaller domain and the S400 with and without baffles.

6.2 Recommendations

Throughout this thesis, many recommendations are given. This section provides a summary of the most important and elaborates on them. Two kinds of recommendations are given here, namely design recommendations for a combustion chamber containing baffles and recommendations for further research.

6.2.1 Design Recommendations

Below are the design recommendations for improving the baffle configuration in the S400 combustion chamber with regard to transverse thermoacoustic instabilities based on the numerical results derived in this work:

- Implement a baffle hub such as in Figure 2.16 in order to eliminate the first transverse first longitudinal (1T1L) and other higher order modes with an acoustic velocity anti-node in the centre of the combustion chamber.
- Avoid symmetry of baffle compartments, it allows higher order acoustic modes to fit in a baffle compartment. On top of that, avoid an even number of baffles in order to deny symmetry of which the first transverse mode can benefit from.
- Baffle gaps (shown in Figure 2.16) are not taken into account in this thesis, but could succeed in eradicating higher order modes that fit in a baffle compartment.

6.2.2 Further Research Recommendations

The recommendations for further research based on the findings presented in this work are:

- Further develop the Poor Man's Rayleigh criterion and validate it. Validation can be done by modifying the geometry of the small domain in such a way that the PMR value of the 1T at 6500 Hz becomes lower than the 1T at 6800 Hz. Then use CFD and observe which 1T is the dominant mode. A $\frac{\lambda}{4}$ tube or a resonator are possible geometry modifications.
  In addition, the accuracy of the formulation will probably increase when the overlap of velocity anti-node with the heat release is also taken into account.
- Use PMR on the S400. Unfortunately the PMR formulation was not used on the S400, due to limitations in COMSOL. Hopefully new tools allow for automation of some pre- and post-processing steps in the future.
- Try to find an optimum baffle length as a function of flame length. In CFD, one could for example take the small domain from this work and use the 10 cells per flame diameter. In that domain extend a wall from the jet exits downstream. Use the pressure bomb and observe per wall length what occurs.
- Conduct simulations of a baffle configuration containing a baffle hub in the S400.
- Try a different flame model, such as the Turbulent Flame Speed closure, on the S400. The selection of the flame model was now based on the ability of triggering any high

frequency instability. It would be interesting to observe whether in for example TFC the same instabilities are observed and what their corresponding amplitudes are.

- The derived amplitudes with the FGM Kinetic Rate were three orders of magnitude higher than in the experiments. A different method of comparing acoustic results is by looking at growth rates of thermoacoustic instabilities. This approach could maybe used to overcome some of the issues encountered in this thesis.

Appendix A

Acoustic Mode Shapes

A.1 S400 without Baffles

All the acoustic modes of the S400 without baffles found by StarCCM+ are shown in this appendix. The selected mode shapes correspond to the results from Figure 5.8.

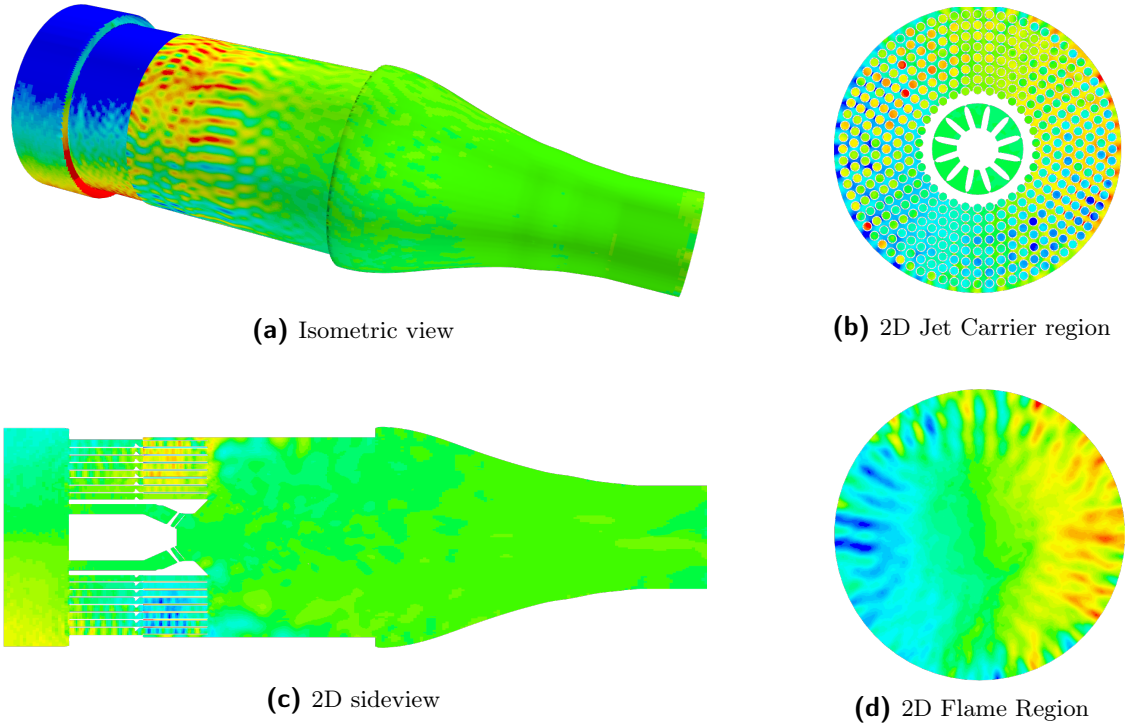

(a) Isometric view

(b) 2D Jet Carrier region

(c) 2D sideview

(d) 2D Flame Region

Figure A.1: S400 without Baffles 820 Hz Acoustic Mode Shape

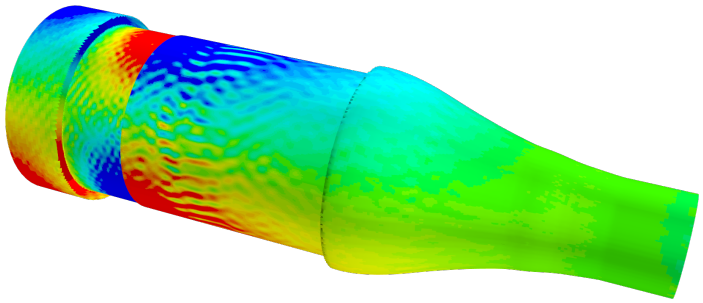

(a) Isometric view

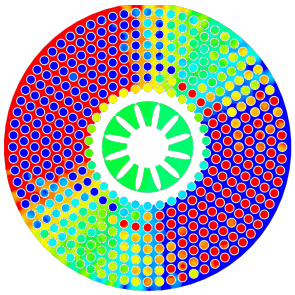

(b) 2D Jet Carrier region

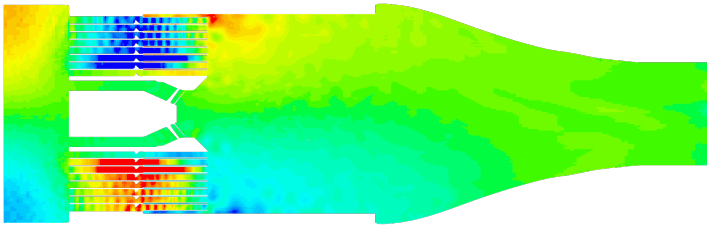

(c) 2D sideview

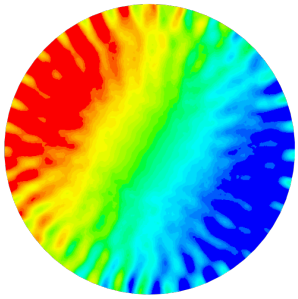

(d) 2D Flame Region

Figure A.2: S400 without Baffles 1300 Hz Acoustic Mode Shape

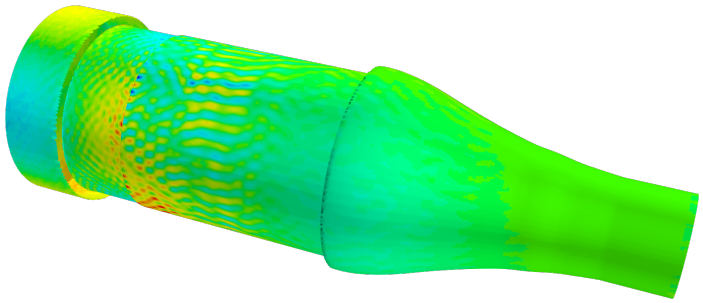

(a) Isometric view

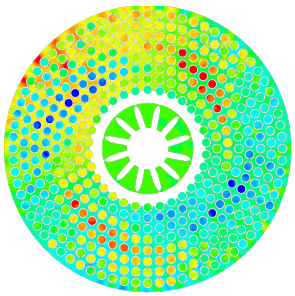

(b) 2D Jet Carrier region

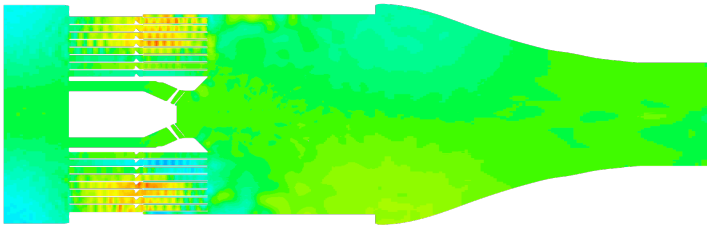

(c) 2D sideview

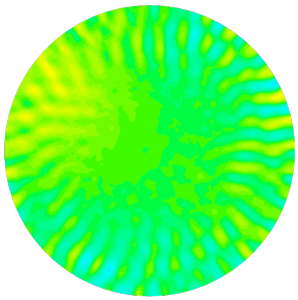

(d) 2D Flame Region

Figure A.3: S400 without Baffles 1550 Hz Acoustic Mode Shape

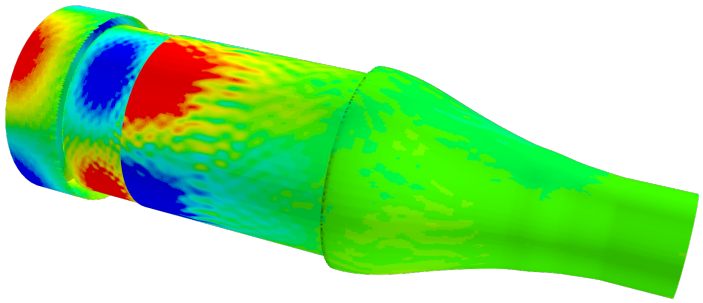

(a) Isometric view

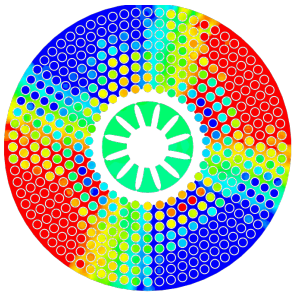

(b) 2D Jet Carrier region

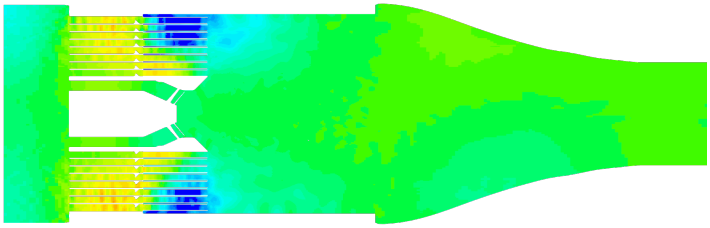

(c) 2D sideview

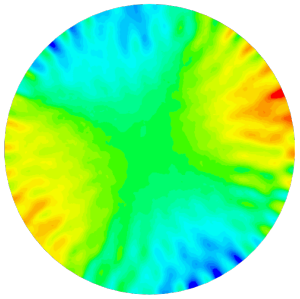

(d) 2D Flame Region

Figure A.4: S400 without Baffles 1950 Hz Acoustic Mode Shape

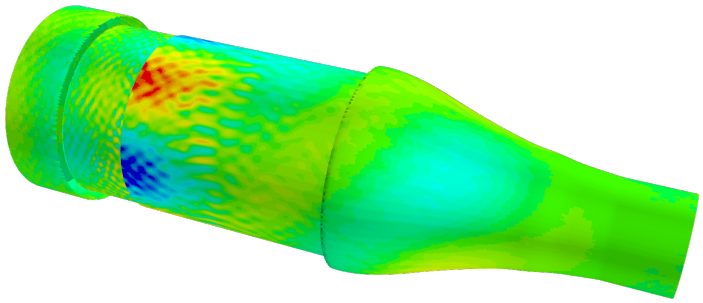

(a) Isometric view

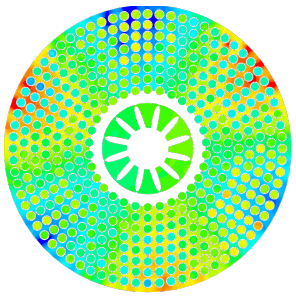

(b) 2D Jet Carrier region

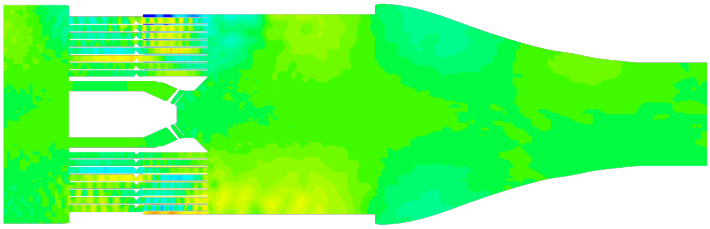

(c) 2D sideview

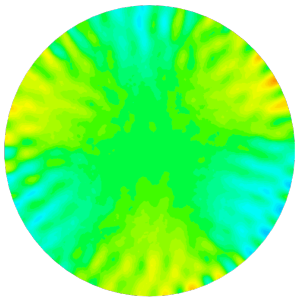

(d) 2D Flame Region

Figure A.5: S400 without Baffles 2780 Hz Acoustic Mode Shape

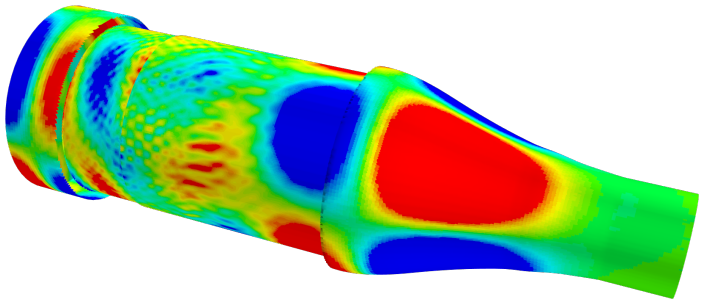

(a) Isometric view

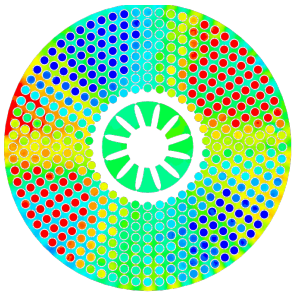

(b) 2D Jet Carrier region

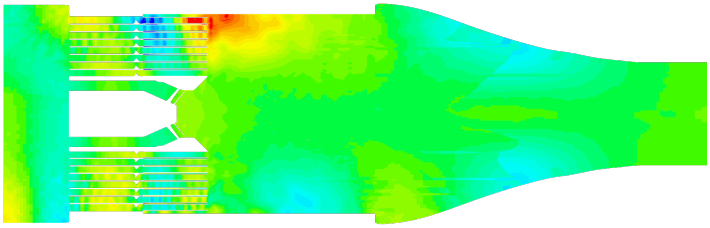

(c) 2D sideview

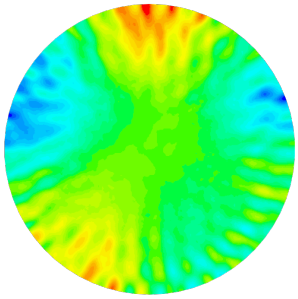

(d) 2D Flame Region

Figure A.6: S400 without Baffles 3100 Hz Acoustic Mode Shape

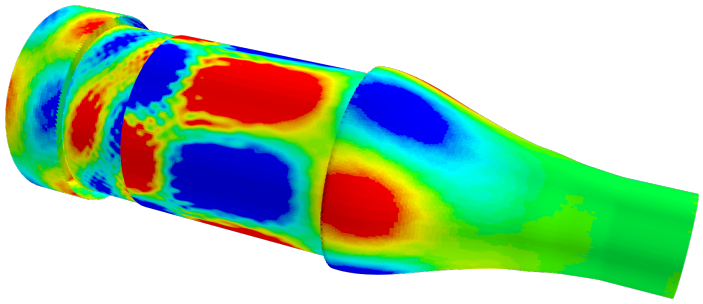

(a) Isometric view

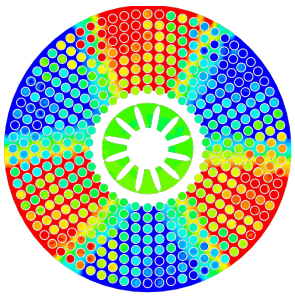

(b) 2D Jet Carrier region

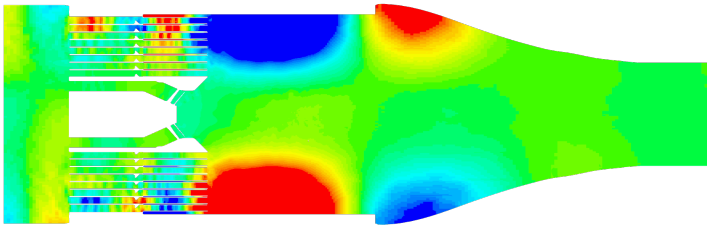

(c) 2D sideview

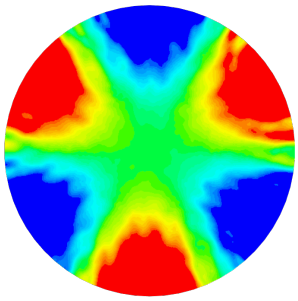

(d) 2D Flame Region

Figure A.7: S400 without Baffles 3400 Hz Acoustic Mode Shape

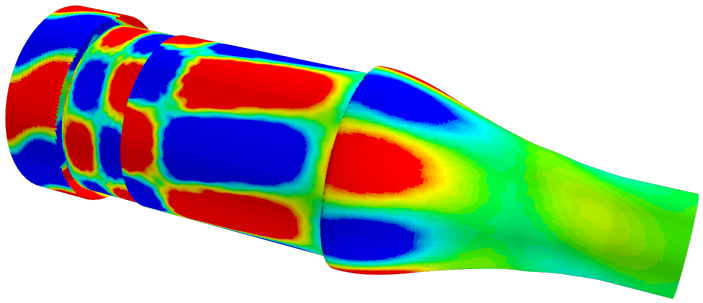

(a) Isometric view

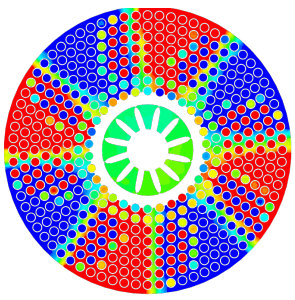

(b) 2D Jet Carrier region

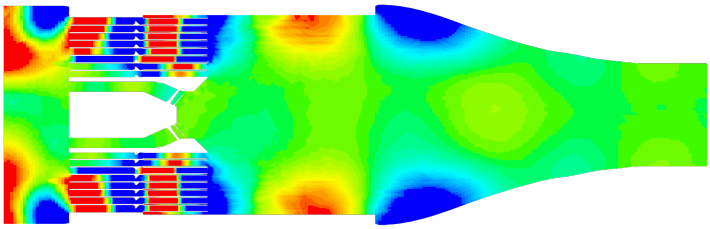

(c) 2D sideview

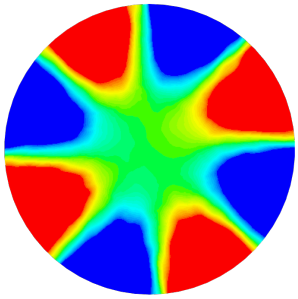

(d) 2D Flame Region

Figure A.8: S400 without Baffles 4150 Hz Acoustic Mode Shape

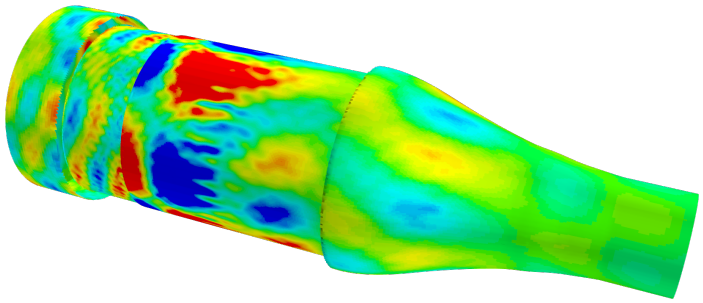

(a) Isometric view

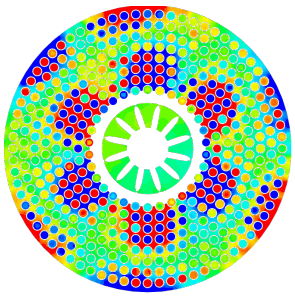

(b) 2D Jet Carrier region

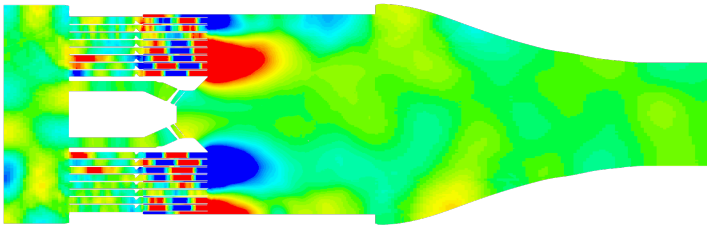

(c) 2D sideview

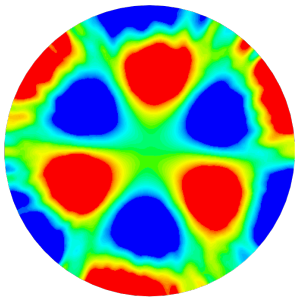

(d) 2D Flame Region

Figure A.9: S400 without Baffles 5850 Hz Acoustic Mode Shape

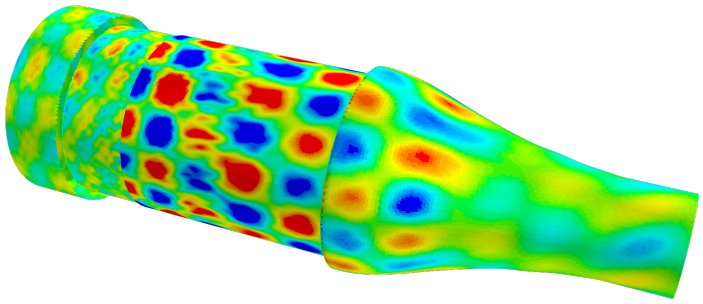

(a) Isometric view

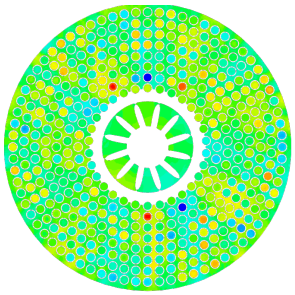

(b) 2D Jet Carrier region

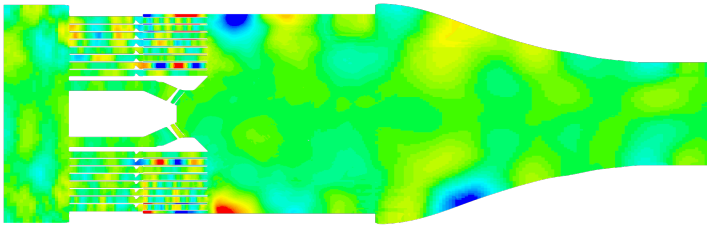

(c) 2D sideview

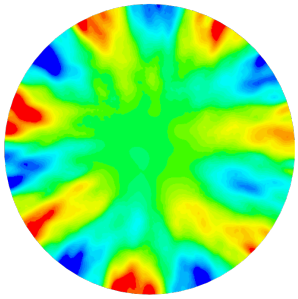

(d) 2D Flame Region

Figure A.10: S400 without Baffles 7650 Hz Acoustic Mode Shape

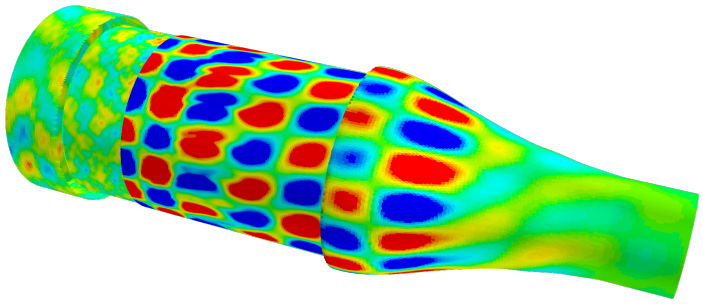

(a) Isometric view

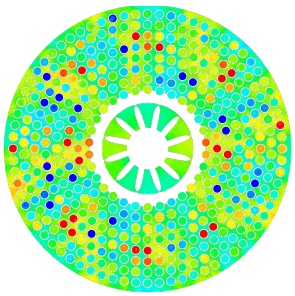

(b) 2D Jet Carrier region

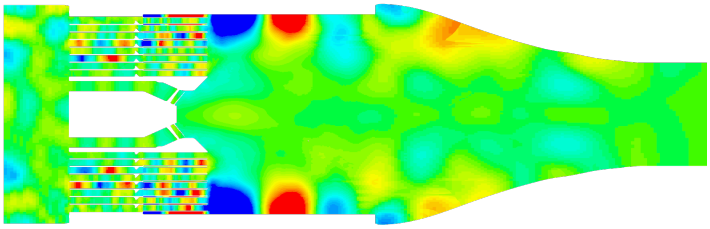

(c) 2D sideview

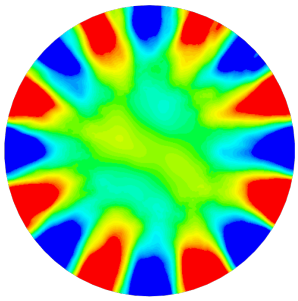

(d) 2D Flame Region

Figure A.11: S400 without Baffles 8300 Hz Acoustic Mode Shape

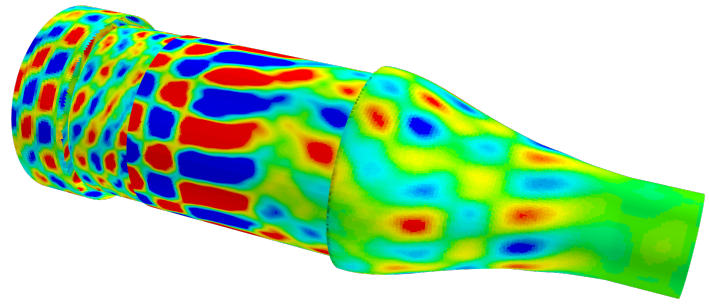

(a) Isometric view

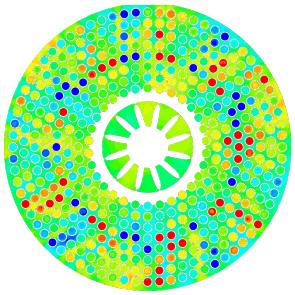

(b) 2D Jet Carrier region

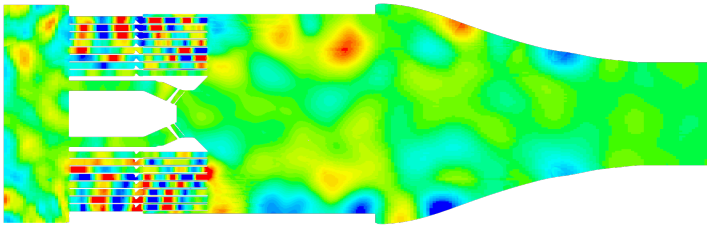

(c) 2D sideview

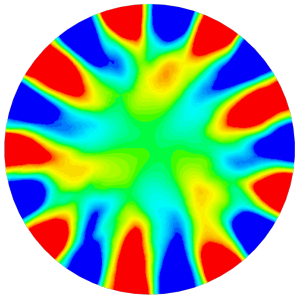

(d) 2D Flame Region

Figure A.12: S400 without Baffles 9250 Hz Acoustic Mode Shape

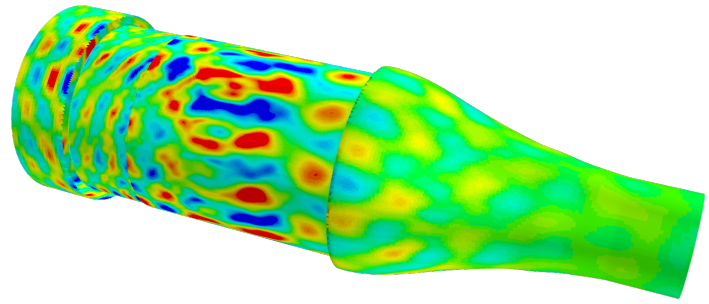

(a) Isometric view

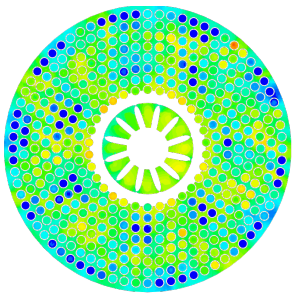

(b) 2D Jet Carrier region

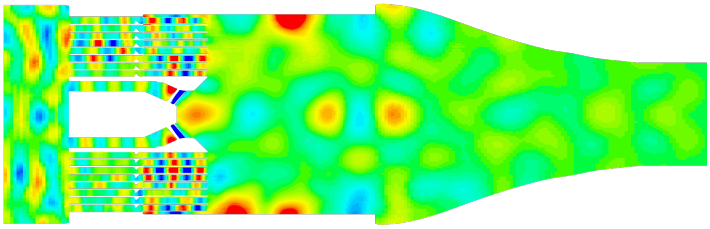

(c) 2D sideview

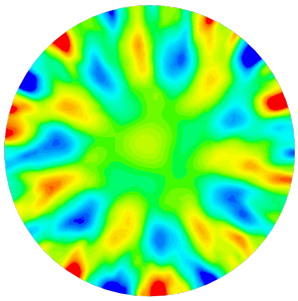

(d) 2D Flame Region

Figure A.13: S400 without Baffles 10000 Hz Acoustic Mode Shape

A.2 S400 with Baffles

All the acoustic modes of the S400 with baffles found by StarCCM+ are shown in this appendix. The selected mode shapes correspond to the results from Figure 5.8.

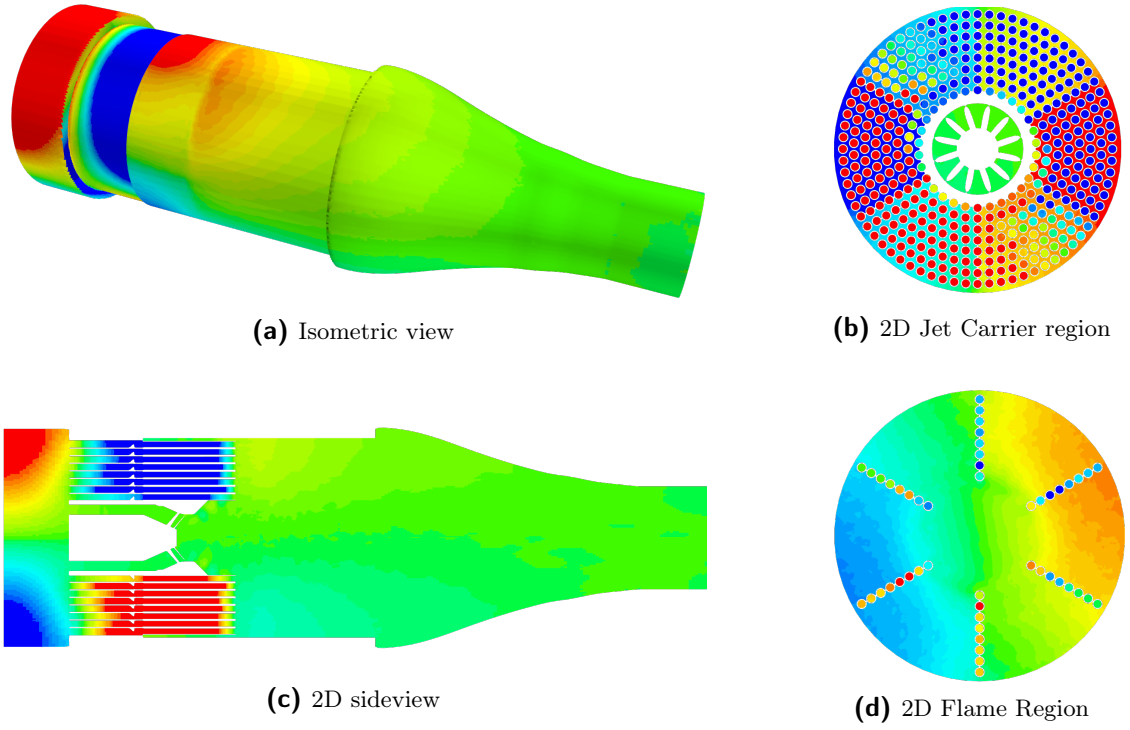

(a) Isometric view

(b) 2D Jet Carrier region

(c) 2D sideview

(d) 2D Flame Region

Figure A.14: S400 with Baffles 1260 Hz Acoustic Mode Shape

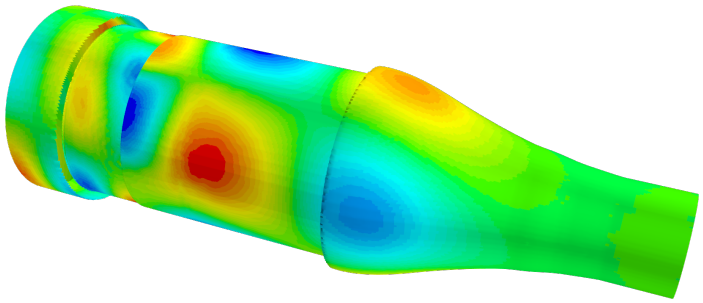

(a) Isometric view

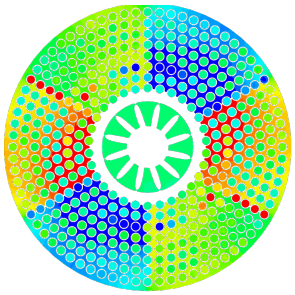

(b) 2D Jet Carrier region

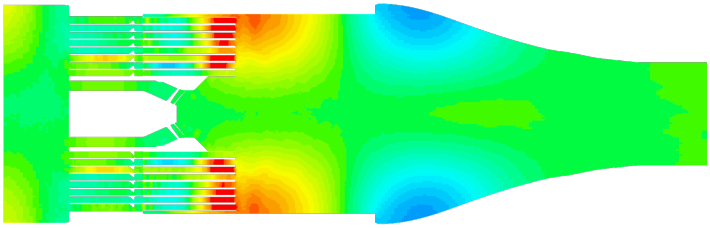

(c) 2D sideview

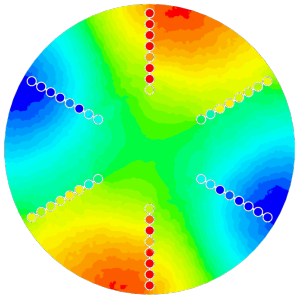

(d) 2D Flame Region

Figure A.15: S400 with Baffles 2550 Hz Mode Acoustic Mode Shape

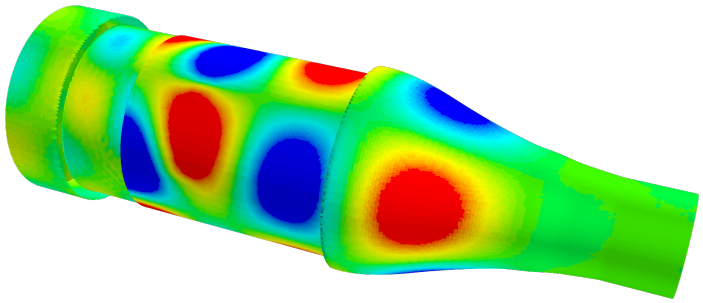

(a) Isometric view

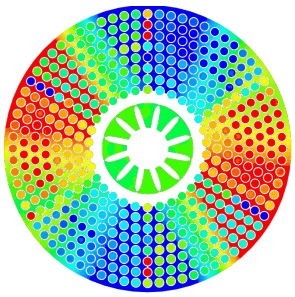

(b) 2D Jet Carrier region

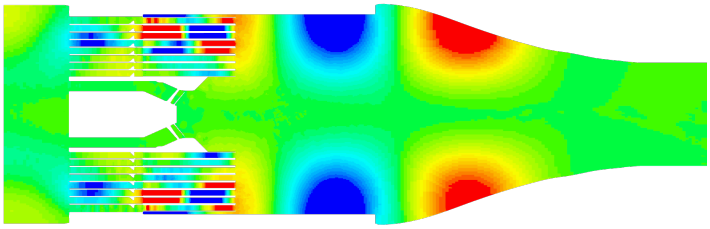

(c) 2D sideview

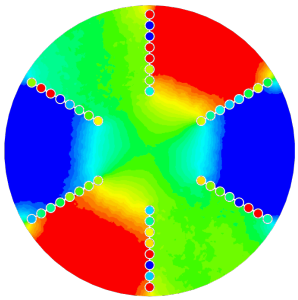

(d) 2D Flame Region

Figure A.16: S400 with Baffles 3050 Hz Mode Acoustic Mode Shape

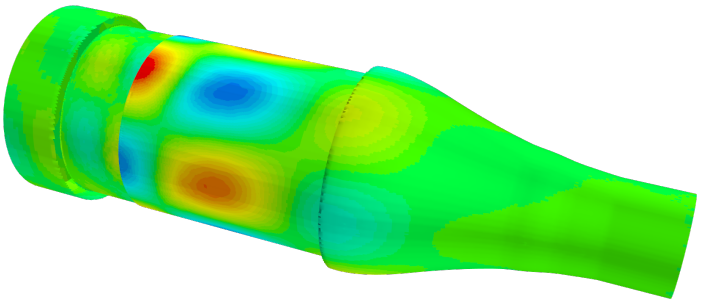

(a) Isometric view

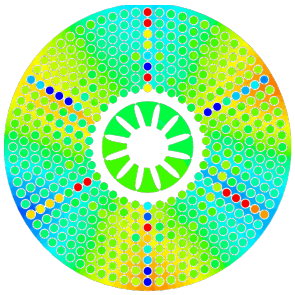

(b) 2D Jet Carrier region

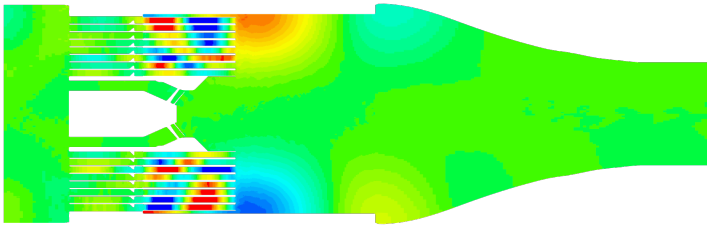

(c) 2D sideview

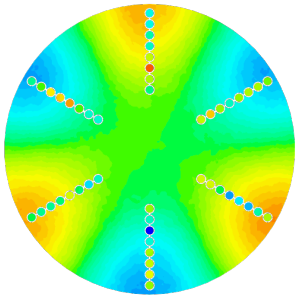

(d) 2D Flame Region

Figure A.17: S400 with Baffles 3450 Hz Mode Acoustic Mode Shape

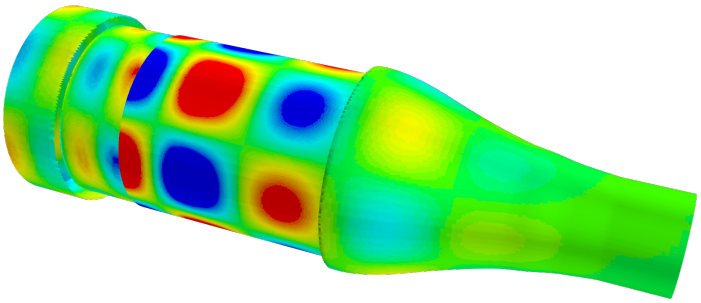

(a) Isometric view

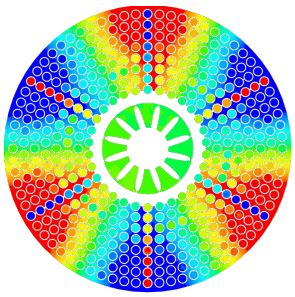

(b) 2D Jet Carrier region

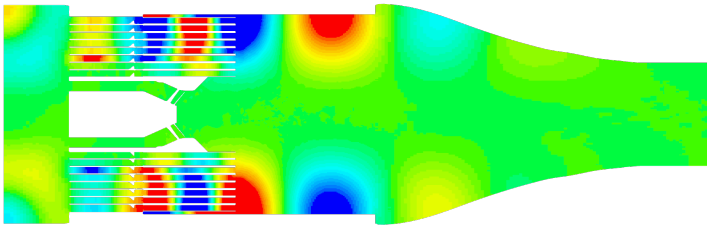

(c) 2D sideview

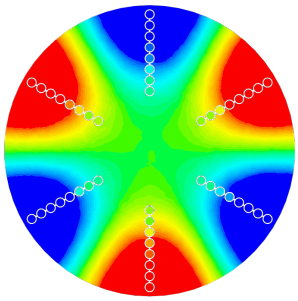

(d) 2D Flame Region

Figure A.18: S400 with Baffles 3850 Hz Mode Acoustic Mode Shape

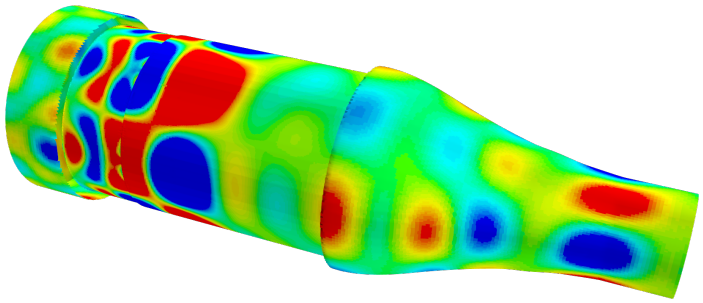

(a) Isometric view

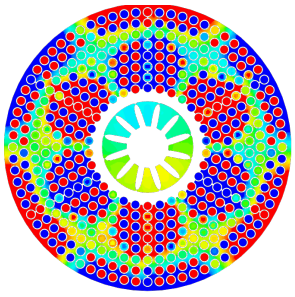

(b) 2D Jet Carrier region

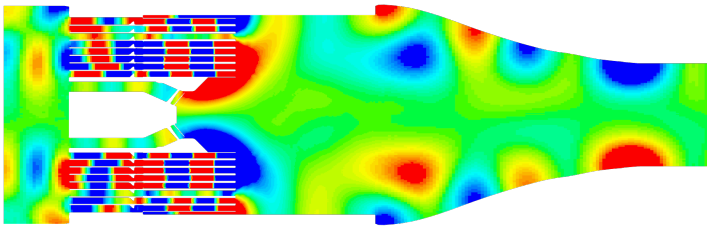

(c) 2D sideview

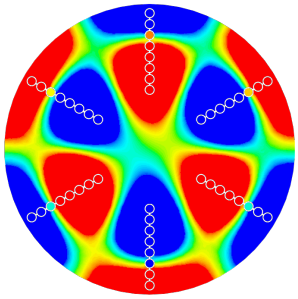

(d) 2D Flame Region

Figure A.19: S400 with Baffles 5850 Hz Mode Acoustic Mode Shape

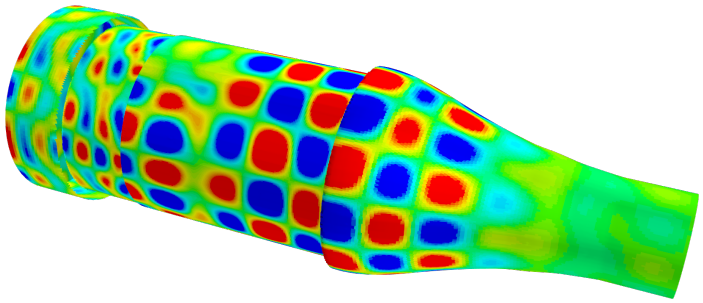

(a) Isometric view

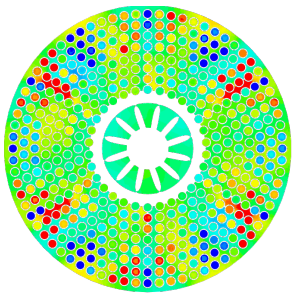

(b) 2D Jet Carrier region

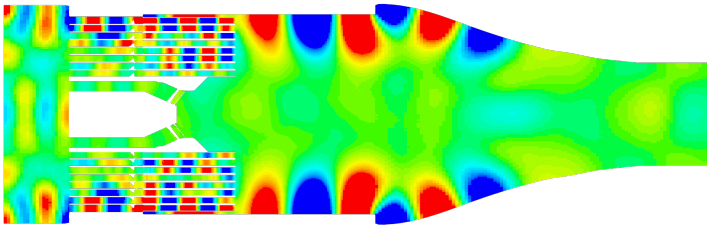

(c) 2D sideview

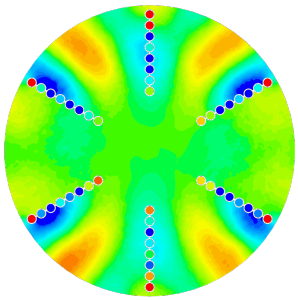

(d) 2D Flame Region

Figure A.20: S400 with Baffles 7650 Hz Mode Acoustic Mode Shape

Appendix B

Mean Fields S400 and Sample Case

B.1 Sample Case

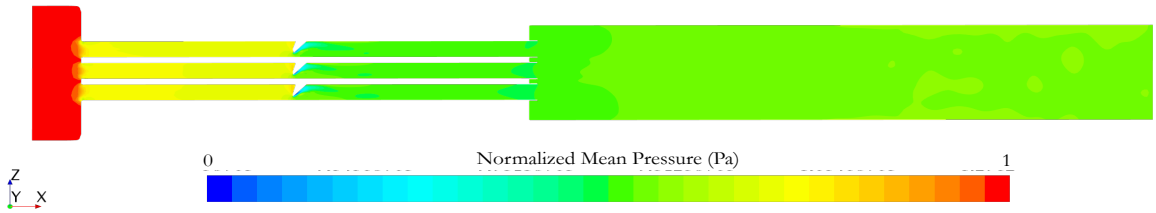

Figure B.1: Normalized Mean Pressure Sample Case

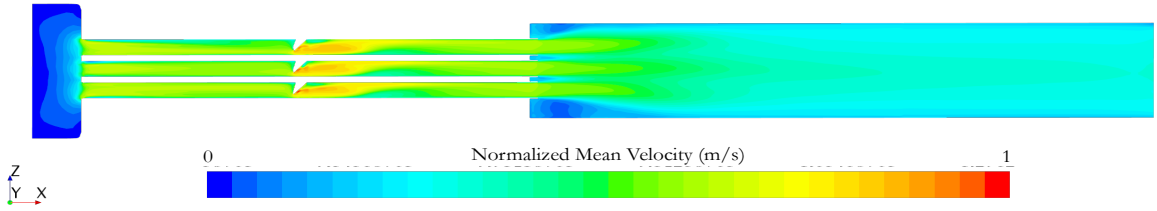

Figure B.2: Normalized Mean Velocity Sample Case

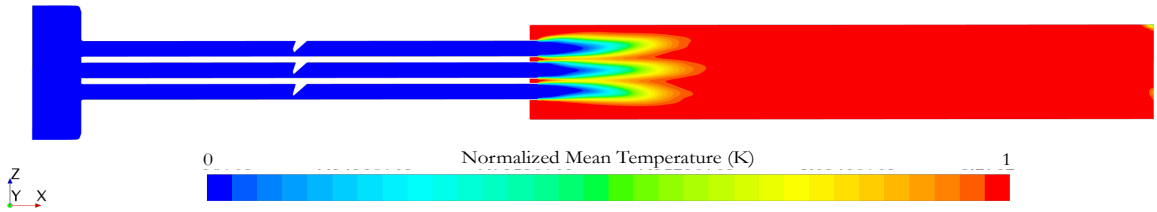

Figure B.3: Normalized Mean Temperature Sample Case

B.2 S400 without Baffles

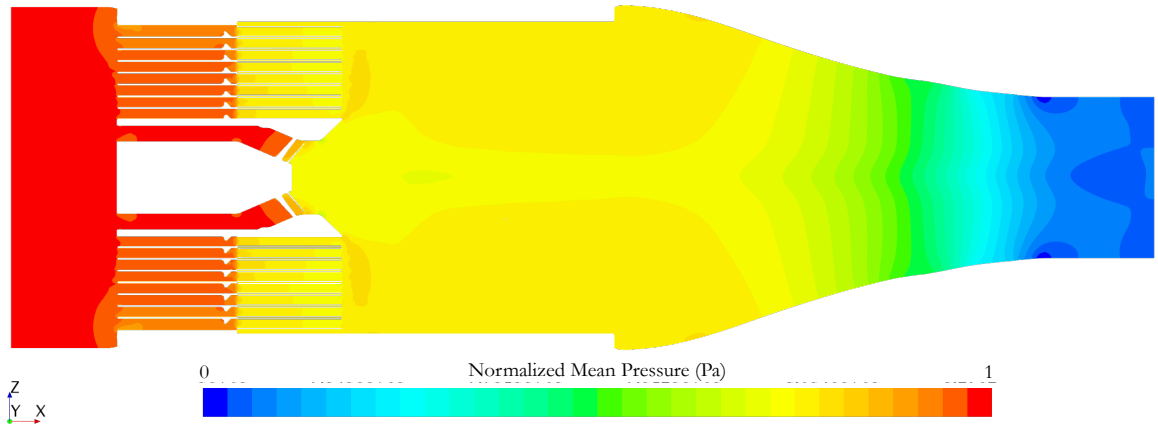

Figure B.4: Normalized Mean Pressure S400 without Baffles

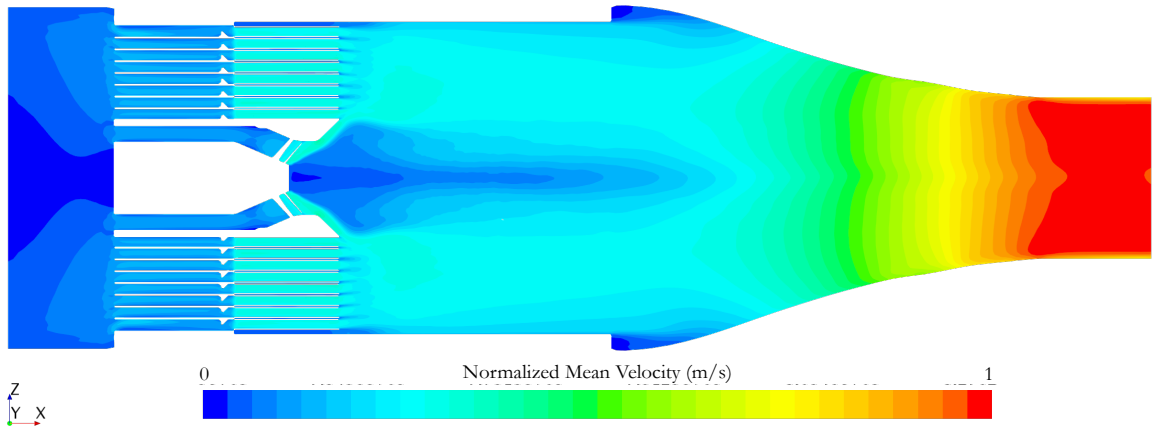

Figure B.5: Normalized Mean Velocity S400 without Baffles

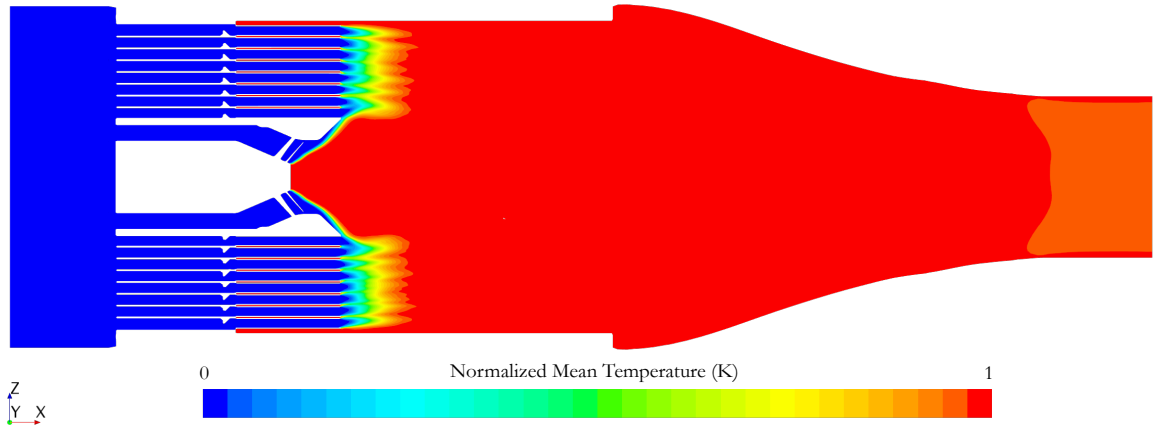

Figure B.6: Normalized Mean Temperature S400 without Baffles

B.3 S400 with Baffles

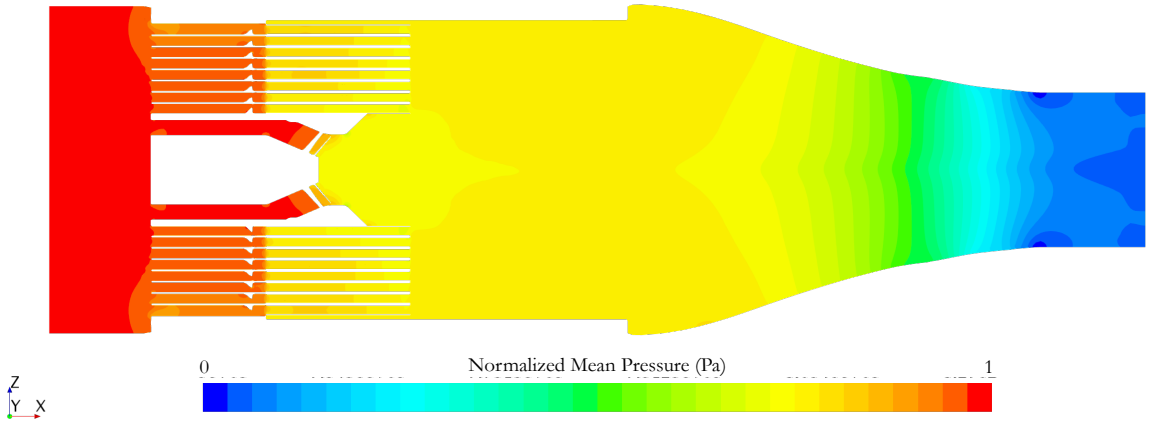

Figure B.7: Normalized Mean Pressure S400 with Baffles

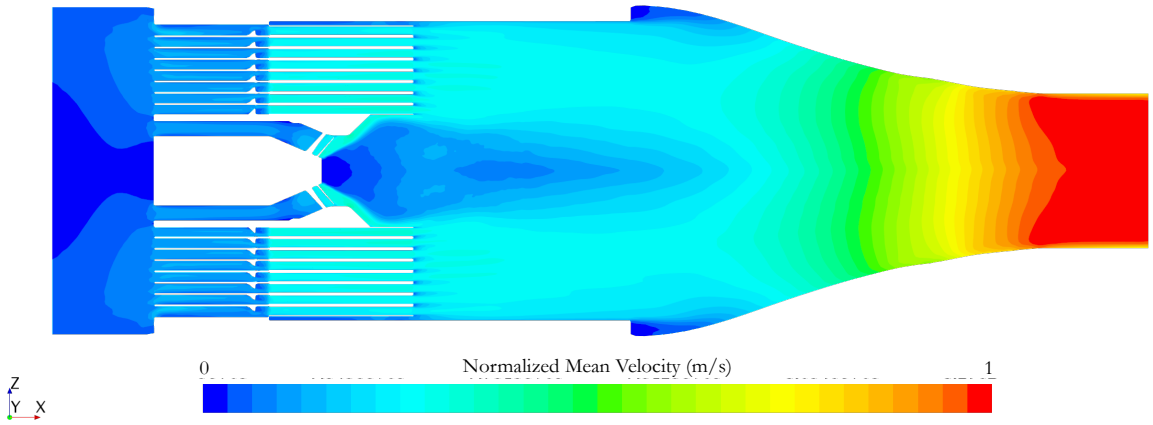

Figure B.8: Normalized Mean Velocity S400 with Baffles

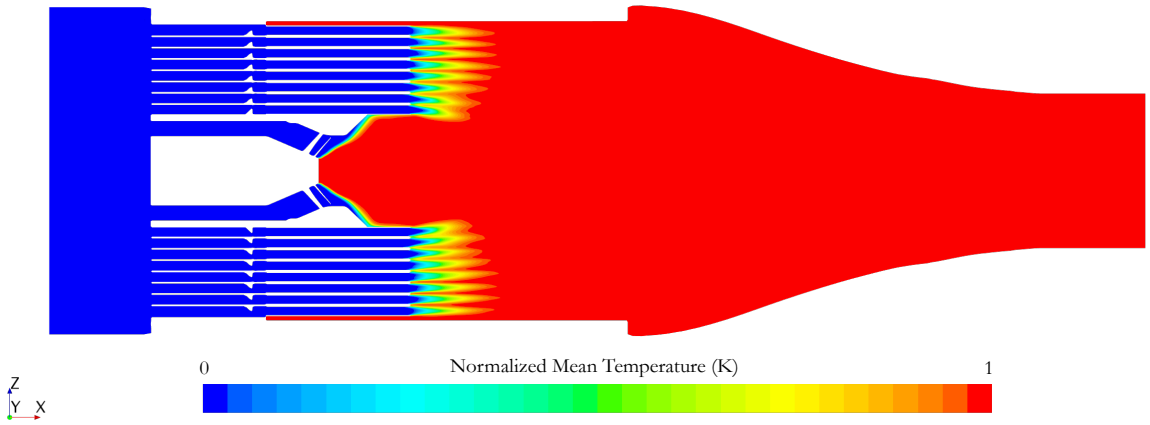

Figure B.9: Normalized Mean Temperature S400 with Baffles

Appendix C

Pre and Post Processing Techniques in StarCCM+

In this Appendix, the techniques used to gather the results derived in this thesis is explained in further detail, namely the pressure bomb and the heat release centre tracking. It is explained as a roadmap. While both techniques can also be used in OpenFOAM, they are explained for StarCCM+.

C.1 Pressure Bomb Sample Case

1. First make a RANS calculation for an initial setup.
2. Create a cellset at the position that must be pressure bombed.

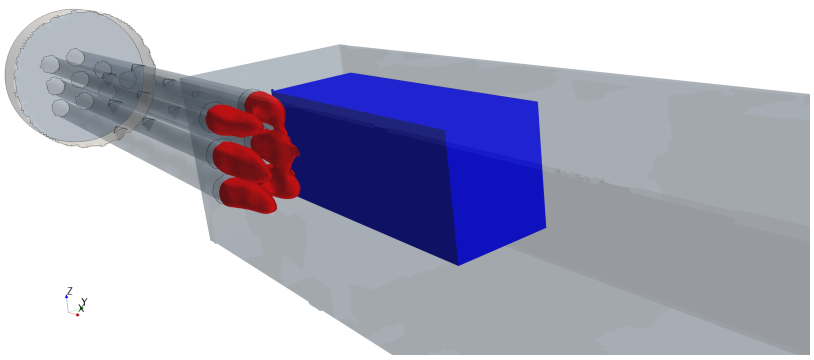

Figure C.1: In blue is the region where the pressure bomb is located. Red are the flames

3. Make a scalar field called Bomb (set dimension to pressure).

4. The definition should be: $\${Pressure}+\${CellSetVar_1}*3e5$, where $3e5$ is the amount of pressure for the bomb, can be artificially set to whatever is desired.
5. Create a Volume Data mapper, set source stencil to cell and target stencil to cell, do not forget to disable Update.
6. Map the scalar quantities: Bomb, Temperature, Mixture Fraction 0, Mixture Fraction Variance 0, Progress Variable and Pressure. The vector quantity: Velocity.
7. Right mouse click on the mapper, select Map Data.
8. Clear the current StarCCM+ solution.
9. Go to Continua, Physics 1, Initial Conditions, Initialize all quantities with the mapped quantities. Make sure to initialize pressure with MappedBomb and not MappedPressure.
10. Run your LES, observe if it remains stable, if not lower your pressure bomb pressure or decrease the volume of the pressure bomb.

C.2 Pressure Bomb S400

In the S400, the pressure bomb had to be in the jet carrier region, as previous studies pointed out that there is where the transverse modes are most active. Therefor, the bomb should not be in the jets, as that may cause longitudinal modes to be triggered. A solution is, to discriminate the bomb region with regard to temperature. Step 4 of the previous enumerating should then be:

$$\underbrace{\${Temperature} > T?}_{(1)}\underbrace{\${Pressure} + \${CellSetVar\_1} * 3e5}_{(2)}:\underbrace{\${Pressure}}_{(3)} \tag{C.1}$$

Where T is a temperature of choosing and $3e5$ is again the bomb pressure. The formulation uses ternary operators. It basically says, if the temperature is **not** higher than T (1), then the cells are cells in the bomb region (2), else they are not bomb region cells (3).

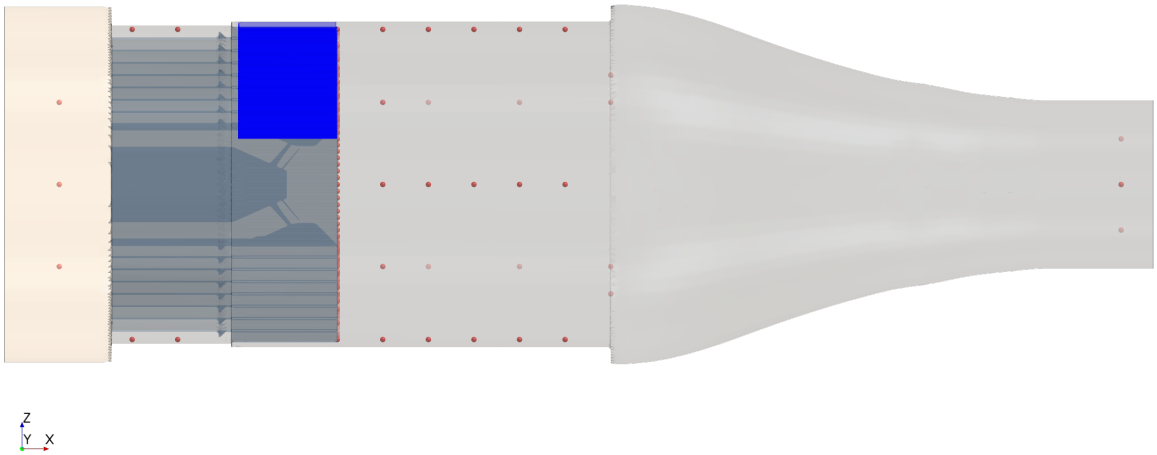

Figure C.2: Bomb location side view S400, the blue area is the bomb area

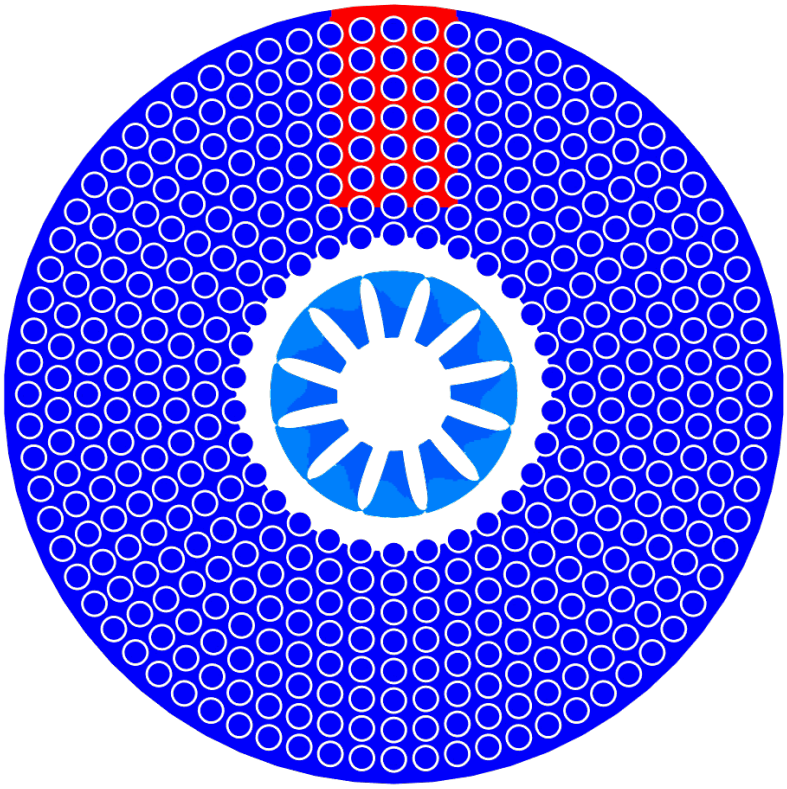

Figure C.3: Bomb front view S400, red indicates the bomb area

C.3 Passive Scalar Region Source

This appendix section covers how to implement a Passive Scalar in a volumetric domain. It is used to distinguish all the jets. So in every jet a passive scalar has to be implemented. Based on the passive scalar and ternary operators, the flames can be tracked more accurate. The roadmap is given below

1. Create a cell set where the passive scalar should be implemented.

2. Create a Field Function, name it PassiveScalarSource and set the dimensions to Mass/Time and the definition to $\${CellSetVar\_1\} * mF$. Where mF is an arbitrary mass flow.

3. Create a Threshold, set the scalar function to PassiveScalarSource and use the set above max option. There choose any super small number above 0 and make sure it is set to kg/s.

4. Create a Sum Report, set the field function to Volume and the part to sum over is the Threshold from step 3.

5. Make a new Field Function, name it PassiveScalarSource-Normalized. Set the dimension to Mass/Time. The definition should be $\${PassiveScalarSource\}/\${SumReport\}$.

6. Create a new Passive Scalar at Continua - Models and set it to convection only.

7. In Region - Fluid 1 - Passive Scalar Source option set it to Mass Flux and the Passive Scalar Source has to be set to PassiveScalarSource-Normalized.

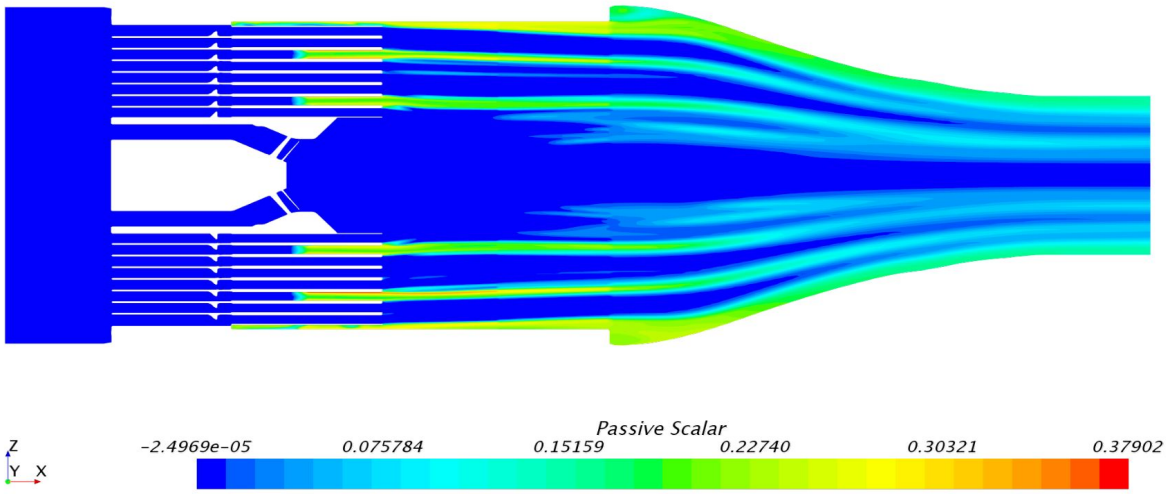

Figure C.4: Passive Scalar Injected in the S400

C.4 Conditional Heat Release

Now, in order to track the centre of heat release, the passive scalars as previously discusses must be implemented and here, the derivation is then given.

1. Make a new Field Function, with definition (\${$PassiveScalar$} > 0.01?\${$ChemistryHeatReleaseIndicator$} : 0).
2. Create a cell set which contains the flame region, make it slightly larger to also cover flame displacements.
3. Create a Threshold, set $CellSetVar\_1$ as the scalar and use above max. Set it to any positive value.
4. Make a new Field Function, name it for example $Heat\_Release\_Conditional\_Flame\_1$ for the first flame, give it definition \${$CellSetVar\_2$} ∗ \${$FieldFunctionFromStep1$}
5. Now the x,y and z component have to be tracked separately. This can be done by making a new field function for each flame and each component. The name could be Heat-Release-Conditional-Flame-Centre-X-1, where X is the direction and 1 the flame. The definition for this flame should then be \$\${$Centroid$}[0] ∗ (\$$Heat - Release - Conditional - Flame - 1$}) Replace the 0 by 1 or 2 to gain the y and z component.
6. Create Integration Reports for the Field Functions from step 4 and 5. For the Field Function from step 5, the Threshold that has been created in step 3 can be selected as part, to speed up the computational process.
7. Very important, do not forget to create **monitors** of all the Reports, else the quantities are not written

Based on the formula

$$q_{centre} = \frac{\int_V \vec{x} \cdot q dV}{\int_V q dV} \tag{C.2}$$

Everything can be divided afterwards and the centre of heat release components are the result.

Appendix D

Flame motion S400

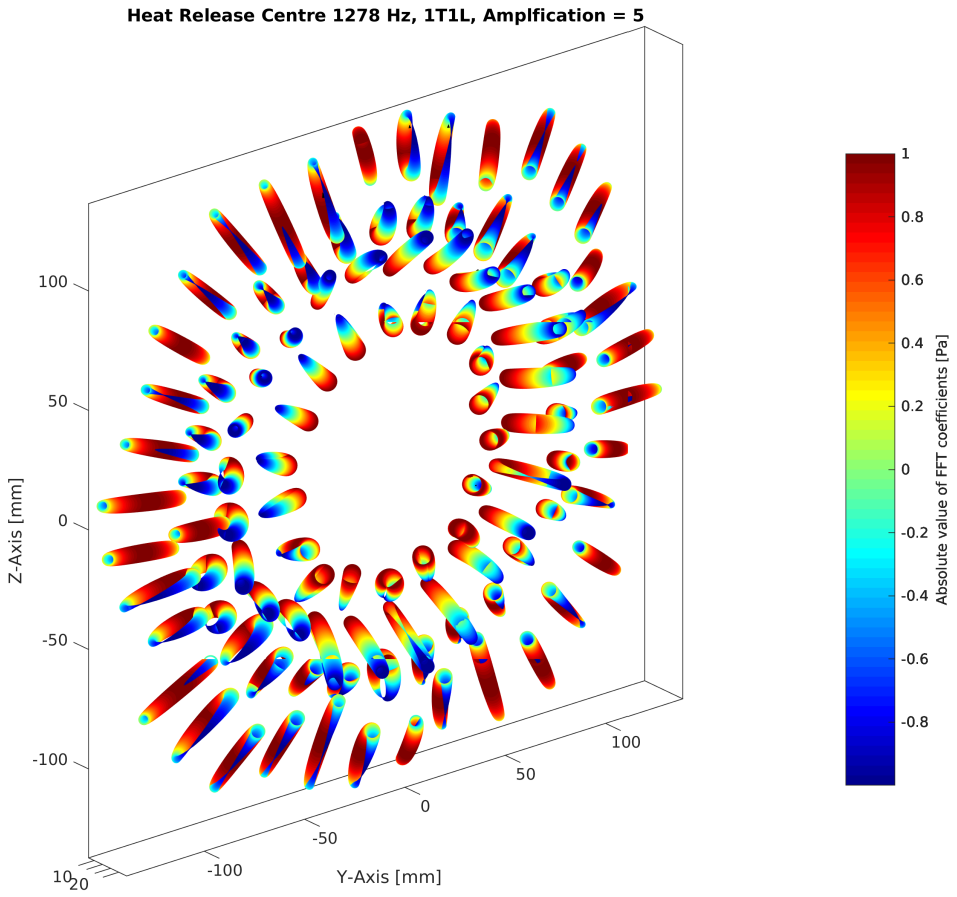

Figure D.1: S400 without baffles heat release movement for the 1T1L

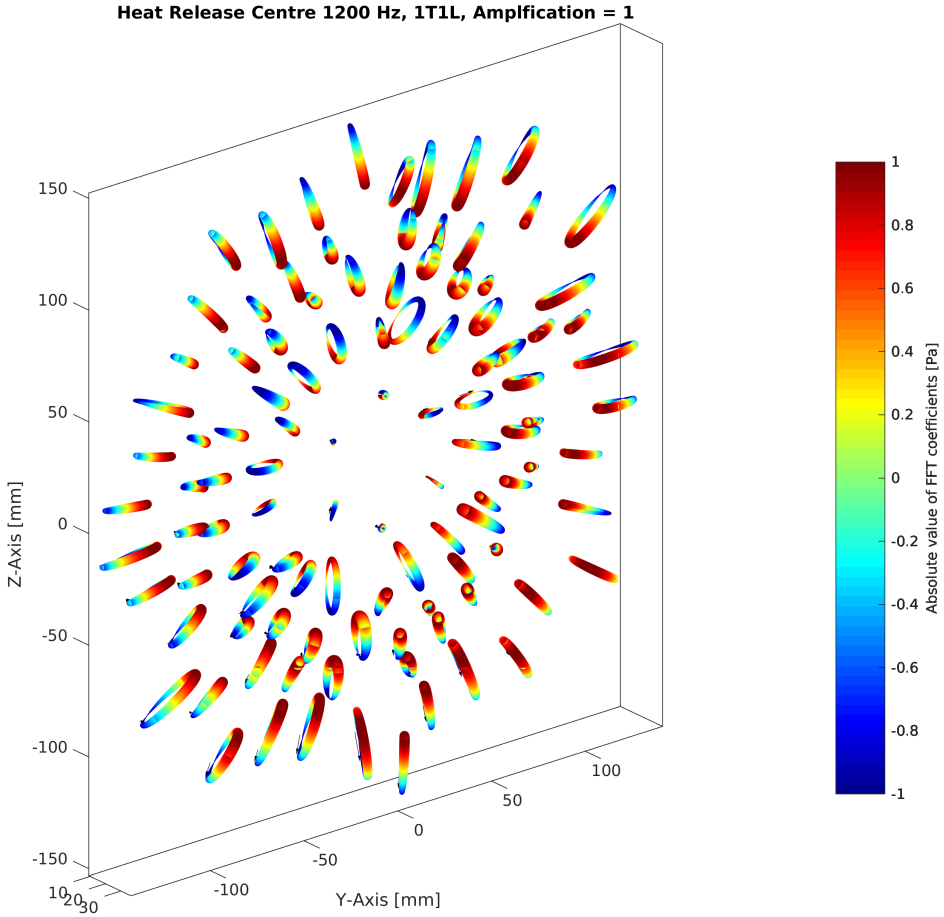

Figure D.2: S400 with baffles heat release movement for the 1T1L

Figure D.1 and Figure D.2 visualise the heat release centre motion for the 1T1L of respectively the S400 without and with baffles. It can be observed that the outer flames in both configurations move in transverse direction, while the inner flames seem to move less. It must be noted here that the acoustic wave is not standing, but rotating.
Why do the outer flames move in transverse direction and not the inner flames such as in section 4.5? The large pilot flame in the centre burns everything that comes near and also rotates with the acoustic mode. The flames on the inside are burned faster by the rotating pilot flame. This local increase in heat release burns their neighbouring flames faster. This goes on till the last row of flames, which have unoccupied space in the direction of the wall. The next pictures give some more insight in the flame motion. They represent the temperature field of the baffled S400, when only the 1T1L was active in the system.

Based on D.3, it seems plausible that the post processing technique, described in Appendix C fails for the inner flames, due to the fact that the pilot flame overlaps with them.

Figure D.4 shows that flames oscillate in longitudinal direction under the influence of high and low pressure, which is in line with the observations in section 4.4.

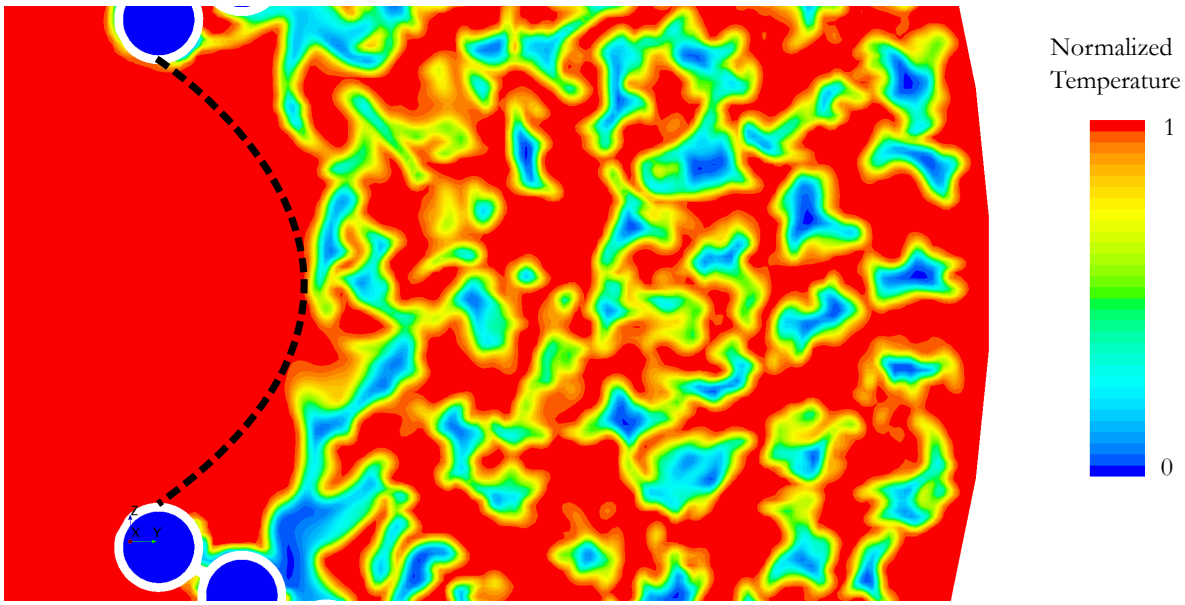

(a) Pilot flame reaching far in the baffle compartment

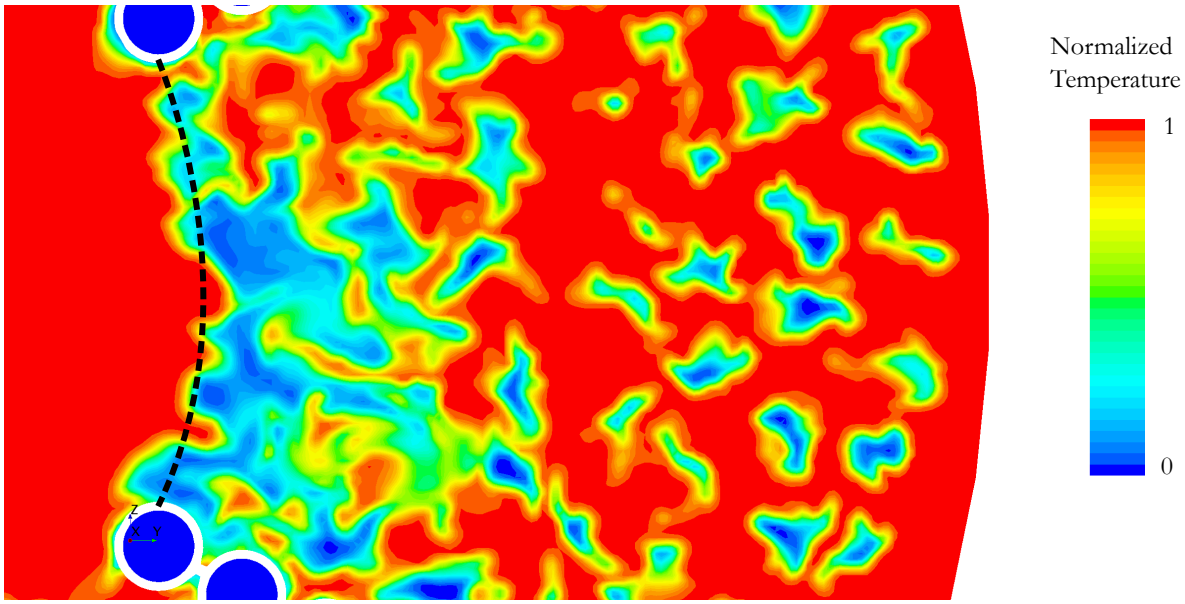

(a) Pilot flame retreated to the centre

Figure D.3: The pilot flame, noted by the black dotted line, reaching in and out the baffle compartments. The cut is made in the YZ-plane and exactly at the end of elongated ducts.

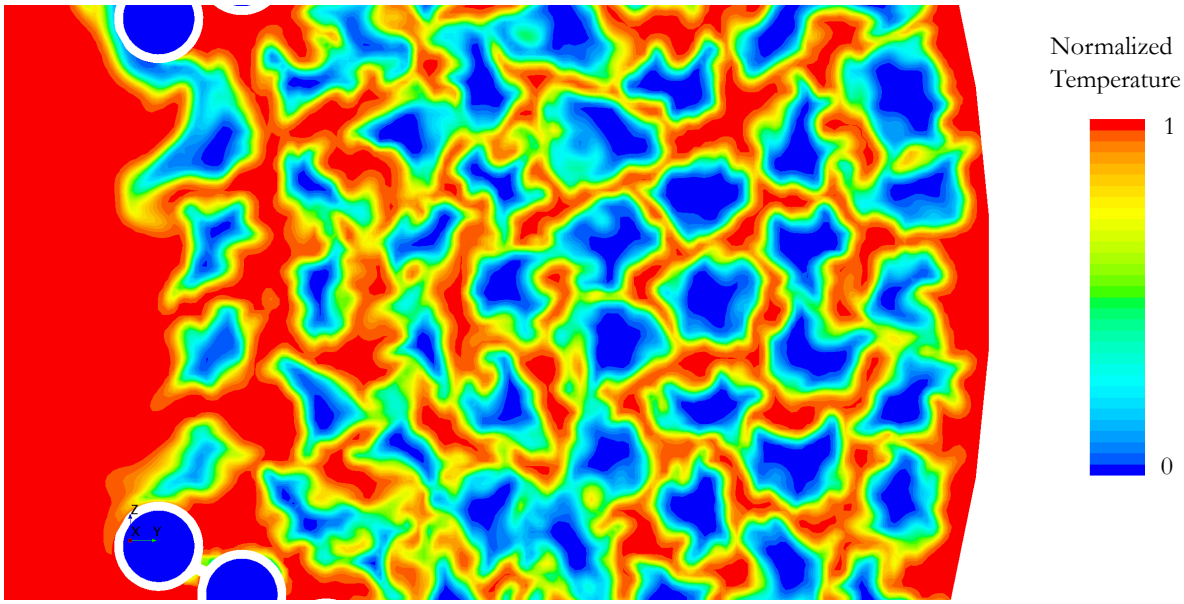

(a) Flames under influence of low pressure in the region

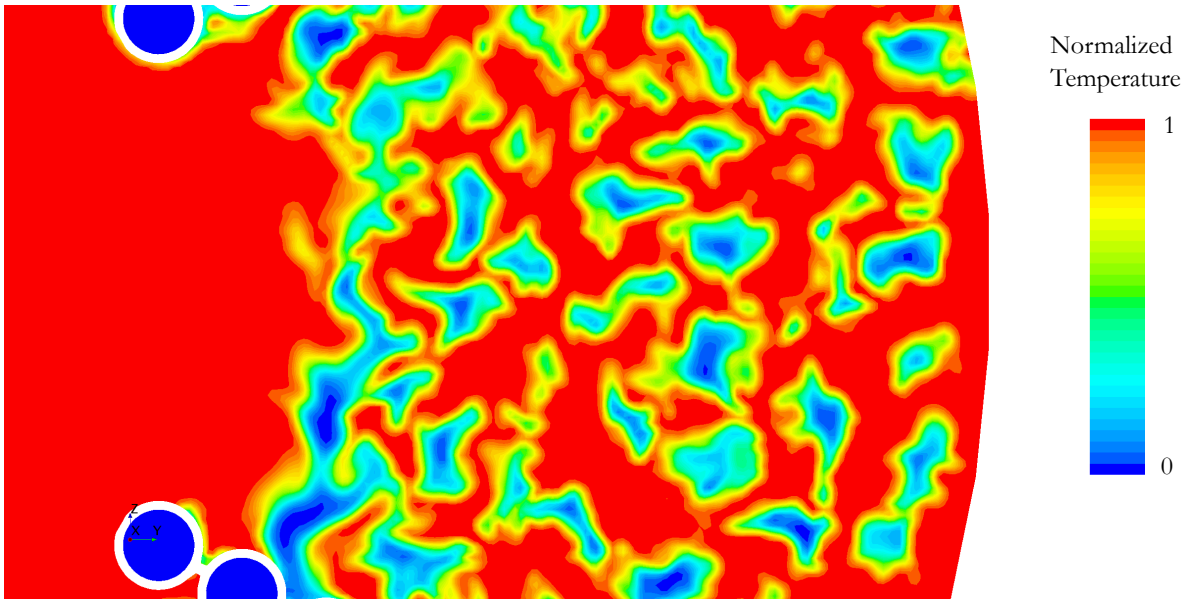

(b) Flames under the influence of high pressure in the region

Figure D.4: The temperature field under the influence of high and lower pressure in the baffle compartments.

Bibliography

[1] U. Energy Information Administration, *International Energy Outlook 2018 (IEO2018),* Csis **2018**, 21 (2018).

[2] National Energy Technology Laboratory (NETL), *Cost and performance baseline for fossil energy plants, Volume 1: Bituminous coal and natural gas to electricity.* Journal of Philosophical Logic , 6657 (2010).

[3] M. A. Gonzalez-Salazar, T. Kirsten, and L. Prchlik, *Review of the operational flexibility and emissions of gas- and coal-fired power plants in a future with growing renewables,* Renewable and Sustainable Energy Reviews **82**, 1497 (2018).

[4] European Environment Agency, *Nitrogen oxides (NOx) emissions,* (2010).

[5] W. R. Bender, *Lean Pre-mixed Combustion,* NETL Gas Turbine Handbook , 217 (2006).

[6] SIEMENS, *SGT5-9000HL heavy duty gas turbine (50Hz),* (2018).

[7] A. P Dowling, *The challenges of lean premixed combustion,* (2018).

[8] T. C. Lieuwen and V. Yang, *Combustion instabilities in gas turbine engines : operational experience, fundamental mechanisms and modeling,* , 657 (2005).

[9] S. Candel, *Combustion dynamics and control: Progress and challenges,* Proceedings of the Combustion Institute **29**, 1 (2002).

[10] S. Candel, D. Durox, T. Schuller, P. Palies, J.-f. Bourgouin, and J. P. Moeck, *Progress and challenges in swirling flame dynamics,* Comptes Rendus Mecanique **340**, 758 (2012).

[11] T. Poinsot, *Prediction and control of combustion instabilities in real engines,* Proceedings of the Combustion Institute **36**, 1 (2017).

[12] A. P. Dowling, *The challenges of lean premixed combustion,* Gt-2003 (2003).

[13] J. Schwing, T. Sattelmayer, and N. Noiray, *Interaction Of Vortex Shedding And Transverse High-Frequency Pressure Oscillations In A Tubular Combustion Chamber,* , 1 (2016).

[14] J. Schwing and T. Sattelmayer, *High-Frequency Instabilities In Cylindrical Flame Tubes: Feedback Mechanism And Damping,* (2016).

[15] Y. Huang and V. Yang, *Dynamics and stability of lean-premixed swirl-stabilized combustion,* Progress in Energy and Combustion Science **35**, 293 (2009).

[16] D. T. Harje and F. H. Reardon, *Liquid Propellant Rocket Combustion Instability,* NASA SP-194 **00**, 1 (1972).

[17] NASA, *Liquid Rocket Engine Combustion Stabilization Devices,* (1974).

[18] M. Bauerheim, *Etudes théorique et numérique des effets de brisures de symétrie sur les modes thermo-acoustiques azimutaux dans les chambres annulaires,* (2014), 10.1088/0953-8984/28/25/253001.

[19] J. O'Connor, V. Acharya, and T. Lieuwen, *Transverse combustion instabilities: Acoustic, fluid mechanic, and flame processes,* Progress in Energy and Combustion Science **49**, 1 (2015).

[20] N. Noiray and B. Schuermans, *On the dynamic nature of azimuthal thermoacoustic modes in annular gas turbine combustion chambers,* Proceedings of the Royal Society A **469**, 20120535 (2013).

[21] G. Ghirardo and M. P. Juniper, *Stability of spinning and standing azimuthal modes in symmetric annular chambers : model for transversal forcing,* Int'l Summer School and Workshop on Non-Normal and Nonlinear effects in Aero- and Thermoacoustics (2013).

[22] J. A. Van Oijen, F. A. Lammers, and L. P. De Goey, *Modeling of complex premixed burner systems by using flamelet-generated manifolds,* Combustion and Flame **127**, 2124 (2001).

[23] T. Poinsot and D. Veynante, *Combustion and Flame*, 2nd ed. (2005) p. 534.

[24] J. van Oijen, *Flamelet-Generated Manifolds : Development and Application to Premixed Laminar Flames,* , 125 (2002).

[25] S. Klein, *On the acoustics of turbulent non-premixed flames*, Ph.D. thesis (2000).

[26] M. Lighthill, *On sound generated aerodynamically II. Turbulence as a source of sound,* **222** (1954).

[27] P. Wolf, G. Staffelbach, A. Roux, L. Gicquel, T. Poinsot, and V. Moureau, *Massively parallel LES of azimuthal thermo-acoustic instabilities in annular gas turbines,* Comptes Rendus - Mecanique **337**, 385 (2009).

[28] Stephen B. Pope, *Turbelent Flows* (2000).

[29] F. T. Nieuwstadt, B. J. Boersma, and J. Westerweel, *Turbulence* (Springer, 2016).

[30] J. Smagorinsky, *General Circulation Experiments With the Primitive Equations,* Monthly Weather Review **91**, 99 (1963).

[31] D. H. Kim, K. S. Yang, and M. Senda, *Large eddy simulation of turbulent flow past a square cylinder confined in a channel,* Computers and Fluids **33**, 81 (2004).

[32] F. Ducros, F. Nicoud, and T. Poinsot, *Wall-adapting local eddy-viscosity models for simulations in complex geometries,* Conference on Numerical Methods in Fluid Dynamics , 1 (1998).

[33] S. Huang and Q. Li, *A new dynamic one-equation subgrid-scale model for large eddy simulations,* International Journal for Numerical Methods in Engineering (2010).

[34] F. Nicoud and F. Ducros, *Subgrid-scale stress modelling based on the square of the velocity gradient tensor,* Flow, Turbulence and Combustion (1999).

[35] N. Ben-Cheikh, F. Hammami, A. Campo, and B. Ben-Beya, *A dynamic sub-grid scale model for large eddy simulation of turbulent flows in a lid-driven cubical cavity,* Comptes Rendus - Mecanique **340**, 721 (2012).

[36] D. Veynante and T. Poinsot, *Large eddy simulation of combustion instabilities in turbulent premixed burners,* Center for Turbulenc Research Annual Research Briefs , 253 (1997).

[37] C. Angelberger, D. Veynante, F. N. Egolfopoulos, and T. Poinsot, *Large eddy simulations of combustion instabilities in premixed flames,* Proceedings of the Summer Program, Center for Turbulence Research , 61 (1998).

[38] A. Ghani, T. Poinsot, L. Gicquel, and G. Staffelbach, *LES of longitudinal and transverse self-excited combustion instabilities in a bluff-body stabilized turbulent premixed flame,* Combustion and Flame **162**, 4075 (2015).

[39] P. Wolf, G. Staffelbach, L. Y. Gicquel, J. D. Müller, and T. Poinsot, *Acoustic and Large Eddy Simulation studies of azimuthal modes in annular combustion chambers,* Combustion and Flame **159**, 3398 (2012).

[40] N. Peters and F. A. Williams, *The asymptotic structure of stoichiometric methaneair flames,* Combustion and Flame **68**, 185 (1987).

[41] N. Peters, *Laminar flamelet concepts in turbulent combustion,* Symposium (International) on Combustion **21**, 1231 (1988).

[42] R. Borghi, *Turbulent combustion modelling,* Progress in Energy and Combustion Science **14**, 245 (1988).

[43] J. A. van Oijen, A. Donini, R. J. Bastiaans, J. H. ten Thije Boonkkamp, and L. P. de Goey, *State-of-the-art in premixed combustion modeling using flamelet generated manifolds,* Progress in Energy and Combustion Science **57**, 30 (2016).

[44] E. Knudsen and H. Pitsch, *Large-Eddy Simulation for Combustion Systems: Modeling Approaches for Partially Premixed Flows,* The Open Thermodynamics Journal **4**, 76 (2010).

[45] J. V. OIJEN and L. D. GOEY, *Modelling of Premixed Laminar Flames using Flamelet-Generated Manifolds,* Combustion Science and Technology **161**, 113 (2000).

[46] O. Colin, F. Ducros, D. Veynante, and T. Poinsot, *A thickened flame model for large eddy simulations of turbulent premixed combustion,* Physics of Fluids **12**, 1843 (2000).

[47] F. L. Sacomano Filho, G. Kuenne, M. Chrigui, A. Sadiki, and J. Janicka, *A consistent Artificially Thickened Flame approach for spray combustion using LES and the FGM chemistry reduction method: Validation in Lean Partially Pre-vaporized flames,* Combustion and Flame **184**, 68 (2017).

[48] G. Kuenne, A. Ketelheun, and J. Janicka, *LES modeling of premixed combustion using a thickened flame approach coupled with FGM tabulated chemistry,* Combustion and Flame **158**, 1750 (2011).

[49] V. L. Zimont and A. N. Lipatnikov, *A numerical model of premixed turbulent combustion of gases,* **14**, 993 (1995).

[50] V. Zimont, W. Polifke, M. Bettelini, and W. Weisenstein, *An Efficient Computational Model for Premixed Turbulent Combustion at High Reynolds Numbers Based on a Turbulent Flame Speed Closure,* Journal of Engineering for Gas Turbines and Power **120**, 526 (1998).

[51] P. Flohr and H. Pitsch, *A turbulent flame speed closure model for LES of industrial burner flows,* Center for Turbulence Research Proceedings of the Summer Program , 169 (2000).

[52] F. Zhang, P. Habisreuther, M. Hettel, and H. Bockhorn, *Modelling of a premixed swirl-Stabilized flame using a turbulent flame speed closure model in les,* Flow, Turbulence and Combustion **82**, 537 (2009).

[53] T. D. Butler and P. J. O'Rourke, *A numerical method for two dimensional unsteady reacting flows,* Symposium (International) on Combustion **16**, 1503 (1977).

[54] F. Charlette, D. Veynante, and C. Meneveau, *A power-law wrinkling model for LES of premixed turbulent combustion: Part I - non-dynamic formulation and initial tests,* \Cf **131**, 159 (2002).

[55] A. Hosseinzadeh, A. Sadiki, and J. Janicka, *Assessment of the Dynamic SGS Wrinkling Combustion Modeling Using the Thickened Flame Approach Coupled with FGM Tabulated Detailed Chemistry,* Flow, Turbulence and Combustion **96**, 939 (2016).

[56] H. Pitsch, *A Consistent Level Set Formulation for Large-Eddy Simulation of Premixed Turbulent Combustion,* Global and Planetary Change **6**, 1 (2005).

[57] T. Poinsot, P. Wolf, G. Staffelbach, L. Y. M. Gicquel, and J. D. Muller, *Identification of azimuthal modes in annular combustion chambers,* Annual research briefs. Center for Turbulence Research. , 249 (2011).

[58] G. Staffelbach, L. Y. Gicquel, G. Boudier, and T. Poinsot, *Large Eddy Simulation of self excited azimuthal modes in annular combustors,* Proceedings of the Combustion Institute **32 II**, 2909 (2009).

[59] I. S. Park, C. H. Sohn, and H. J. Kim, *Acoustic damping enhanced by gaps in baffled injectors in an acoustic chamber,* Journal of Sound and Vibration **330**, 2747 (2011).

[60] C. F. Silva, T. Emmert, S. Jaensch, and W. Polifke, *Numerical study on intrinsic thermoacoustic instability of a laminar premixed flame,* Combustion and Flame **162**, 3370 (2015).

[61] H. Krediet, *Prediction Of Limit Cycle Pressure Oscillations In Gas Turbine Combustion Systems Using The Flame Describing Function*, Ph.D. thesis (2012).

[62] F. Di Sabatino, T. F. Guiberti, W. R. Boyette, W. L. Roberts, J. P. Moeck, and D. A. Lacoste, *Effect of pressure on the transfer functions of premixed methane and propane swirl flames,* Combustion and Flame **193**, 272 (2018).

[63] C. Kraus, L. Selle, and T. Poinsot, *Coupling heat transfer and large eddy simulation for combustion instability prediction in a swirl burner,* Combustion and Flame **191**, 239 (2018).

[64] J. Yoon, S. Joo, J. Kim, M. C. Lee, J. G. Lee, and Y. Yoon, *Effects of convection time on the high harmonic combustion instability in a partially premixed combustor,* Proceedings of the Combustion Institute **36**, 3753 (2017).

[65] M. Möser, *Technische Akustik* (Springer, 2015).

[66] K. Prieur, D. Durox, J. Beaunier, T. Schuller, and S. Candel, *Ignition dynamics in an annular combustor for liquid spray and premixed gaseous injection,* Proceedings of the Combustion Institute **36**, 3717 (2017).

[67] D. Blackstock, *Fundamentals of physical acoustics* (2000).

[68] D. Laera, G. Campa, S. M. Camporeale, E. Bertolotto, S. Rizzo, F. Bonzani, A. Ferrante, and A. Saponaro, *Modelling of thermoacoustic combustion instabilities phenomena: Application to an experimental test rig,* Energy Procedia **45**, 1392 (2014).

[69] M. Bauerheim, P. Salas, F. Nicoud, and T. Poinsot, *Symmetry breaking of azimuthal thermo-acoustic modes in annular cavities: A theoretical study,* Journal of Fluid Mechanics **760**, 431 (2014).

[70] K. Wieczorek, *Numerical Study of Mach Number Effects on Combustion Instability,* Entropy (2010).

[71] B. Rayleigh, *The Explanation of Certain Acoustical Phenomena,* Nature **18**, 319 (1878), arXiv:arXiv:1011.1669v3 .

[72] Martin Summerfield, *A Theory of Unstable Combustion in Liquid Propellant Rocket Systems,* (1951).

[73] L. Crocco and S.-I. Cheng, *Theory of Combustion Instability in Liquid Propellant Rocket Motors*, January (Butterwvortiis Scientific Publiciations, 1956) pp. 1–7.

[74] T. Lieuwen and B. T. Zinn, *The role of equivalence ratio oscillations in driving combustion instabilities in low NOxgas turbines,* Symposium (International) on Combustion **27**, 1809 (1998).

[75] C. M. Coats, *Coherent structures in combustion,* Progress in Energy and Combustion Science **22**, 427 (1996).

[76] S. Candel, *Combustion instablities coupled by pressure waves and their active control,* Twenty fourth symposium on combustion/The combustion institute , 1277 (1992).

[77] M. Hoeijmakers, V. Kornilov, I. Lopez Arteaga, P. de Goey, and H. Nijmeijer, *Intrinsic instability of flame-acoustic coupling,* Combustion and Flame **161**, 2860 (2014).

[78] T. Emmert, S. Bomberg, and W. Polifke, *Intrinsic thermoacoustic instability of premixed flames,* Combustion and Flame **162**, 75 (2015).

[79] E. Courtine, L. Selle, and T. Poinsot, *DNS of Intrinsic ThermoAcoustic modes in laminar premixed flames,* Combustion and Flame **162**, 4331 (2015).

[80] F. M. Berger, B. Schuermans, and T. Sattelmayer, *Swirl-Stabilized Gas Turbine Combustors Part One : Experimental Investigation of Local Flame Response,* Proceedings of ASME Turbo Expo 2016 , 1 (2016).

[81] T. Hummel, F. Berger, M. Hertweck, B. Schuermans, and T. Sattelmayer, *Swirl-Stabilized Gas Turbine Combustors Part Two : Modeling and Analysis,* Proceedings of ASME Turbo Expo 2016 , 1 (2016).

[82] A. P. Dowling and S. Hubbard, *Instability in lean premixed combustors,* Proceedings of the Institution of Mechanical Engineers, Part A: Journal of Power and Energy **214**, 317 (2000).

[83] J. Lepers, W. Krebs, B. Prade, P. Flohr, G. Pollarolo, and A. Ferrante, *Investigation of Thermoacoustic Stability Limits of an Annular Gas Turbine Combustor Test-Rig With and Without Helmholtz-Resonators,* Volume 2: Turbo Expo 2005 , 177 (2005).

[84] A. Hoffmann, Stefan & Weber, Gerd & Judith, H & Hermann, Jakob & Orthmann, *Application of Active Combustion Control to Siemens Heavy Duty Gas Turbines,* (1998).

[85] F. E. C. Culick, *Technology*, Vol. 323 (2006) pp. 1–664.

[86] I.-s. Park, C. H. Sohn, and N. Methods, *A Numerical Study on Acoustic Damping Mechanism of Baffled-Injectors in an Acoustic Chamber,* , 1 (2010).

[87] H. von Helmholtz, *On the sensations of tone as a physiological basis for the theory of music* (1895).

[88] H. J. Kim, J. Cha, J. Song, and Y. S. Ko, *Geometric and number effect on damping capacity of Helmholtz resonators in a model chamber,* Journal of Sound and Vibration **329**, 3266 (2010).

[89] B. Ćosić, D. Wassmer, S. Terhaar, and C. O. Paschereit, *Acoustic response of Helmholtz dampers in the presence of hot grazing flow,* Journal of Sound and Vibration **335**, 1 (2015).

[90] I. D. J. Dupere and A. P. Dowling, *The use of Helmholtz Resonators in a Practical Combustor,* (2003).

[91] I. S. Park and C. H. Sohn, *Nonlinear acoustic damping induced by a half-wave resonator in an acoustic chamber,* Aerospace Science and Technology **14**, 442 (2010).

[92] C. H. Sohn and J. H. Park, *A comparative study on acoustic damping induced by half-wave , quarter-wave , and Helmholtz resonators,* Aerospace Science and Technology **15**, 606 (2011).

[93] K. J. Lee, H. J. Kim, S. Seo, and H. S. Choi, *Experimental Verification for Acoustic Damping Enhancement by Gaps in Injector-Formed Baffles,* Journal of Propulsion and Power **25**, 435 (2009).

[94] S. J. Feng, W. S. Nie, B. He, and F. C. Zhuang, *Control Effects of Baffle on Combustion Instability in a LOX/GH(2) Rocket Engine,* Journal of Spacecraft and Rockets **47**, 419 (2010).

[95] T. Indlekofer, *Evaluation of StarCCM+ to Predict Thermoacoustic Instabilties Using Large Eddy Simulation*, Tech. Rep. (2017).

[96] D. Goeb, *Development of a CFD Strategy for the Assessment of Thermoacoustic Instabilities in a Gas Turbine Combustion System*, Tech. Rep. (2016).

[97] StarCCM+, *StarCCM+ Manual,* (2018).

[98] Fluent, *Fluent Manual,* (2017).

[99] F. Liu, *A Thorough Description Of How Wall Functions Are Implemented In OpenFOAM,* Proceedings of CFD with OpenSource Software , 1 (2016).

[100] A. Urbano, L. Selle, G. Staffelbach, B. Cuenot, T. Schmitt, S. Ducruix, and S. Candel, *Exploration of combustion instability triggering using Large Eddy Simulation of a multiple injector liquid rocket engine,* Combustion and Flame **169**, 129 (2016).

[101] M. P. Juniper, *Triggering in Thermoacoustics,* International Journal of Spray and Combustion Dynamics **4**, 217 (2012).

[102] S. Dederichs and C. Beck, *Validation of a Novel Les Approach Using Tabulated Chemistry for Thermoacoustic Instability Prediction in Gas Turbines,* , 1 (2015).

[103] A. Escue and J. Cui, *Comparison of turbulence models in simulating swirling pipe flows,* Applied Mathematical Modelling **34**, 2840 (2010).

[104] A. Wanik and U. Schnell, *Some remarks on the PISO and SIMPLE algorithms for steady turbulent flow problems,* Computers and Fluids **17**, 555 (1989).

[105] T. I. M. Lieuwen and Y. Neumeier, *Nonlinear Pressure-Heat Release Transfer Function Measurements in a Premixed Combustor,* **29**, 99 (2002).

[106] K. Kim, D. Lee, H. J. Lee, J. G. Quay, and D. Santavicca, *Flame transfer function measurement and instability frequency prediction using a thermoacoustic model,* Proceedings of the ASME Turbo Expo **2**, 799 (2009).

[107] F. M. Berger, T. Hummel, B. Schuermans, and T. Sattelmayer, *Pulsation-Amplitude-Dependent Flame Dynamics of High-Frequency Thermoacoustic Oscillations in Lean-Premixed Gas Turbine Combustors,* Journal of Engineering for Gas Turbines and Power **140**, 041507 (2017).

Faculty of Mechanical Engineering
Mekelweg 2
2628 CD Delft
The Netherlands